

Passive Acoustic Mapping For Monitoring Burst Wave Lithotripsy

AADARSH MISHRA

ST PETERS COLLEGE

DEPARTMENT OF ENGINEERING SCIENCE

A thesis submitted for the degree of **Doctor of Philosophy**

Supervised by **Professor Robin Cleveland**

ABSTRACT

Burst Wave Lithotripsy (BWL) is a non-invasive treatment modality for kidney stone fragmentation. Studies have shown that BWL induces lesser tissue damage than Shock Wave Lithotripsy and has no risk of infection, as observed in other treatment options such as ureteroscopy. This thesis studied the mechanical properties of porcine tissues and agarose using uniaxial compression testing, oscillatory shear testing and oscillatory nanoindentation testing. This work: i)Investigated the mechanical properties of the kidney at the macro-length scale and micro-length scale. A shear modulus of 0.5 kPa was obtained at 1 Hz, and 0.01% strain using oscillatory shear experiments at the macro-length scale. Oscillatory nanoindentation experiments yielded a shear modulus varying from 25 kPa to 45 kPa as the frequency varied from 10 Hz to 110 Hz at the micro-length scale. ii)Studied other porcine tissues such as the aorta, heart, liver and brain. The highest shear modulus of 4.2 kPa was obtained for porcine aorta, followed by the heart at 1.9 kPa, the liver at 0.3 kPa and the brain at 0.2 kPa. iii)Studied the mechanical properties for a range of agarose concentrations at the macro and micro-length scales, and identified agarose concentrations with viscoelastic properties similar to the porcine organs. The shear modulus of 0.4% agarose resembled the porcine heart, and 0.3% agarose resembled the porcine kidney. The porcine liver had a shear storage modulus 50% lower than the 0.25% agarose, which was the lowest possible agarose concentration for gelation or solidification. At the micro-length scale, the shear modulus of 1.2% agarose was in a similar range as that of the porcine kidney. iv)Applied fractional viscoelastic models to the porcine tissues and agarose samples, and predicted their stress response. The S-FKV model fitted the frequency response of porcine organs, whereas springpot fitted the frequency data of agarose and aorta. The stress predicted for porcine organs and the amplitudes of measurements were within 26% using the S-FKV model and 10% using the springpot model for agarose samples. v) Localised the cavitation events during BWL using Passive Acoustic Mapping (PAM) and

quantified the cavitation around the stone using parameters such as the Spatial Integral Frame Power and Treatment Average Total Spatial Power, and investigated the agarose damage. The highest agarose damage and Treatment Average Total Spatial Power were observed in the stones prepared using the rubber mould due to higher surface roughness.

Overall this work extracted the mechanical properties of porcine kidneys, which helped us understand their response during the BWL. The mechanical properties of other porcine tissues were extrapolated to higher frequencies using the S-FKV and springpot model and compared with the results from elastography techniques available in the literature. The agarose concentration developed for the porcine heart will be useful as an in-vitro model during elastography, and the agarose concentration developed for the porcine kidney will be helpful as an in-vitro model during lithotripsy. The PAM results showed that cavitation is dominated by the surface roughness and dimensions of stone, which will vary between the patients. We were unable to extract useful time-sensitive information using PAM during the BWL.

Acknowledgements

I would like to thank my supervisor Professor Robin Cleveland for the guidance and everlasting support. He has extensive knowledge in the domain of viscoelasticity and acoustics, which helped me to finish the DPhil within the required timeframe.

I would like to thank Nicolas Hawkins for the training and support offered during the oscillatory shear testing and Dr Igor Dyson for the training on the Universal Testing Machine. I am extremely thankful to Dr Riaz Akhtar and his wonderful team at the University of Liverpool for hosting me every time I visited Liverpool during the nanoindentation experiments. Dr Riaz Akhtar provided me with the relevant training and insights to the working of nanoindenter setup. I was delighted to participate in this collaboration between the University of Oxford and the University of Liverpool.

I would like to thank my former lab group member Dr Cameron Smith for the PAM analysis from the ultrasound data collected during BWL experiments. Further, I would like to thank BUBBL group members: Prof. Constantin Coussios for his feedback during the group meetings in the first year of my project and James Fisk for manufacturing the experimental setup and other components in his workshop. I am also thankful to St. Peter's College for all the help and support. A special thanks to my mother, Kanak Lata Mishra, for her support during my DPhil and father, Late Ram Sewak Mishra.

Finally, I would like to acknowledge the financial help I received from the National Institute of Health (NIH) in the form of a studentship and conference travel.

Contents

1 Introduction 1

1.1 Shock Wave Lithotripsy 3

1.2 Tissue damage during SWL 6

1.2.1 Mechanism behind tissue damage 9

1.3 Burst Wave Lithotripsy 13

1.4 Injury during BWL 17

1.5 Passive Acoustic Mapping 20

1.6 Aim & Thesis outline 26

2 Mechanical testing of Porcine Kidney

2.1 Introduction 28

2.2 Viscoelasticity 29

2.2.1 Viscoelastic models 30
2.2.2 Kelvin-Voight model 30
2.2.3 Maxwell model 31
2.2.4 Fractional derivative model 32

2.3 Methods of Mechanical testing 35

2.3.1 Uniaxial Compression 35
2.3.2 Oscillatory Shear 35
2.3.3 Oscillatory Nanoindentation 36

2.4 Uniaxial Compression 39

2.5 Rheological Tests 41

2.5.1 Strain sweep 42
2.5.2 Frequency sweep 43
2.5.3 Stress relaxation 47

2.6 Nanoindentation Test 48

2.7 Discussion and Conclusion 49

3 Mechanical testing of Porcine Tissues

3.1 Introduction 52

3.2 Materials and Methods 53

3.3 Results 54

3.3.1 Strain sweep 54
3.3.2 Frequency sweep 56
3.3.3 Stress relaxation 62

3.4 Discussion and Conclusion 64

4 Mechanical testing of Agarose as a Tissue Mimic for Porcine Organs

4.1 Introduction 67

4.2 Materials and Methods 68

4.2.1 Agarose preparation 68
4.2.2 Uniaxial Compression 68
4.2.3 Oscillatory Shear 69
4.2.4 Oscillatory Nanoindentation 70

4.3 Results

4.3.1 Uniaxial Compression 70
4.3.2 Strain sweep 72
4.3.3 Frequency sweep 75
4.3.4 Stress relaxation 80
4.3.5 Nanoindentation Test 82

4.4 Discussion 88

4.5 Conclusion 90

5 Passive Acoustic Mapping In Monitoring Burst Wave Lithotripsy

5.1 Introduction 91

5.2 Methodology 91

5.2.1 Experimental setup 94
5.2.2 Preparation of agarose samples 100
5.2.3 Preparation of Ultracal-30 stone 101

5.3 Results 102

5.3.1 Stone fragmentation 102
5.3.2 Agarose damage 107

5.4 Discussion and Conclusion 110

6 Conclusion 113

6.1 Future Work 117

References 119

CHAPTER 1: INTRODUCTION

Kidneys are excretory organs which regulate the volume and composition of the internal fluid environment [1] [2]. Figure 1.1 depicts the internal anatomy of the kidney. The renal cortex is a red-coloured soft tissue under the renal capsule and is the outer region of the kidney. The renal medulla is the inner region, and the cortex and medulla consist of blood in their working condition. The renal column is the connective tissue separating the renal pyramids which create urine and terminate into a renal papilla. Each renal papilla drains into a collecting pool called a minor calyx; several minor calyces connect to form a major calyx; all major calyces connect to a single renal pelvis which then connects to the ureter.

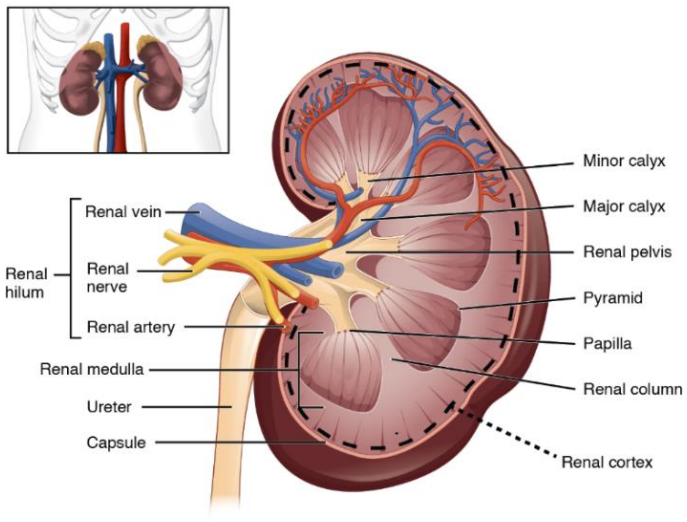


Figure 1.1. Internal anatomy of the human kidney [3]

Kidney stones are mineral deposits in the renal calyces and pelvis that are found free or attached to the renal papillae. They contain crystalline and organic components and are formed when urine becomes supersaturated with a mineral, leading to crystal formation, growth, aggregation and retention within the kidneys [4,5]. Globally, calcium oxalate and calcium phosphate account for ~80% of kidney stones, uric acid for 9%, struvite for 10% and cystine for 1% [6]. Treatment options for kidney stones include Percutaneous Nephrolithotomy (PCNL), Ureteroscopy and Shock Wave Lithotripsy (SWL).

Ureteroscopy involves the visualisation of the kidney collecting system using a rigid, semi-rigid or flexible endoscope known as a ureteroscope which has a working channel that allows the introduction of a variety of instruments for stone removal. Ureteroscopy is used for the treatment in the following cases: a) Renal calculi less than 20 mm in size, b) Mid or distal ureteral calculi, c) Stones such as cystine which are resistant to SWL, d)Removal of renal calculi fragments following SWL or PCNL [7]. Ureteroscopy has a stone-free rate of ~91% [8]. PCNL involves creating an access tract into the renal collecting system through which nephroscopy can be performed. The nephroscope has a working channel through which an intracorporeal lithotripsy device such as a laser can be introduced, and stone fragments are removed using graspers. PCNL is considered more invasive than other treatments and is only recommended for large stones (>20mm diameter). Stone-free rates reported from PCNL are up to 90% [9].

1.1. SHOCK WAVE LITHOTRIPSY

The first kidney stone treatment was reported in 1980 with an extracorporeal device using shock waves [10-12]. SWL remains one of the first-line treatments for kidney stones today, with a stone-free rate of ~87% at the 3-month follow-up [13]. Shock waves can be generated using electrohydraulic, electromagnetic and piezoelectric sources known as lithotripters. Lithotripters can be categorised into three types depending on their shock wave-generating principle:

i)Electrohydraulic

Electrohydraulic lithotripter generates shock waves using a spark source, which is focused by an ellipsoidal reflector, see Fig. 1.2. This device consists of a high voltage capacitor (10-30 kV) that is discharged and results in the growth and collapse of vapours generating a spherically spreading shock front. The position of the spark is at the first focus of the ellipse and is critical to the shock wave focus. A few millimetres of misalignment can cause a significant loss of focus [12].

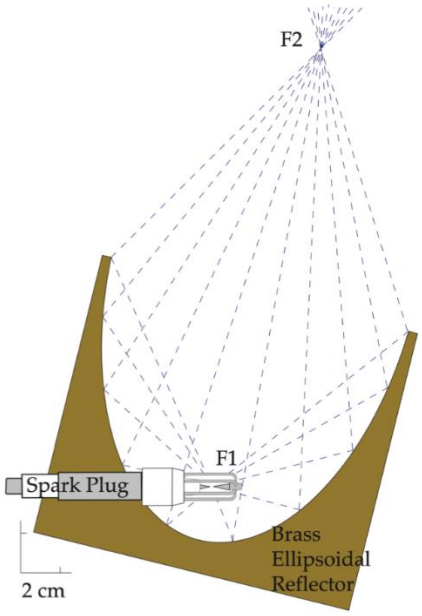


Figure 1.2. Electrohydraulic lithotripter and the spark plug at first focus [12]

ii)Electromagnetic

An electromagnetic lithotripter consists of an electrical coil and a metal plate in close proximity, see Fig. 1.3. A short electric pulse is passed through the coil, which generates a repulsive force on the metal plate. This generates an acoustic wave which is focused by an acoustic lens. Electromagnetic lithotripter generates a high-intensity ultrasonic wave, and a non-linear distortion occurs during its propagation. This produces a shock before the wave reaches the focus [12].

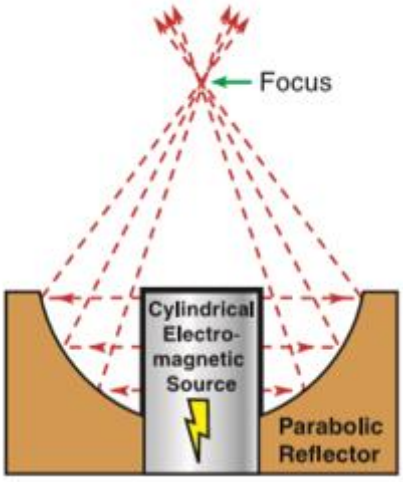


Figure 1.3. Schematic of an Electromagnetic lithotripter [12].

iii)Piezoelectric

This type of lithotripter uses piezoelectric crystals to form an ultrasonic wave. A voltage is applied to a large number of piezoelectric crystals, which leads to their deformation producing an acoustic wave. The crystals are placed inside a spherical cap, and the acoustic wave is focused at the centre of curvature [12].

A shock wave is created by the non-linear distortion of the wave. Shock wave sources are optimized to generate a pulsed waveform, typically on the order of microseconds in duration. The peak positive pressure ranges from 20 MPa to 110 MPa, and the peak negative pressure varies from 5 MPa to 15 MPa [12]. Typically, 2000 to 4500 shock waves are used to fragment

kidney stones [14]. As shown in Fig. 1.4a, a lithotripter shock wave is a 5 µs duration acoustic pressure pulse consisting of a compressive phase followed by a tensile phase. It begins with a near-instantaneous jump to peak positive pressure of 40 MPa. This transition is known as 'Shock' and is less than 5 ns long. About 1 µs later, the pressure falls to zero, and there is a region of negative pressure or tensile phase with a peak negative pressure of 10 MPa lasting around 3 µs. There is no abrupt pressure transition in the negative or tensile component of the shock wave, and the amplitude of peak positive pressure is higher than that of peak negative pressure [12]. Figure 1.4b shows the Fourier transform spectra of the waveform with a peak around 150 kHz.

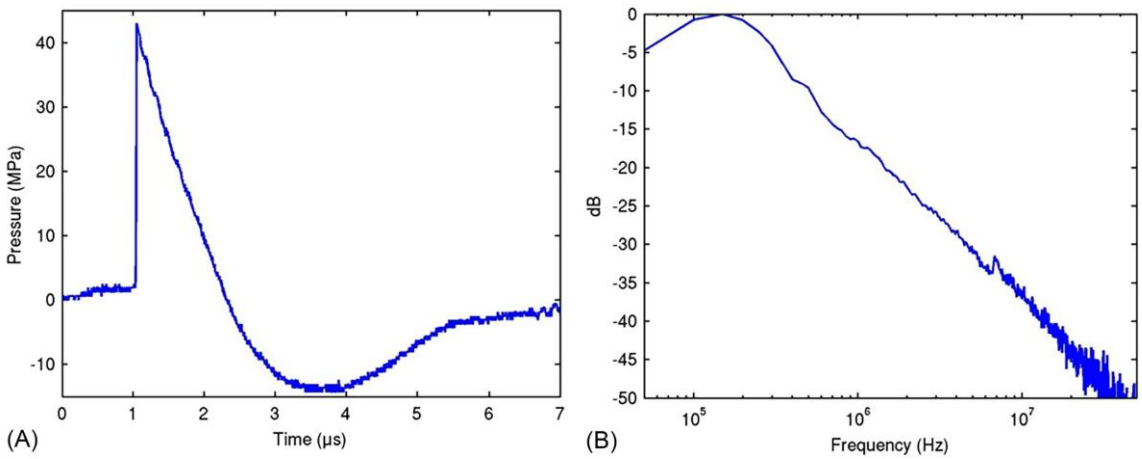


Figure 1.4. (a) A pressure waveform measured at the focus of an electrohydraulic lithotripter, (b) The Fourier transform of the waveform shows a broad spectrum with a peak around 150 kHz [15].

To a first approximation, the area under a pressure-time trace for an acoustic wave needs to integrate to zero, and hence the pulse has both positive and negative pressure phases. Linear acoustics describes the propagation of low-amplitude waves such that every point on the wave travels at the same speed. The small-signal sound speed c_0 is ~1500 m/s in water and tissue. Equation 1.1 describes the relation between local phase speed c and pressure amplitude p.

$$c = c_0 + \beta \frac{p}{\rho_0 c_0} \qquad (1.1)$$

where ρ_0 is the density of the medium and β is the coefficient of nonlinearity of the medium. The non-linear distortion of the pulse steepens the rise time of the leading positive phase. However, absorption also plays an important role, and a shock front is formed due to the balancing of the nonlinear distortion and absorption.

1.2. TISSUE DAMAGE DURING SWL

Rubin et. al. [16] performed Computed Tomography (CT) before and after the shock wave treatment in fifty patients to determine the extent of renal injury or haematuria. These patients were subjected to 800 to 2400 shock waves, and the discharge voltage ranged from 18 kV to 24 kV. Subcapsular hematomas were observed in eight patients, and intrarenal hematomas in two patients. Perinephric soft tissue stranding was seen in thirty-seven of fifty-three treated kidneys. Ng et. al. [17] evaluated renal injury after extracorporeal shock wave therapy was performed on 320 patients. In this study, the patients were randomised to receive one of the four treatment protocols or groups: Group 1) Patients received 20 shock waves at 19.2 kV from the beginning to the end of treatment. This group was known as a control group. Group 2) Patients received the first 100 shocks at 9.6 kV, followed by shock waves at 19.2 kV until the end of treatment. Group 3) Patients received 100 shocks at 9.6 kV, followed by a 3-minute pause and then further shock waves at 19.2 kV. Group 4) Patients received 100 shocks at 19.2 kV, followed by a 3-minute pause and then further shock waves at 19.2 kV until the end of treatment. All the shock waves were delivered at a rate of 2 Hz. A 3T Magnetic Resonance Imaging (MRI) was used to perform imaging in the axial and coronal phases of the kidneys in 197 patients, and CT scanning was performed in 115 patients. The number of patients developing haematoma was eight (10.26%), seven (8.97%), six (7.59%) and three (3.90%) in groups 1 to 4, respectively. Overall, the subcapsular or perinephric haematoma was detected in twenty-four patients and complications such as vomiting, loin pain, chest discomfort and dizziness developed immediately after SWL in twelve patients. The symptomatic perinephric haematoma was

detected in one patient, which led to acute renal failure. Krishnamurthy et. al. [18] performed a long-term radiographic study on nineteen patients with twenty-one SWL-induced haematomas. All patients were treated with a Dornier HM3 lithotripter. The number of shock waves delivered was 500 to 2400 at 18 kV to 19 kV. These patients were followed from 4 to 61 months after SWL. In eighteen haematomas, a complete radiographic resolution was observed on ultrasound 3 to 46 months after the SWL treatment.

The porcine kidney is commonly used as an animal model and as a control group due to its easy availability, and similar anatomy and function to the human kidney [19,20]. Hence, various studies have investigated the effect of SWL-related injury on porcine kidneys. Shao et. al. [21] conducted a study and treated one kidney in each of six juvenile pigs (6-7 weeks old) with 1000 shock waves delivered at 24 kV and 2 Hz. These shock waves were directed at the lower pole calyx of the right kidney using an HM3 lithotripter. In this study, three pigs were used as sham controls, while the other three were used to quantitate lesion size and observe the damage. There was no tissue damage in sham control kidneys, while SWL-treated kidneys showed signs of injury with a lesion of 0.2%±0.1% of the renal volume. At the lithotripter focus, intraparenchymal haemorrhage and tubular injury occurred in both the cortex and medulla. During the autopsy, this study observed that all SWL-treated kidneys had a subcapsular haematoma, which appeared on either the anterior or posterior surface of the kidney. Multiple areas of intraparenchymal haemorrhage were observed in both the cortex and medulla during the gross examination of cross-sections at lithotripter focus, see Fig. 1.5. Haemorrhage sites ranged from small circumscribed regions around an injured vessel to enlarging areas extending up to the renal capsule which occasionally connected to a subscapular haematoma.

a) b)



Figure 1.5. a) SWL-treated kidney. Double arrow shows one large hemorrhagic site extending from the medulla to the renal capsule, resulting in a subcapsular hematoma. Single arrow shows a smaller hemorrhagic site near the renal capsule. b)Sham kidney [21]

Connors et. al. [22] performed a study to determine the impact of shock waves on lesion size and renal function. Each pig received 2000 shock waves at a frequency of 2 Hz and a discharge voltage of 12 kV,18 kV or 24 kV to the lower pole calyx of the kidney. A lesion was observed on the anterior or posterior surface of the kidney from the 12 kV group, characterised by a small region of haemorrhage (less than 0.5 mm in diameter) or multiple sites of petechial bleeding. As the discharge voltage was increased from 18 kV to 24 kV, the lesion became extensive and traversed the kidney, see Fig. 1.6. In the kidneys treated with 24 kV, a subcapsular haematoma encased the entire lower pole. All treated groups (12 kV, 18 kV and 24 kV) showed intraparenchymal haemorrhage.

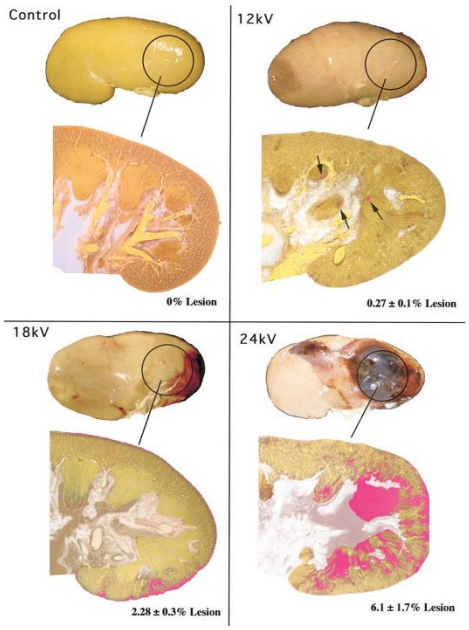


Figure 1.6. Impact of discharge voltage (12 kV, 18 kV and 24 kV) on the lesion volume or tissue injury [22].

1.2.1. Mechanism behind tissue damage

Shock waves produce an acoustic field resulting in two mechanical forces on stones and tissue, i) Direct stress associated with high amplitude shock, and ii) Stresses and microjets due to violent growth and collapse of bubbles known as cavitation [12]. Studies [21] [23] have suggested that either inertial cavitation or shear stresses are the potential mechanisms behind tissue injury during the SWL treatment.

Cavitation mechanism

Acoustic cavitation refers to the generation of bubbles in the fluid when it is ripped apart by the negative pressure or tensile phase of the wave. The presence of small gas pockets initiates cavitation, and the tensile phase of the wave causes bubble growth from micro-metre to milli-metre length scale over a duration of hundreds of microseconds. This is followed by a violent collapse of the bubble [12].

Coleman et. al. [24] detected cavitation during SWL by observing the impact of a liquid jet associated with the bubble collapse. In this study, X-ray films, thin aluminium sheets, and thick

metal plates were used as targets, and it was observed that thin foils punctured while metal plates were deformed due to the violent jet impact. This study concluded that violent cavitation during SWL is a potential cause behind tissue trauma. Cleveland et. al. [25] performed measurements of shock waves using a membrane hydrophone. The hydrophones were oriented perpendicular to the shock waves using fluoroscopic imaging and placed on the anterior or posterior surface of the left kidney of pigs. Shock waves were generated using a Dornier HM3 lithotripter, and the voltage was varied from 12 kV to 24 kV. Secondary shock waves were measured in-vivo and 3 ms after the initial shock waves, potentially due to the collapse of the bubble or cavitation. Coleman et. al. [26] observed acoustic emission due to the inertial cavitation in tissue during SWL in four patients. In this study, the hydrophone was acoustically coupled to the patient's skin, and the focus was directed at depth in the tissue under ultrasound guidance. The signal measured by the focused hydrophone was interpreted as originating from shock waves due to bubble collapse. Williams et. al.[27] suggested acoustic cavitation as the cause of cell damage due to shock waves under in-vitro conditions. In this study, a Dornier HM3 lithotripter was used to produce shock waves such that the peak positive pressure varied from 29 MPa to 37 MPa as the discharge voltage varied from 15 kV to 24 kV. The pressure chamber for cell storage consisted of a bronze aluminium cylinder, and polyphenylene oxide was used to mill the end caps since it allowed shock wave propagation with minimal attenuation and no waveform change. Red blood cells were exposed to shock waves at atmospheric and hydrostatic pressure higher than 8 MPa. It was found that cell lysis significantly reduced under high hydrostatic pressure (1.03±0.09%) compared to atmospheric pressure (7.3±1.7%) at 24 kV.

Evan et. al. [28] generated 2000 shock waves at 24 kV using a Dornier HM3 lithotripter. This study treated the kidneys of six week old pigs using a rigid and pressure release reflector. A pressure-release reflector transposes the compressive and tensile part of a shock wave. A

pressure release reflector is formed by fitting the brass ellipsoidal reflector of the lithotripter with a polyurethane foam which is an air-filled matrix and has a pressure reflection coefficient of approximately -1. Due to the pressure-release reflector, the acoustic waveform from the lithotripter consists of a leading negative pressure trough followed by a trailing positive spike. The trailing positive spike reduces the bubble expansion cycle by forcefully collapsing the bubble. Since the intensity of cavitation depends on both the magnitude and duration of the tensile component, the bubble collapse becomes less violent, and the cavitation is stifled. In the kidneys treated using a rigid reflector, subcapsular haematomas encased the anterior and posterior surfaces of the lower renal pole. Also, multiple sites of intraparenchymal haemorrhage were observed, which encompassed the cortex and tips of renal papillae. Since the pressure-release reflector suppressed the cavitation, there was a reduction in kidney damage. In kidneys treated with pressure-release reflector, small sites of intraparenchymal injury and haemorrhage were observed at the tips of medullary papillae, see Fig. 1.7 and 1.8.

a) b)



Figure 1.7. Morphological appearance of kidneys treated using a) rigid reflector and b) pressure release reflector. Arrows show the subcapsular hematoma that encased the anterior and posterior surfaces of the lower pole. No injury was detected on the lower pole of pressure-release reflector treated kidneys [28].

a) b)



Figure 1.8. Digitized mid-coronal plane images of kidney treated with a) rigid reflector (b) pressure release reflector. Arrows show the regions of intraparenchymal hemorrhage in cortex and medulla in kidneys treated with rigid reflector. Arrowhead shows the vascular injury in kidneys treated with pressure release reflector with small sites of intraparenchymal hemorrhage [28].

Lifshitz et. al. [29] generated shock waves using a Dornier HM3 lithotripter and quantified the acoustic cavitation damage using aluminium foil targets which were placed inside the polypropylene cryovials. Castor oil and ringer solution was filled inside the cryovials to vary the amount of cavitation, and foil damage was quantified using a damage index. Vials were treated with 150 shock waves at 18 kV. Damage of 2.2% ± 0.3% was observed in foils treated with shock waves submerged in ringer buffer. This damage was reduced to 0.3% ± 0.1% as the buffer was degassed. No damage was observed in foils submerged in castor oil since it is a non-cavitating fluid. This study concluded that acoustic cavitation played a role in foil deformation.

Non-Cavitation mechanism

A shock wave first compresses the tissue for about 1 μs and then induces tension for a few microseconds. The total strain caused by lithotripter shock waves during compression and tension is estimated to be less than 2% [30]. The strength of a shock wave varies laterally along

the wavefront leading to tissue shearing. Freund et. al. [31] estimated a maximum shear strain of 0.26% during the SWL treatment. During the calculations, the maximum shear was associated with the compressive or positive pressure of the wave and the tensile or negative pressure was neglected. Howard and Sturtevant [30] studied the effects of focused shock waves on thin-planar polymeric membranes immersed in various tissue-mimicking fluids. In this study, no damage was observed in membranes immersed in a non-cavitating liquid, while membrane failure was observed when heterogeneous scatterers were seeded in the liquid. This was due to the variable acoustic properties of the medium during seeding, which caused focusing and defocusing of the shock front leading to a lateral variation and a relative shearing motion of the membrane. Hence, this study suggested shearing as a possible damage mechanism when a shock wave propagates in a heterogeneous medium like tissue. Williams et. al. [27] observed lysis of red blood cells exposed to shock waves under high hydrostatic pressure (>12 MPa). This study observed that lysis in cells subjected to shock waves was 97% higher than in control cells which were not subjected to shock waves. This suggested that non-cavitational mechanisms such as shear, spallation, or fluid streaming within the cell vials could induce cell damage even at high pressures.

1.3. BURST WAVE LITHOTRIPSY

A new technique known as Burst Wave Lithotripsy (BWL) has emerged as an effective and less injurious extracorporeal modality to fragment kidney stones with the potential of being offered as office-based treatment [32]. Over the past few years, BWL has progressed from conception to human clinical trials and fragmented various stone compositions in both human and animal studies . BWL uses bursts of sub-megahertz (currently 350 kHz) focused ultrasound at relatively low-pressure amplitudes (typically less than 10 MPa) for stone comminution, see Fig. 1.9. The BWL treatment generates small fragments which can be passed without any

additional intervention. The BWL transducer is small enough to be hand-held and uses B-mode ultrasound for stone detection and localisation which makes it well suited for an office-based modality. This contrasts to SWL which is typically a large installation in a hospital environment often with C-arm fluoroscopy used for stone localisation.

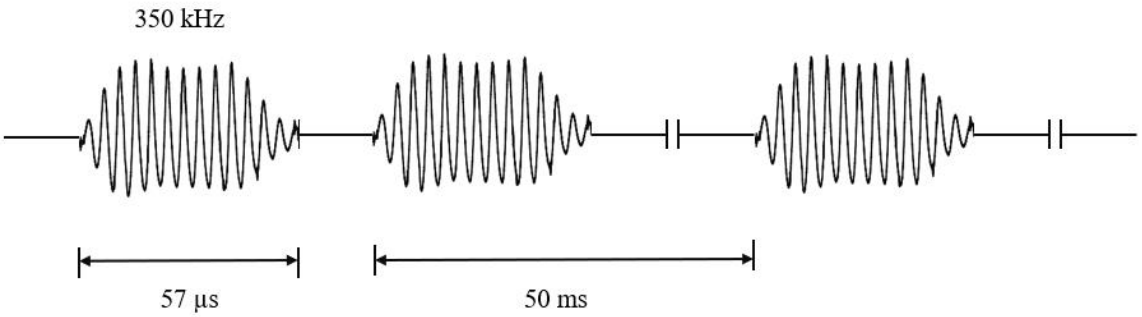


Figure 1.9. Representative waveform employed in BWL. A 10-cycle burst at 350 kHz (57 µs) is transmitted every 50 ms (20 Hz pulse repetition frequency).

The physical aspects of the stone destruction during BWL are due to a combination of the following mechanical factors:

i)Burst waves induce tensile and shear stresses inside the stone, leading to the generation and propagation of fractures which results in fragmentation [33]. Theoretical modelling of stones treated with BWL has shown that amplifications of stresses occur inside the stone due to their geometry and contributes to the increased fragmentation [34].

ii)Cavitation is generated by the tensile phases of the BWL pulses and is preferentially induced at the stone's surface, and the collapsing bubbles reduce the stone to fine dust through surface erosion. However, abundant cavitation clouds can shield the stone from the propagation of further acoustic energy [33]. Hence, a careful selection of pressure amplitude and pulse repetition frequency is needed during the BWL.

Studies have been carried out varying the ultrasound frequency, pulse repetition frequency and pressure amplitude of the BWL waveforms. Increasing the fundamental frequency of the BWL transducer results in more tightly spacing between peak tensile stresses leading to finer dust

during fragmentation and smaller stone fragments (i.e. higher stone destruction). Increasing the pressure amplitude of burst waves leads to higher stresses, although it generates higher cavitation, which shields the stone from further fragmentation. Similarly, a lower pulse repetition frequency leads to less energy being imparted to the stone for a fixed treatment period, and a higher pulse repetition frequency has the potential to create a cavitation cloud shielding the stone. Hence, a trade-off is needed in selecting an optimal pressure amplitude and pulse repetition frequency to increase the stone destruction.

Maxwell et. al. [33] treated natural and artificial stones in a water tank by generating burst waves for 10 cycles at a repetition rate of 200 Hz. In this study, the pressure threshold was determined by treating the artificial stones for 5 minutes at pressure amplitudes varying from 1.2 MPa to 6.5 MPa at 170 kHz. The fragmentation time and sizes of stones fragments were compared by subjecting natural stones of four compositions (Uric Acid, Struvite, Calcium Oxalate Monohydrate [COM] and cystine) and twelve artificial stones prepared from Begostone plastic powder to burst waves at 170 kHz and 6.5 MPa. Also, three different transducers at 170 kHz, 285 kHz and 800 kHz were used to fragment artificial stones and the effect of ultrasound frequency on fragment size was evaluated. This study concluded that the artificial stones could be fragmented at focal pressure of 2.8 MPa. The fragmentation time was 0.17 to 1.40 minutes for uric acid stones, 0.07 to 2.02 minutes for struvite stones, 8.0 to 18.1 minutes for COM stones and 10.3 to 21.3 minutes for cystine stones. Complete fragmentation was achieved in twelve artificial stones in a mean time of 9.7±2.8 minutes. Stone fragments were less than 4 mm at a frequency of 170 kHz, less than 2 mm at 285 kHz and less than 1 mm at 800 kHz. This study concluded that the fundamental frequency of burst waves controlled the stone fragment sizes, and densely spaced fractures were generated at higher frequencies leading to smaller fragments. Maxwell et. al. [32] performed an in-vivo BWL study and implanted 6 mm to 7 mm COM stones (n=6) in the kidneys of three pigs. Treatment was administered in five kidneys. Burst

waves with a focal pressure of 6.5 MPa to 7 MPa were used to fragment the stones for a duration of 30 minutes. BWL transducer with a frequency of 350 kHz delivered 20 cycle pulses at a pulse repetition rate of 10 Hz. On average, 87% of the stone mass was fragmented to sizes less than 2 mm. Stones were completely fragmented to less than 2 mm in three out of five treatments. In the other two treatments, partial disintegration of stones was observed.

Zwascha et. al. [35] performed an in-vitro study by combining BWL and Ultrasonic propulsion to improve stone fragmentation. In this study, artificial stones prepared from Begostone plaster and human COM stones were placed in a polyvinyl chloride phantom. These stones were subjected to burst waves with a transducer frequency of 335 kHz, pulse repetition rate of 40 Hz, peak focal pressure of 8 MPa and pulse duration of 20 cycles. Ultrasonic propulsion was performed using a P4-2 probe at 2.5 MHz centre frequency, 45 ms pulse duration and ~0.15 MPa peak pressure amplitude. This study observed that Begostone models were fragmented in 45 to 60 minutes when BWL alone was used, compared to combined BWL and propulsion pulses, where the stones were fragmented in 30 to 40 minutes. Successful fragmentation was considered when the fragments were less than 2 mm. This study argued that the reduction in fragmentation time when the BWL was combined with ultrasonic propulsion could be due to the following reasons: i)Fragments loosely attached to the stone were ejected due to ultrasonic propulsion, ii)Stones were reoriented due to ultrasonic propulsion leading to BWL exposure of multiple sides, iii)Ultrasonic propulsion removed the dust and cavitation bubbles around the stones which shielded it from the burst waves, and iv)Further stresses developed inside the stones due to ultrasonic propulsion.

Harper et. al. [36] performed a BWL study on nineteen human participants and twenty-three stones. In this study, burst waves were generated using a handheld transducer, and up to three stones per subject were fragmented for a maximum duration of 10 minutes. Burst waves were delivered at a frequency of 390 kHz, a pulse repetition rate of 10 Hz, maximum peak negative

pressure of 7 MPa and 20 to 50 cycles. Twenty-one out of twenty-three stones were fragmented with median stone comminution of 90% of the stone volume. Complete fragmentation was observed in nine out of twenty-three stones.

The accuracy of the BWL system is determined by a combination of the imaging and therapy resolution. Localisation of stone is performed using B-mode ultrasound with the ultrasound probe in-line with the BWL transducer. The imaging frequencies are typically in the range of 2 MHz to 5 MHz, given an axial resolution on the order of a millimetre (controlled by the pulse length) and the lateral resolution also about a millimetre (controlled by diffraction). This focal region of the BWL source is nominally 60 mm long by 6 mm wide; and therefore the resolution is predominantly controlled by the B-mode ultrasound used for localisation.

1.4. INJURY DURING BWL

Studies [32,36,37] suggest that BWL induces lesser tissue damage than SWL during stone treatment in animal models. Maxwell et. al. [32] reported BWL injury which was limited to the surface layers of the collecting system and occurred near the immediate vicinity of the implanted stone. In this study, petechial damage occurred to the urothelium in the collecting system surrounding the area containing most of the stone fragments. However, the injury did not extend to the capsular surface and histological or MRI examination did not reveal any morphological anomalies to kidney parenchyma in the treatment path, see Fig. 1.10.

a) b) c)

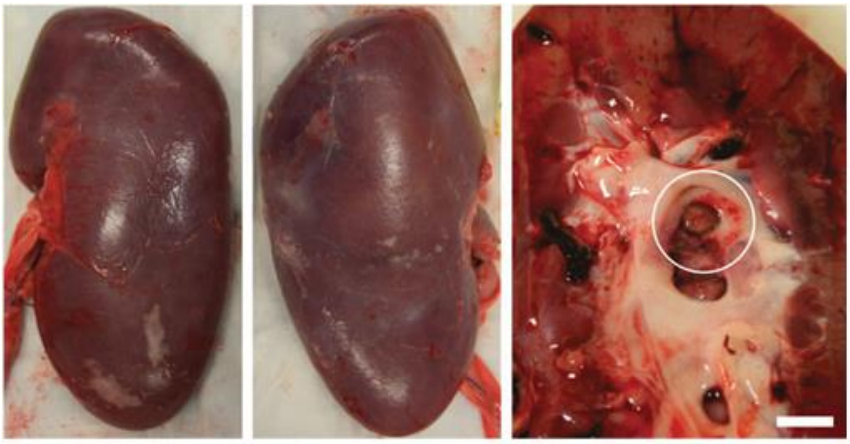


Figure 1.10. No injury to the a) anterior capsular surface, b) the posterior capsular surface and c) petechial injury to the urothelium in the vicinity of stone fragments. [32].

Wang et. al. [37] studied an animal model to assess the potential renal injury during BWL. After the BWL treatment, kidneys were removed for gross, MRI and histological analysis. During the inspection, no damage was observed to the skin overlying the treatment site or intervening tissues, and no bleeding occurred on the capsular surfaces. However, gross examination revealed a minor petechial haemorrhagic injury to the urothelium and damage to the mucosa of the collecting space, see Fig. 1.11.

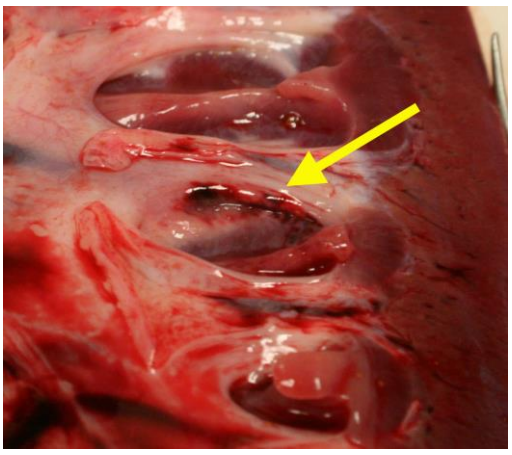


Figure 1.11. Yellow arrow shows the Petechial injury to the urothelium in the vicinity of the stone fragments [37]

Harper et. al. [36] assessed the injury in nineteen human patients after BWL treatment by classifying the tissue injury as grade 0 (within normal limits) or grade 1 (mild). Mild haematuria was observed in all the cases and no injury beyond mild was observed in any patient. Mild redness of skin was experienced by five subjects, and it resolved within 24 hours after treatment. No injury was observed in five subjects, and the injuries observed in other subjects were: small blood clots, tiny red spots and sites of bleeding at the papillae tip, mild to negligible urothelium bruising and petechial haemorrhage along some papillae, see Fig. 1.12.



Figure 1.12. Mild clotting and papilla bruising classified as grade 1 injury. Also, there are stone fragments less than 2 mm [36].

May et. al. [38] performed BWL treatment on ten kidneys from five pigs using a 170 kHz or 335 kHz transducer. The upper, middle and lower poles of each kidney were treated at a pressure amplitude from 5.8 MPa to 8.1 MPa with a pulse length of 10 cycles, a pulse repetition rate of 200 Hz at a transducer frequency of 170 kHz or a pulse length of 20 cycles, a pulse repetition rate of 40 Hz at a transducer frequency of 335 kHz. Kidneys were perfusion fixed and scanned using a 3T MRI followed by histomorphometric analysis. A haemorrhagic injury was detected in 47.6% of the BWL-treated sites, and no identifiable injury was detected in the remaining sites. MRI injury volume varied from less than 0.01% to 2.40%, and the morphometric injury volume varied from less than 0.1% to 5.2%.

1.5. PASSIVE ACOUSTIC MAPPING

An ultrasound-based technique known as Passive Acoustic Mapping (PAM) can be used for real-time three-dimensional mapping of acoustic emissions induced by an ultrasound field. During PAM, a set of receivers are used to passively record acoustic emissions from collapsing bubbles. A beamforming technique is used to filter and combine the received signals, and spatial power is estimated in the region of interest. Cavitation energy maps can be generated which provides information on the spatial distribution of sources in the region of interest [39]. A detailed discussion on beamforming techniques and the steps involved are outlined in the Chapter 5 of this thesis. Gyongy et. al. [40] used 3% agar as a tissue-mimicking cavitating medium and conducted the experiments in a water tank at 20 ℃. A transducer of 1.06 MHz frequency operating at 1.15 MPa was used to generate HIFU waves in the tissue mimicking phantoms. In this study, the peak rarefactional pressure was also increased to 1.67 MPa and 2.50 MPa to obtain a large and contiguous cavitation region. Acoustic emissions were extracted using an L10-5 probe (5 MHz to 10 MHz) and the study observed that a single bubble could be localised using PAM maps, see Fig. 1.13. Also, cavitation maps obtained from PAM at 1.67 MPa and 2.50 MPa confirmed a widening cavitation region with increasing pressure amplitude, see Fig. 1.14 and 1.15.

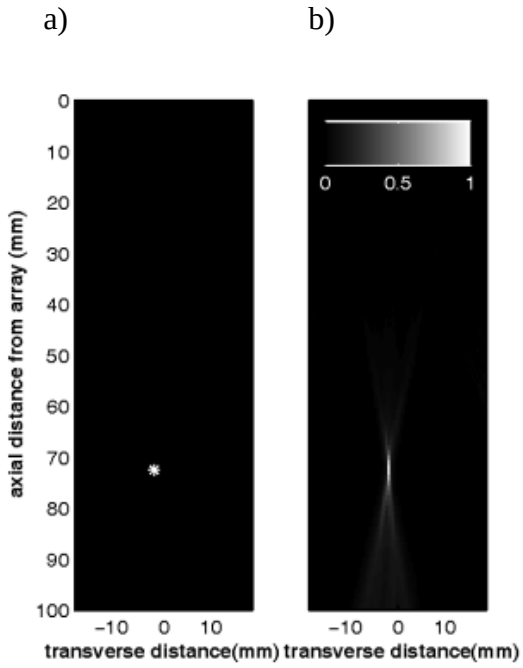


Figure 1.13. a) Position of HIFU focus, b)Passive mapping of a single cavitating bubble [40]

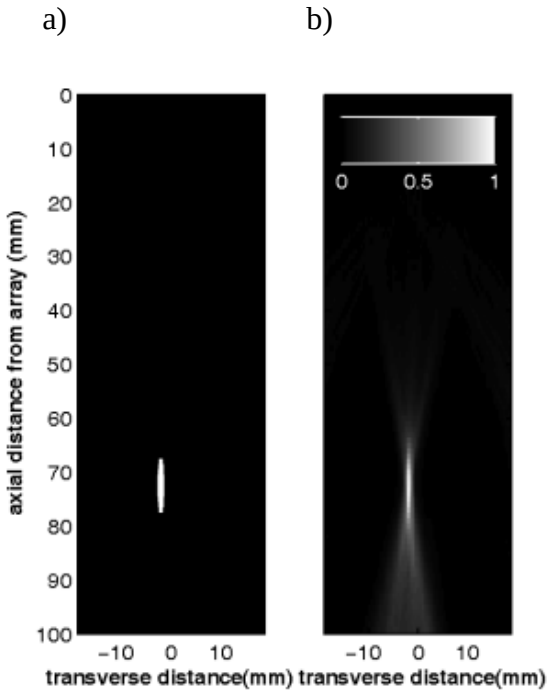


Figure. 1.14. a) Estimated cavitation region around HIFU focus b)Passive mapping of a cavitation region produced in agar gel exposed to 1.06 MHz HIFU transducer at 1.67 MPa peak rarefaction focal pressure [40].

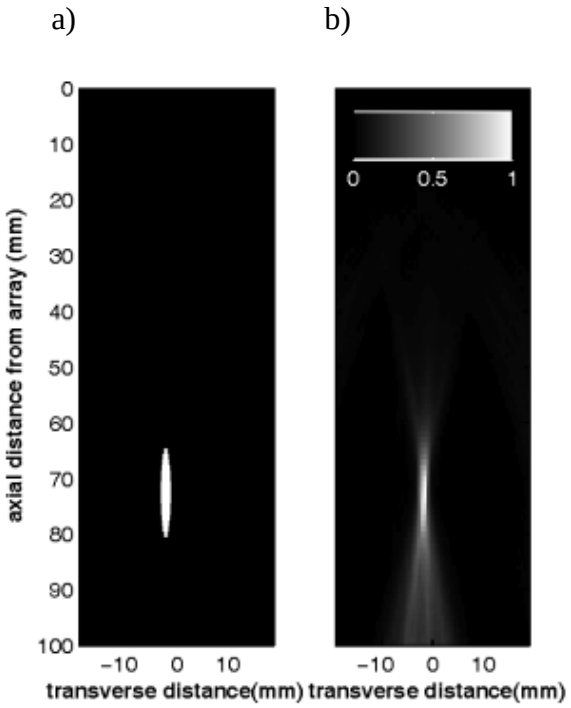


Figure 1.15. a) Estimated cavitation region around HIFU focus b)Passive mapping of a cavitation region produced in agar gel exposed to 1.06 MHz HIFU transducer at 2.50 MPa peak rarefaction focal pressure [40].

Jensen et. al. [41] performed High-Intensity Focused Ultrasound (HIFU) on five freshly excised bovine livers. Lesions were generated in ex-vivo samples of bovine liver, and a 5 to 10 MHz linear array transducer (L10-5) recorded acoustic emissions. Tissues were subjected to 180 HIFU exposures at peak rarefactional pressure varying from 3.6 MPa to 8 MPa for a duration of 2 to 10 seconds. Passive Acoustic Mapping correctly predicted the location of ablation in 42 out of 45 exposures, see Fig. 1.16.

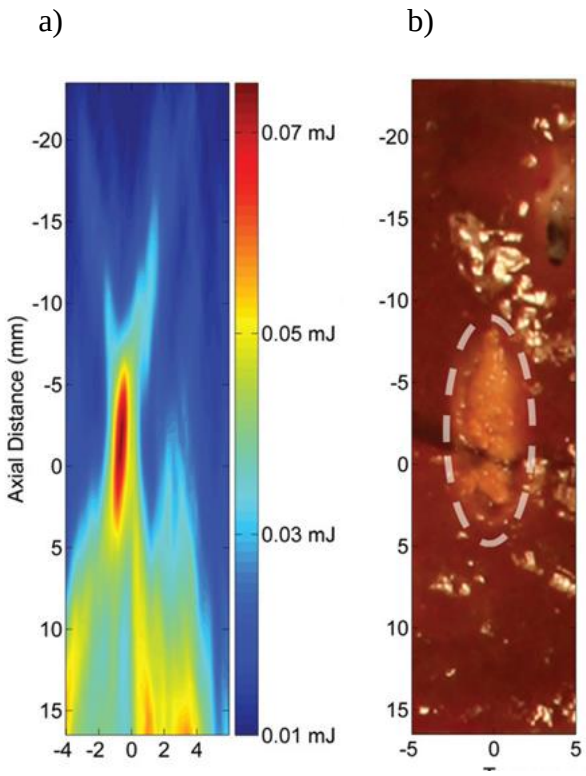
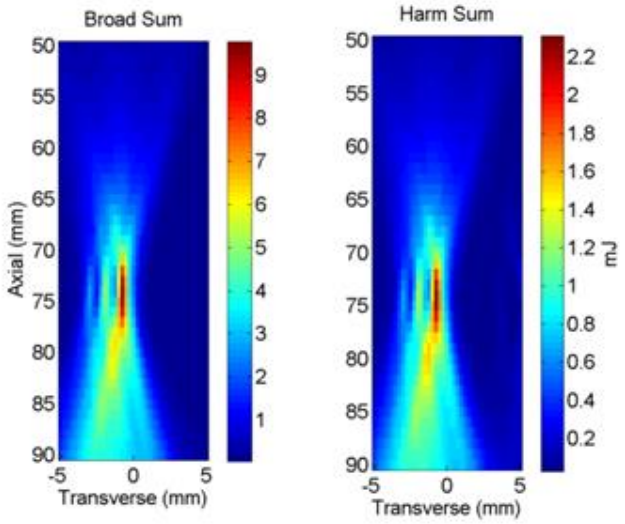


Figure 1.16. a) Source energy computed using PAM from a 5 second treatment at 6.3 MPa, b) Lesioning in the liver [41].

Crake et. al. [42] performed PAM analysis of microbubbles in an in vitro flow. In this study, microbubbles were excited using a 0.5 MHz ultrasound consisting of an in-line linear array probe L10-5 with a centre frequency of 7.14 MHz. A 7% polyacrylamide tissue phantom was used as an in-vitro model and placed in a water tank maintained at 25℃. Stable and readily available commercial polymer microspheres were used as microbubbles. The HIFU transducer and imaging array were aligned with the flow channel of the polyacrylamide phantom. Microbubbles were added to the water and passed through the phantom channel. HIFU pulses of 25 cycle length, 1 Hz to 150 Hz pulse rate and 0.1 MPa to 3.7 MPa peak negative focal pressure were applied for 1 to 10 seconds. PAM results showed that increasing the flow rate or pressure increased the focal intensity, see Fig. 1.17.

a)



b)

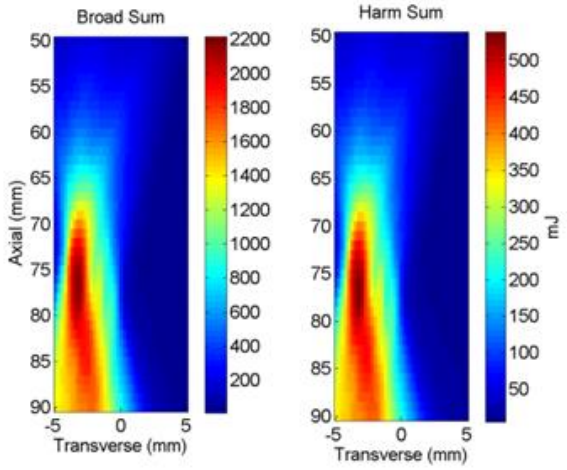


Figure. 1.17. Source energy observed at (a) 1.3MPa, 10mm/sec. (b) 3.7MPa, 174mm/sec [42].

Coviello et al. [43] performed an in-vitro PAM analysis using a 3% agar phantom with a 1.6 mm channel centred with the focal volume of two 500 kHz ultrasound transducers. An L10-5 probe (5-10 MHz) collected the acoustic emissions. A Phosphate Buffered Saline (PBS) solution consisting of a contrast agent Sonovue with a concentration of $0.3x10^6$ to $1.7x10^6$ microbubbles/mL streamed through the central channel. A 25-cycle sine wave with a peak negative pressure of 0.3 MPa was applied to generate cavitation in the microbubbles. Sonovue

microbubbles acted as cavitation nuclei and the focus of HIFU transducers overlapped the channel in one area, and the cavitation was expected to be exhibited in this area in the PAM image. A Robust Capon Beamforming (RCB) approach in PAM showed the bubble activity as expected, see Fig. 1.18.

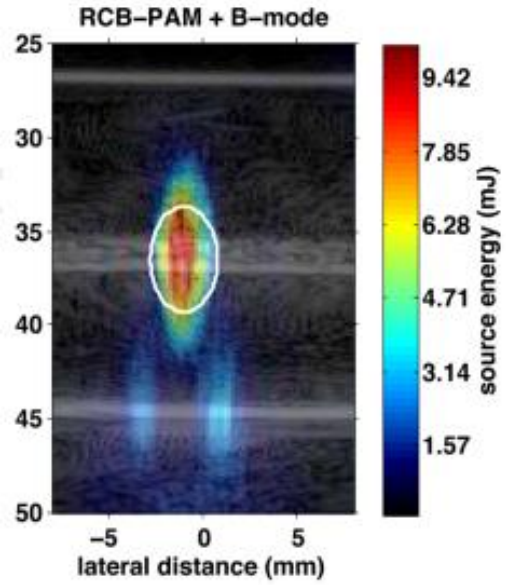


Figure. 1.18. Source energy computed using RCB and overlaid on B-mode images of a tissue phantom with a center flow channel containing microbubbles [43].

BWL combined with PAM has the potential to minimise the damage caused to kidney tissue during the treatment. PAM involves using an ultrasound array which passively listens to the acoustic emissions and computes the cavitation energy using the beamforming technique, see Sec 5.1. The cavitation map generated from PAM can be overlaid on the B-mode image and potentially used to differentiate between the cavitation on the tissue and cavitation around the stone.

1.6. AIM & THESIS OUTLINE

This study investigates the mechanical response of kidneys at pulse repetition frequencies relevant to the BWL treatment and apply a novel mapping technique known as PAM to minimise the damage caused to kidneys during BWL. With the passage of every burst wave, there is some stress stored in the kidneys while a part of this stress is dissipated. Mechanical characterisation enables quantification of the stresses stored in the form of storage modulus, and stress dissipated in the form of the loss modulus. Kidneys also undergo relaxation between the passage of burst waves, which can be quantified using a relaxation modulus. Overall, this work has measured the storage modulus, loss modulus and relaxation modulus of kidneys using rheological tests and applied an S-FKV model in the frequency domain to extract parameters and predict stress response in the time domain.

B-mode imaging is used during the BWL to perform treatment guidance, and the ultrasound transducer used for B-mode can be employed to do PAM in order to monitor and map cavitation activity during BWL. Confirmation of treatment success is difficult to be performed using B-mode imaging as the stone fragments are less than 1 mm.

This thesis aims to i) Study the mechanical properties of kidneys and determine the relevant concentration of agarose mimicking its properties, ii) Study the mechanical properties of porcine organs, apply fractional viscoelastic models and identify agarose concentrations with mechanical properties similar to porcine organs, iii) Apply PAM to monitor cavitation during BWL. In Chapter 2, the viscoelastic properties of porcine kidneys are obtained from mechanical testing, and a fractional viscoelastic model is applied to understand the kidney tissue response. Mechanical properties of the porcine heart, liver, brain and aorta are studied in Chapter 3, and fractional viscoelastic models later predict the stress behaviour of porcine organs. The mechanical properties of porcine organs are compared with 0.25%, 0.3% and 0.4% agarose concentrations in Chapter 4. Chapter 5 uses PAM to quantify cavitation when Ultracal-30 stones

are placed in agarose moulds that mimics the kidney collecting system and subjected to BWL treatment. This chapter investigates the cavitation evolution with stone fragmentation, cavitation changes with the variation in stone dimensions and stone surface roughness, and a comparison of the cavitation power with agarose damage.

CHAPTER 2: MECHANICAL TESTING OF PORCINE KIDNEY

2.1. INTRODUCTION

In this chapter, mechanical testing on porcine kidneys is performed using uniaxial tests, rheology and nanoindentation tests. Viscoelastic behaviour is characterised using a stress-controlled rheometer and a fractional viscoelastic model is fitted to the frequency domain which predicts the stress response in the time domain. Dynamic mechanical properties at the macro-scale were extracted using a rheometer until the inertial effects affected the measurement. Since cavitation occurs at a micro-length scale, viscoelastic properties of porcine kidneys were also measured at the micro-length scale as a function of frequency using oscillatory nanoindentation tests. Nanoindentation can probe small tissue volumes and spatially resolve mechanical properties such as the storage modulus and loss modulus.

There are multiple time scales that are relevant to both BWL and SWL. The fundamental frequency of burst waves varies from 170 kHz to 390 kHz [32,36,38], and the pulse repetition frequency in BWL varies from 10 Hz to 40 Hz [32,36,38]. For SWL, the shock waves has most of its energy between 100 kHz and 10 MHz, and typical PRFs of 1 Hz to 2 Hz [44]. The frequencies and time scales at which the viscoelastic properties are measured in this thesis are relevant to the pulse repetition frequency in both SWL and BWL, and these properties can provide an insight to the stress-strain response and relaxation behaviour of the tissue during these times and frequency scales. However, the instruments employed here were not able to measure properties at the microseconds timescale.

2.2. VISCOELASTICITY

Porcine organs are biological materials which exhibit time and history-dependent stress-strain behaviour [20]. This phenomenon is known as viscoelasticity, and viscoelastic materials can be thought to possess both viscous (fluid-like) and elastic (solid-like) properties. The response of a viscoelastic material is dependent on the strain and the strain rate:

$$\sigma = \sigma(\varepsilon, \dot{\varepsilon}) \qquad (2.1)$$

where σ is the stress, ε is the strain and $\dot{\varepsilon}$ is the strain rate.

Figure 2.1 represents the two classical elements: spring and dashpot, and traditional viscoelastic models use a combination of these elements.

a) b)

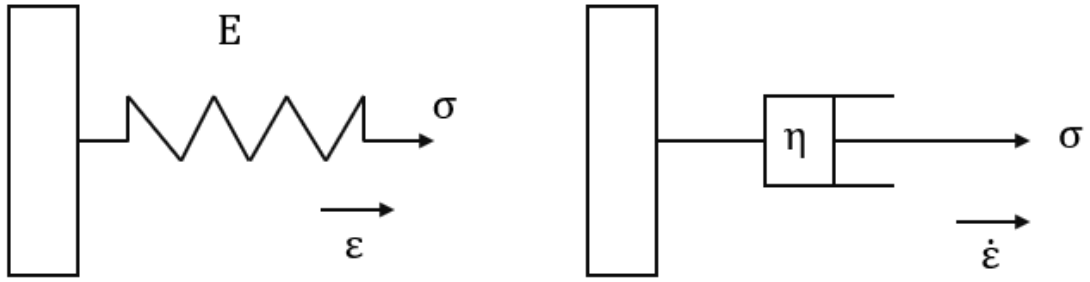


Figure 2.1. A representation of a) spring and b) dashpot.

An elastic material deforms, storing potential energy, and recovers from the deformation like a spring releasing all the stored energy. The elastic modulus (E) for a linearly elastic material relates stresses and strains as:

$$\sigma = E\varepsilon \qquad (2.2)$$

A dashpot is a viscous fluid-like material where the energy of deformation is all lost to frictional forces, and the stress is linearly related to the strain rate.

$$\sigma = \eta\,\dot{\varepsilon} \qquad (2.3)$$

where η is the viscosity.

2.2.1. Viscoelastic models

Two common simple models for viscoelasticity are the Kelvin-Voight model which consists of a spring and a dashpot in parallel configuration (Fig. 2.2 a) and the Maxwell model which consists of a spring and dashpot in series configuration (Fig. 2.2 b). More recently models employing fractional derivatives have been found to better match soft tissue. Here, the three types of models will be reviewed.

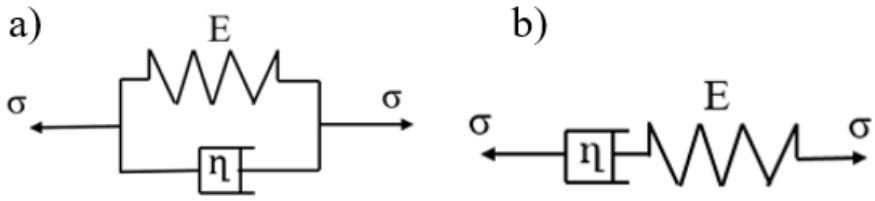


Figure 2.2. a) Kelvin-Voight and b) Maxwell model

2.2.2. Kelvin-Voight model

For the Kelvin-Voight model, the stress applied to the entire system is divided between the spring (σ_s), and the dashpot (σ_d):

$$\sigma = \sigma_s + \sigma_d \quad (2.4)$$

The strain on the dashpot ε_d and the spring ε_s must both equal the system strain due to the parallel configuration, that is,

$$\varepsilon = \varepsilon_d = \varepsilon_s \quad (2.5)$$

The stress-strain relation for the spring and dashpot can be represented as:

$$\sigma_s = E\,\varepsilon_s \quad (2.6)$$

$$\sigma_d = \eta\dot{\varepsilon_d} \quad (2.7)$$

Hence, the relationship between stress and strain for a Kelvin-Voight model is:

$$\sigma = E\varepsilon + \eta\frac{d\varepsilon}{dt} \quad (2.8)$$

A frequency domain relationship can be obtained by applying Fourier transform to equation 2.8:

$$\hat{\sigma}(\omega) = E\,\hat{\varepsilon}(\omega) + \eta\, i\,\omega\,\hat{\varepsilon}(\omega) \qquad (2.9)$$

where $\hat{\sigma}(\omega)$ and $\hat{\varepsilon}(\omega)$ are the Fourier transform of stress and strain respectively.

The ratio of the stress and strain in the frequency domain typically gives the complex modulus for a viscoelastic media.

$$G^*(\omega) = \frac{\hat{\sigma}(\omega)}{\hat{\varepsilon}(\omega)} = E + \eta\, i\,\omega \qquad (2.10)$$

The storage modulus (G') and loss modulus $\left(G^{"}\right)$ can be obtained by separating the real and imaginary part of equation 2.10 respectively:

$$G'(\omega) = E \qquad (2.11)$$

$$G^{"}(\omega) = \eta\,\omega \qquad (2.12)$$

In the Kelvin-Voight model, the storage modulus is independent of frequency and the loss modulus increases linearly with the frequency.

2.2.3. Maxwell model

For the Maxwell model, the stress applied to the entire system acts equally on the spring and dashpot:

$$\sigma_s = \sigma_d = \sigma \qquad (2.13)$$

The resulting strain is the sum of strains in spring and dashpot :

$$\varepsilon = \varepsilon_d + \varepsilon_s \qquad (2.14)$$

Taking a derivative and using the constituents relations, one gets:

$$\frac{d\varepsilon}{dt} = \frac{\sigma}{\eta} + \frac{1}{E}\frac{d\sigma}{dt} \qquad (2.15)$$

$$\eta\frac{d\sigma}{dt} + E\,\sigma = \mathrm{E}\,\eta\,\frac{d\varepsilon}{dt} \qquad (2.16)$$

Equation 2.16 represents a differential equation relating stress and strain for the Maxwell model.

Applying Fourier transform to equation 2.16:

$$(i\omega)\eta\hat{\sigma}\,(\omega) + E\hat{\sigma}\,(\omega) = \mathrm{E}\,\eta\,(i\,\omega)\,\hat{\varepsilon}\,(\omega) \qquad (2.17)$$

and the complex modulus can be expressed as:

$$G^*(\omega) = \frac{iE\eta\omega}{E+i\eta\omega} \qquad (2.18)$$

The storage modulus and loss modulus can then be expressed as:

$$G'(\omega) = \frac{E\,(\eta\omega)^2}{E^2+\,(\eta\omega)^2} \qquad (2.19)$$

$$G^{"}(\omega) = \frac{E^2\,(\eta\omega)}{E^2+\,(\eta\omega)^2} \qquad (2.20)$$

The storage modulus approaches to 0 as $\omega \rightarrow 0$ and to E as $\omega \rightarrow \infty$. The loss modulus approaches to η as $\omega \rightarrow 0$ and to 0 as $\omega \rightarrow \infty$.

2.2.4. Fractional derivative model

Fractional calculus is useful in modelling the response of biological and tissue-like materials such polymers, gels, emulsions, composites and suspensions which exhibit power-law responses to an applied stress or strain. A Fractional derivative model differs from a classical viscoelastic model in its construction such that components like springs or dashpots are replaced by springpots which possess intermediate properties between elastic spring and viscous dashpot [45]. The stress (σ) and strain (ε) in a springpot are related with a fractional order derivative:

$$\sigma = K_\alpha \frac{d^\alpha \varepsilon(t)}{dt^\alpha} = \frac{K_\alpha}{\Gamma(1-\alpha)} \int_0^t (t-a)^{-\alpha}\, \frac{d\varepsilon}{da}\, da \qquad (2.21)$$

where $0 \leq \alpha \leq 1$, K_α is the coefficient of consistence has units of $Pa.(s)^\alpha$ and a is the time shift due to convolution, and Γ is the gamma function. A Semi-Fractional Kelvin Voight (S-FKV)

model consists of a springpot in parallel with a viscous dashpot (Fig. 2.3). The stress-strain relation of a S-FKV Model is given by:

$$\sigma(t) = \eta \frac{d\varepsilon(t)}{dt} + K_\alpha \frac{d^\alpha \varepsilon(t)}{dt^\alpha} \quad (2.22)$$

$$K_\alpha = E\tau^\alpha \quad (2.23)$$

where E is the elastic modulus, τ is the time constant and α is the fractional order. The bounding values of α represent the discrete elements employed in conventional viscoelastic models such as spring $K_\alpha = E$ when $\alpha = 0$; and dashpot $K_\alpha = \eta$ when $\alpha = 1$.

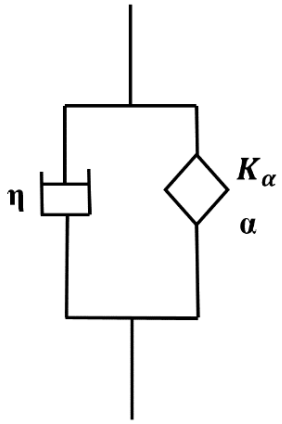


Figure 2.3. Semi-Fractional Kelvin-Voight model.

Applying Fourier transform to equation 2.22 :

$$\hat{\sigma}(\omega) = i\eta\omega\, \hat{\varepsilon}(\omega) + K_\alpha (i\omega)^\alpha \hat{\varepsilon}(\omega) \quad (2.24)$$

Using the identity, $i^\alpha = cos\left(\frac{\alpha\pi}{2}\right) + i\, sin\left(\frac{\alpha\pi}{2}\right)$, one can express the complex modulus as:

$$G^*(\omega) = K_\alpha (\omega)^\alpha cos\left(\frac{\alpha\pi}{2}\right) + i\left[\eta\omega + K_\alpha (\omega)^\alpha sin\left(\frac{\alpha\pi}{2}\right)\right] \quad (2.25)$$

Then the storage modulus G' and loss modulus G'' can be written as:

$$G'(\omega) = K_\alpha (\omega)^\alpha cos\left(\frac{\alpha\pi}{2}\right) \quad (2.26)$$

$$G''(\omega) = \eta\omega + K_\alpha (\omega)^\alpha sin\left(\frac{\alpha\pi}{2}\right) \quad (2.27)$$

Figure 2.4 shows the response of S-FKV model, Maxwell model and Kelvin-Voight model as a function of frequency. S-FKV model shows a power-law increase in the storage and loss modulus with frequency compared to Maxwell and K-V model where power-law behaviour is not observed.

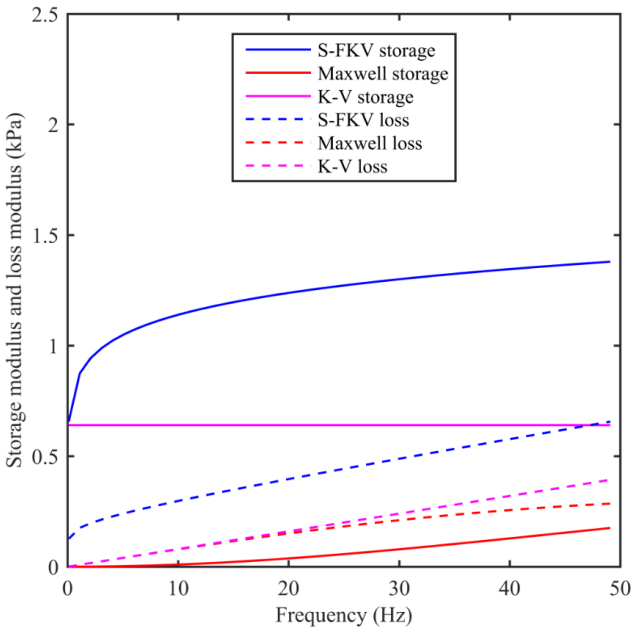


Figure 2.4. S-FKV model vs. common viscoelastic models.

For S-FKV model, the response to a step strain $\in=\in_0 H(t)$ (where $H(t)$ is Heaviside function) results in a relaxation modulus.

$$G(t) = \frac{\sigma(t)}{\epsilon_0} = \eta\,\delta(t) + K_\alpha \frac{t^{-\alpha}}{\Gamma(1-\alpha)} \qquad (2.28)$$

where Γ is the gamma function.

2.3 METHODS OF MECHANICAL TESTING

2.3.1. Uniaxial Compression

A typical testing scenario for uniaxial compression is shown in Fig. 2.5. A sample is placed between the top and bottom plates, a load F is applied to the sample and the displacement δL is measured. The nominal value of stress is estimated as $\sigma = F/A$, where A is the cross-sectional area of the sample. The strain is given by $\epsilon = \delta L/L$, where L is the original length of the sample. In the uniaxial tests reported here, a Universal Testing Machine (Instron, 5582) was used for all the measurements.

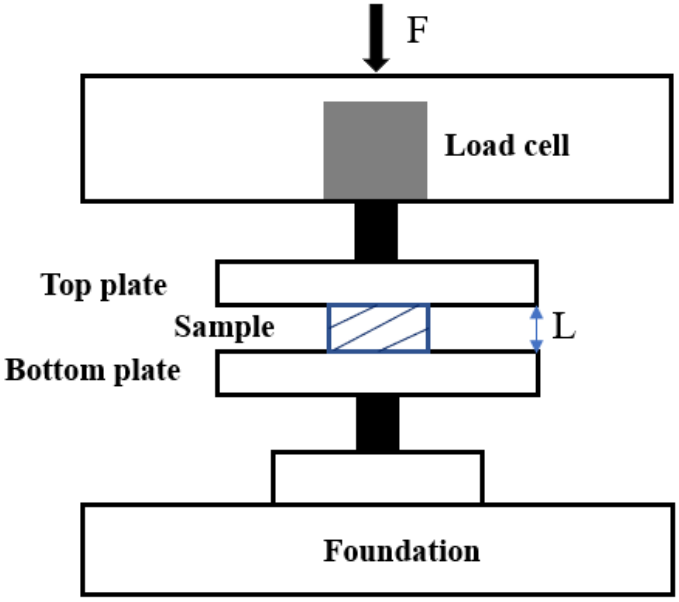


Figure 2.5. Schematic of a uniaxial compression test

2.3.2. Oscillatory Shear

The storage modulus and loss modulus are measured using an oscillatory shear testing. This device consists of a two-plate system (Fig. 2.6) such that the lower plate is fixed and the upper plate is rotated at a fixed amplitude and frequency. The rheometer measures the torque applied

and the angle of deformation, and converts them into shear stress and shear strain respectively. The ratio of shear stress and shear strain gives the complex modulus G^*, and the phase angle δ between the stress and strain is used to obtain the storage modulus G' and loss modulus $G^{"}$.

$$G' = G^* \cos \delta \qquad (2.29)$$

$$G^{"} = G^* \sin \delta \qquad (2.30)$$

The oscillatory shear tests were performed by varying the shear strain amplitude and frequency. All the measurements were done using a stress-controlled rheometer (Physica MCR, 301).

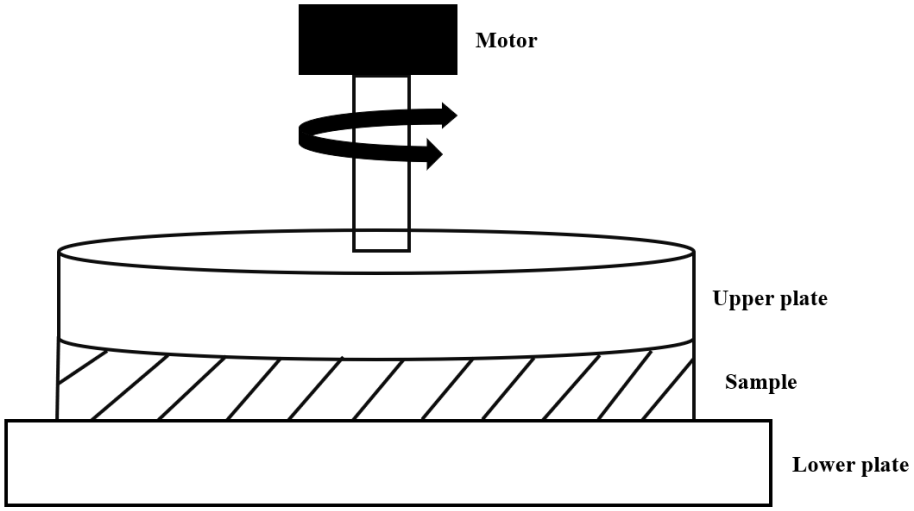


Figure 2.6. Schematic of a rheometer.

2.3.3. Oscillatory Nanoindentation

A nanoindenter consists of a coil-magnet assembly along with a leaf spring, phase lock amplifier and a capacitive gauge (Fig. 2.7). Figure 2.8 shows the agarose samples placed in the nanoindenter testing rig. The indenter column is supported by two leaf springs with a lateral stiffness higher than the vertical stiffness effectively limiting the system to 1 degree of freedom (i.e. vertical motion). The load is controlled by electromagnetic actuation, and as the load is transmitted through the filters in the phase lock amplifier, a phase shift is introduced. A three-

plate capacitive arrangement measures the displacement of the indenter. The Nanoindenter G200 setup equipped with a DCM-II head (Keysight Technologies, Chandler, Arizona) applies a pre-compression into the sample, oscillates at the user-defined frequency and determines the storage modulus and loss modulus. All measurements were performed using a flat punch cylindrical indenter of diameter 100 μm and the oscillation frequency of the indenter was varied. Equations 2.31 and 2.32 describe the storage modulus and loss modulus in terms of contact stiffness (S), contact damping ($D\omega$), radius of flat cylindrical punch (a) and Poison's ratio (ν) [46].

$$G' = \frac{S(1-\nu)}{4a} \qquad (2.31)$$

$$G'' = \frac{D\omega(1-\nu)}{4a} \qquad (2.32)$$

Equations 2.31 and 2.32 are based on the assumption that the contact area between the specimen and indenter remains constant [47]. Oscillatory nanoindentation has previously been used as a mechanical testing method for soft materials such as hydrogels [46] and cartilage [48]. Oscillatory nanoindentation has an advantage over rheometer that the indenter can be oscillated at frequencies up to 110 Hz. However a nanoindenter extracts viscoelastic properties at the micro-length scale due to which the bulk response of tissue is not known.

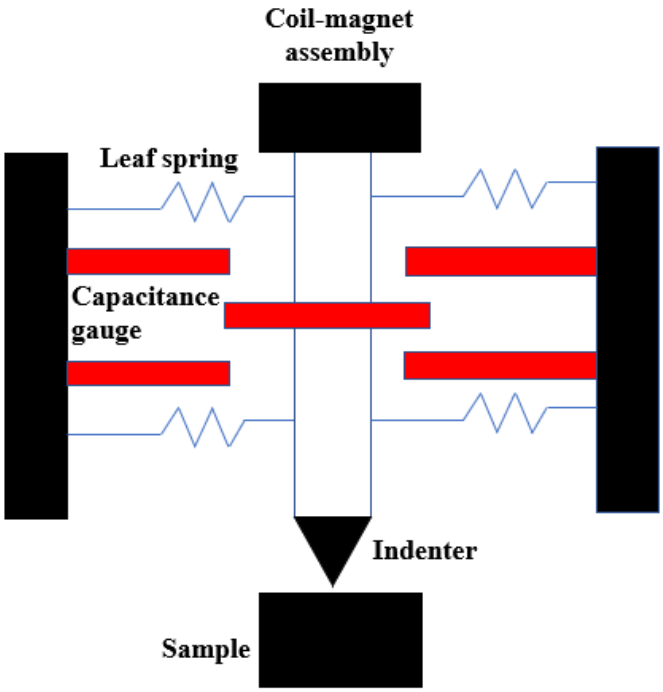


Figure 2.7. Schematic of a Nanoindenter

a) b)

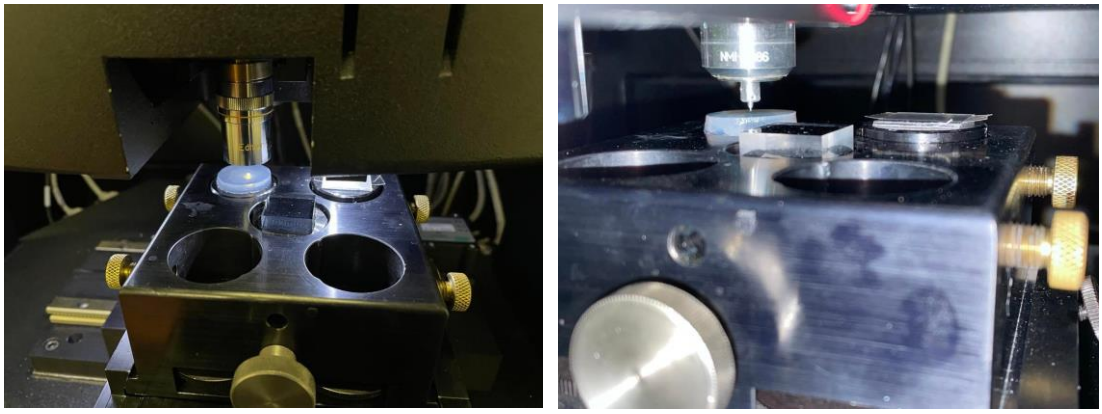


Figure 2.8. a) Agarose samples placed in the testing rig and indent points selected on the samples using a microscope b)Oscillatory nanoindentation tests performed using a flat cylindrical punch

2.4. UNIAXIAL COMPRESSION

Porcine kidneys were collected from a local butcher's shop and the pigs were sacrificed within 36 hours prior to the collection. Porcine kidneys were tested within 2 hours after collection. Figure 2.9 shows a cross-sectional image of a pig's kidney. Samples were extracted from the renal cortex due to their uniform texture [20]. Surgical blades were used to extract samples with a length of 11.5± 1.7 mm, a width of 10.3± 1.4 mm and a height of 3.4± 0.4 mm. 15 renal cortical samples were extracted from 5 kidneys (n=3 per kidney). The cross head was lowered until a contact force of 0.1 N was established. Then a uniaxial test was performed with a fixed speed of 0.5 mm/min. Elastic properties of porcine kidneys were investigated until rupture.



Figure 2.9. Cross-section of a pig's kidney

Figure 2.10 shows the average stress vs. strain curve from 15 samples upto 2% strain at a cross-head velocity of 0.5 mm/min. It can be observed that the stress-strain curve starts from a non-zero stress value at zero strain. This corresponds to the initial contact force of 0.1 N established between the top plate and specimen. An elastic modulus of 44.8±22.6 kPa was obtained from experimental data until 2% strain for 15 porcine kidney samples. This lies in agreement with the elastic modulus of 48.6±7.3 kPa obtained by Opik et. al. [49] where uniaxial tests were performed on the renal medulla up to 25% strain. Our experimental data also resembles with

the elastic modulus of 47 ± 6 kPa obtained by Sommerer et. al. [50] where transient elastography was performed on ex-vivo porcine kidneys.

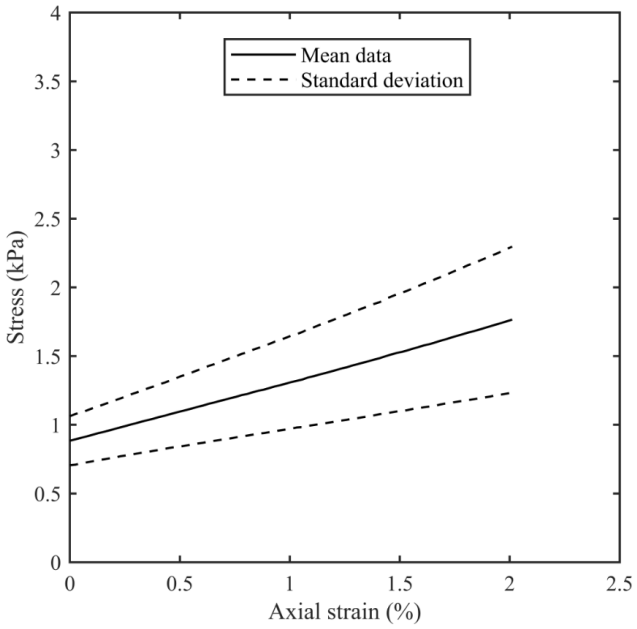


Figure 2.10. Stress vs. strain for renal cortex samples (n=15) up to 2% strain.

Figure 2.11 shows the stress-strain plot for 15 samples. A non-linear stress vs. strain curve is obtained up to a rupture stress of 250 kPa and a rupture strain of 43%. A Mooney-Rivlin hyperelastic model was fitted to the stress-strain curve. Eq. 2.33 defines the strain energy potential (W) for Mooney-Rivlin model for incompressible materials.

$$W = \sum_{i+j=1}^{N} C_{ij} \, (I_1 - 3)^i \, (I_2 - 3)^j \qquad (2.33)$$

where I_1 is the first order strain invariant , I_2 is the second order strain invariant, and C_{ij} are the material parameters.

A second order Mooney-Rivlin model fitted the non-linear stress-strain response with a correlation coefficient better than 0.99, see Fig. 2.11. The material parameters computed from our data were as follows : C_{10}= 1.24 MPa, C_{01}= -1.26 MPa, C_{20}= -0.65 MPa, C_{02}= -1.20 MPa and C_{11}= 1.10 MPa. Considering the variability in animal tissues, these values are in similar range compared to the material parameters calculated by [51] using the second order Mooney-Rivlin model: C_{10}= 0.28 MPa, C_{01}= 0.29 MPa, C_{20}= -0.29 MPa, C_{02}= -2.30 MPa and C_{11}= 2.13

MPa. The average rupture stress of ~250 kPa and rupture strain of ~43% obtained from our experimental data were similar to the values of rupture stress ~250 kPa and rupture strain ~50% obtained by Farshad et. al. [52]. Elastic modulus of 920±270 kPa was obtained from our experimental data in the region of 25% to 35% strain which lies in agreement with 1160±100 kPa obtained by Umale et. al. [51] where compression tests on 60 renal cortex samples from 12 porcine kidneys were performed at a static speed of 0.05 mm/s.

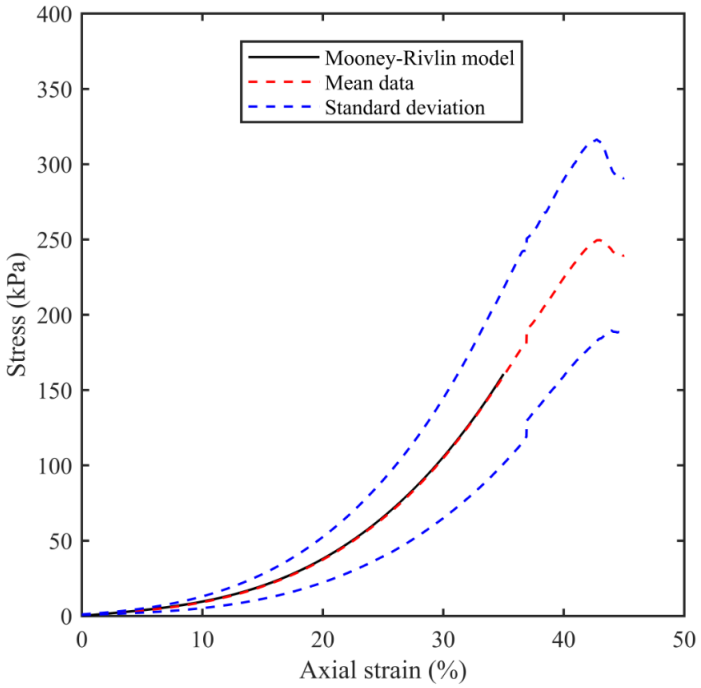


Figure 2.11. Stress vs. strain plot with standard deviation for 15 renal cortex samples along with Mooney-Rivlin fit.

2.5. RHEOLOGICAL TESTS

Porcine kidneys were collected from a local butcher 36-48 hours after slaughter. All samples were tested within 2 hours after collection. Figure 2.12 shows a representative image of a porcine kidney that was measured in the study. A cork borer was used to extract 25 mm diameter samples and surgical blades were used to dissect slices with ~5 mm thickness. One sample per kidney from the middle region was extracted. The thickness of samples was 5±0.1 mm (n=5) for the strain sweep, 5.3±0.2 mm (n=5) for the frequency sweep and 5.4±0.8 mm (n=3) for the relaxation tests.

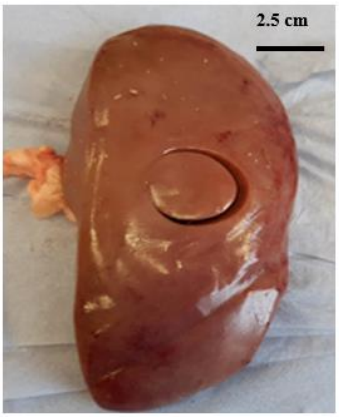


Figure 2.12. Sample extracted from the middle region of the porcine kidney for rheological tests.

2.5.1. Strain sweep

The storage modulus and loss modulus were provided by the rheometer using strain sweep tests as the strain amplitude was increased from 0.01% to 10% at a frequency of 1 Hz. Figure 2.13 shows the dependency of both moduli as a function of strain for different porcine organs. The horizontal sections are consistent with the tissue acting as a linear viscoelastic material upto 0.3%. The storage modulus of 0.50±0.03 kPa and loss modulus of 0.10±0.02 kPa is obtained at 0.1% strain amplitude and 1 Hz frequency.

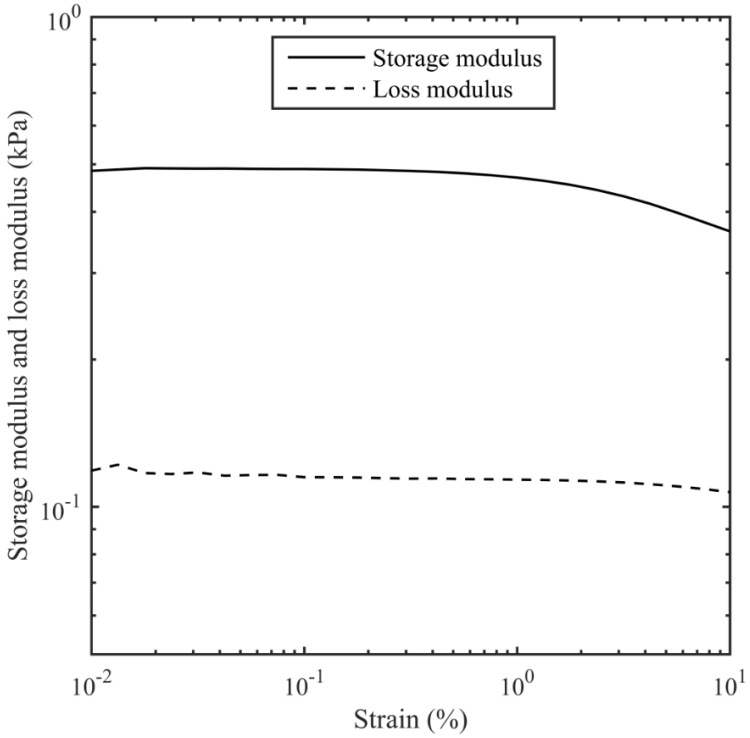


Figure 2.13. Storage modulus and loss modulus as a function of strain amplitude for 5 porcine kidneys. Measurements were carried out at 1 Hz.

2.5.2. Frequency sweep

For the frequency sweep experiments, the strain amplitude was held at 0.1% and the frequency varied from 0.1 Hz until inertial effects appeared to impact the results. The presence of inertial effects can be seen by the reduction in storage modulus, see Fig. 2.14. The upper limit of frequency was 9.5 Hz.

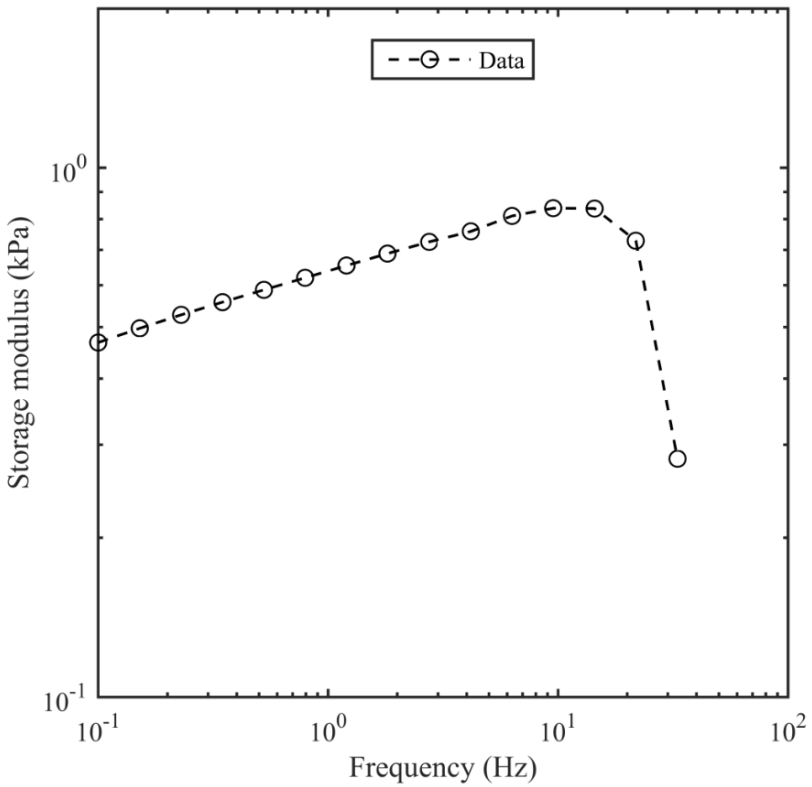
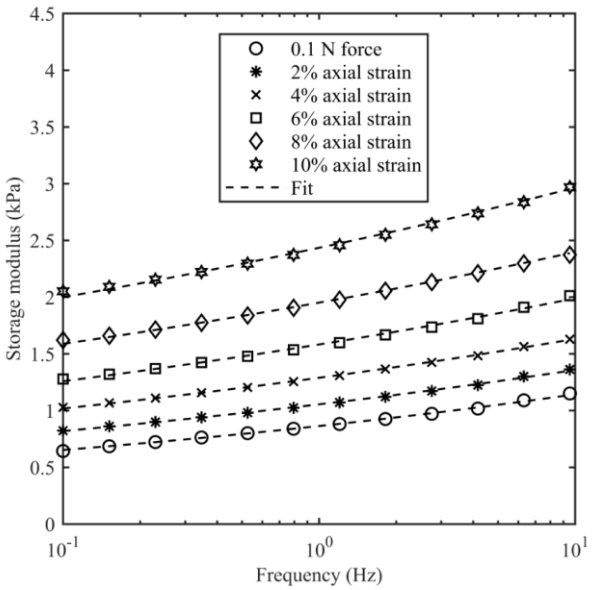


Figure 2.14. The storage modulus of the porcine kidney at a contact force of 0.1 N. Depending on the tissue, a dip in storage modulus can be seen near 10 Hz which is indicative of inertial effects affecting the measurement of modulus.

The S-FKV model (Eq. 2.26 and 2.27) was fit to the data using the least square fit function in MATLAB, in order to determine K_α, α and η. This was repeated for each axial strain. At a contact force of 0.1 N, the axial stress is $\sigma \approx$ 200 Pa which for a typical elastic modulus of 45 kPa (see Sec. 2.4) results in an axial strain of ~0.5%. The absolute axial strain is therefore 0.5% higher than the values given on the figures. Figure 2.15 shows the data and model fit of the storage modulus and loss modulus of kidney samples for a range of axial strains, and it can be seen that there is a good agreement over the range of frequencies and strains considered here with a correlation coefficient better than 0.99. The parameters obtained at 0.1 N were: K_α: 0.88±0.25 kPa.(s)$^\alpha$, α: 0.120±0.008 and η: 8±3 Pa.s; and at 10% axial strain were : K_α: 2.50±0.74 kPa.(s)$^\alpha$, α: 0.090±0.012 and η: 22±8 Pa.s. It can be observed that K_α, α and η change with the axial strain.

a)



b)

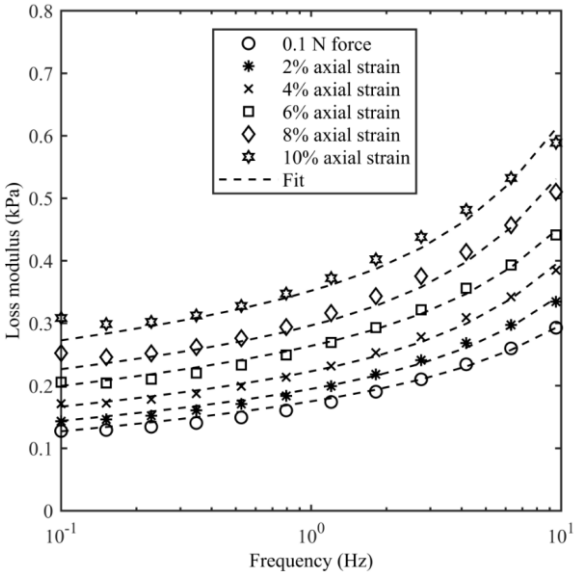


Figure 2.15. (a) Storage modulus, and (b) loss modulus of kidney samples as a function of frequency and axial strain. Axial strain was varied up to 10%.

The storage modulus and the loss modulus increased monotonically with the axial strain (ε_A) and frequency. Figure 2.16 shows the dependence of K_α as a function of ε_A and it can be observed that there appears to be a linear relationship with the axial strain. The data was fit to the expression:

$$K_\alpha = k_0(1 + b\varepsilon_A) \qquad (2.34)$$

where k_0 and b are the fitting values, and ε_A is the axial strain. In this case, an offset of 0.5% is added to all the axial strain values to account for the 0.1N contact force. Parameters from a linear fit of Eq. 2.34 in the plot of K_α as a function of ε_A were: k_0: 0.7±0.2 kPa.(s)$^\alpha$ and b: 0.23±0.07.

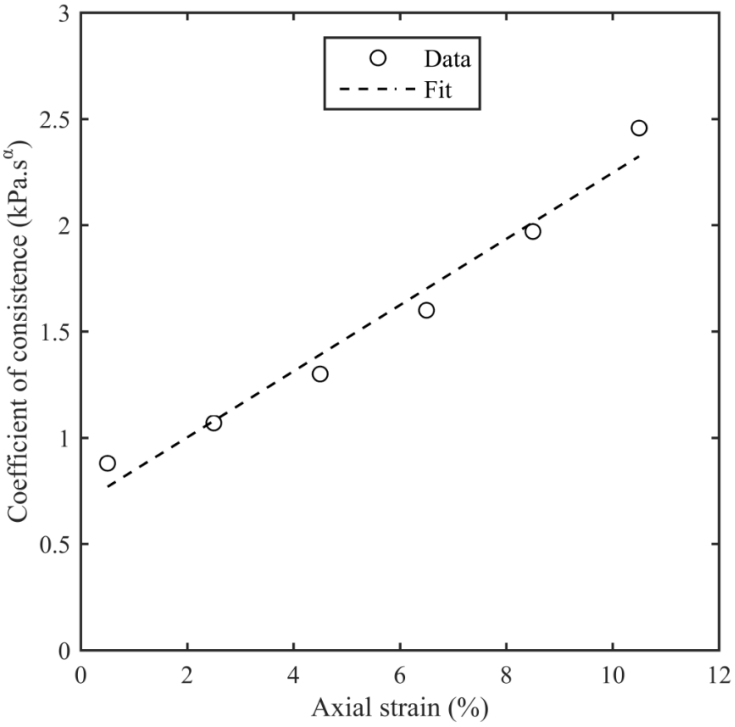


Figure 2.16. Coefficient of consistence (K_α) as a function of axial strain (ε_A) for the porcine kidney.

The data reported here were all taken at 20°C, however living tissue would be at body temperature, normally 37°C. The effect of this change in temperature was assessed by performing frequency sweep tests on kidney samples immersed in PBS solution at 37°C by adjusting the Peltier plate temperature in the rheometer. The storage modulus of kidney samples at 1.2 Hz varied less than 10% as the temperature was increased from 20°C to 37°C and the loss modulus by 20%, see Fig. 2.17.

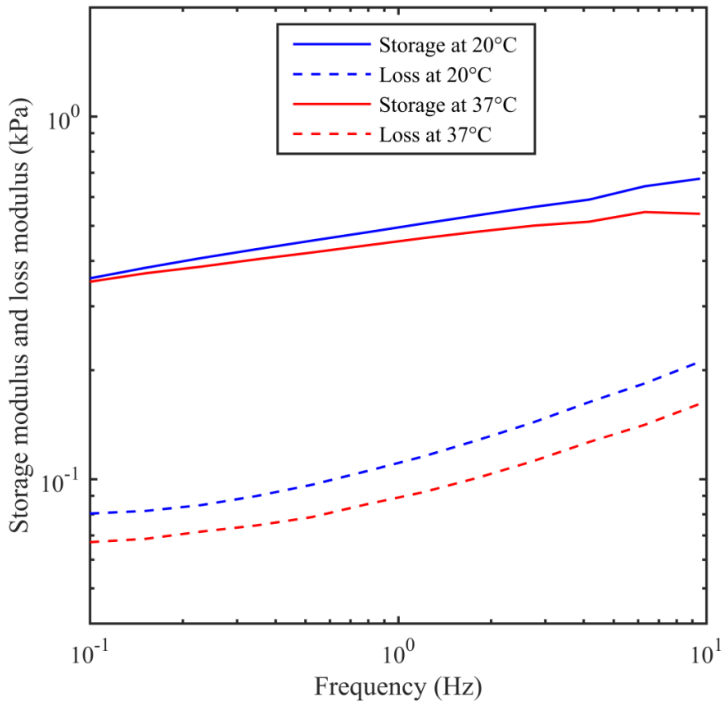


Figure 2.17. Storage modulus and loss modulus as a function of frequency at 20°C and 37°C.

2.5.3. Stress relaxation

For the stress relaxation test, the samples were compressed to an axial strain of 0.5% and at time t=0, they were subjected to a step shear strain of 0.1%. The shear stress was then measured every second for 10 seconds. The measured stress was compared to predictions based on the S-FKV model using parameters extracted from Eq. 2.26 and 2.27. Figure 2.18 represents the

experimental and predicted stress relaxation. It can be seen that the predicted response matches the time evolution of the measurements but it over estimates the amplitude by about 26%.

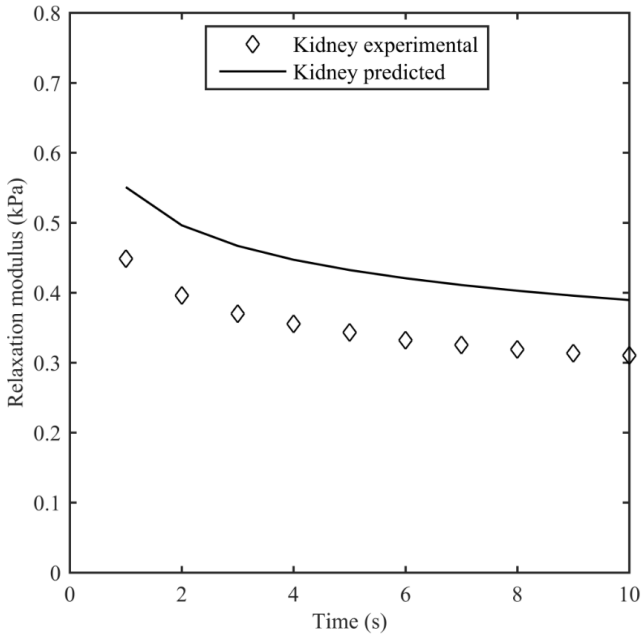


Figure 2.18. Measured stress relaxation modulus and predicted stress relaxation modulus using S-FKV model.

2.6. NANOINDENTATION TEST

Porcine kidneys were collected from a local butcher in Oxford and these kidneys were extracted from pigs sacrificed 24 hours prior to collection. The kidneys were cooled on ice and sealed for transport from Oxford to University of Liverpool which took 24 hours. After collection at the University of Liverpool, samples were extracted from the middle region of the kidney. Surgical blades were first used to extract ~4-5 mm thick rectangular samples from the renal cortex region. A biopsy punch of diameter 5 mm was used to extract cylindrical samples. Four samples were extracted from four pigs (n=1 per pig) and three indents per sample were performed.

Nanoindentation tests were conducted using a Nanoindenter G200 setup, see Sec. 2.3.3. A flat punch cylindrical indenter of diameter 100 μm was used to perform the tests at 10 Hz, 40 Hz, 80 Hz and 110 Hz. All tests were conducted at an oscillation amplitude of 500 nm and pre-

compression at 5 μm. The upper frequency limit was set to 110 Hz since it is near the resonant frequency of the actuator above which the uncertainties in both stiffness and damping increase significantly [46]. Nanoindenter extracted the storage modulus and loss modulus values at each frequencies. Figure 2.19 represents the storage modulus and loss modulus as a function of frequency from oscillatory nanoindentation tests. Storage modulus varied from 25 kPa to 45 kPa while loss modulus varied from 9 kPa to 14 kPa over the frequency range tested.

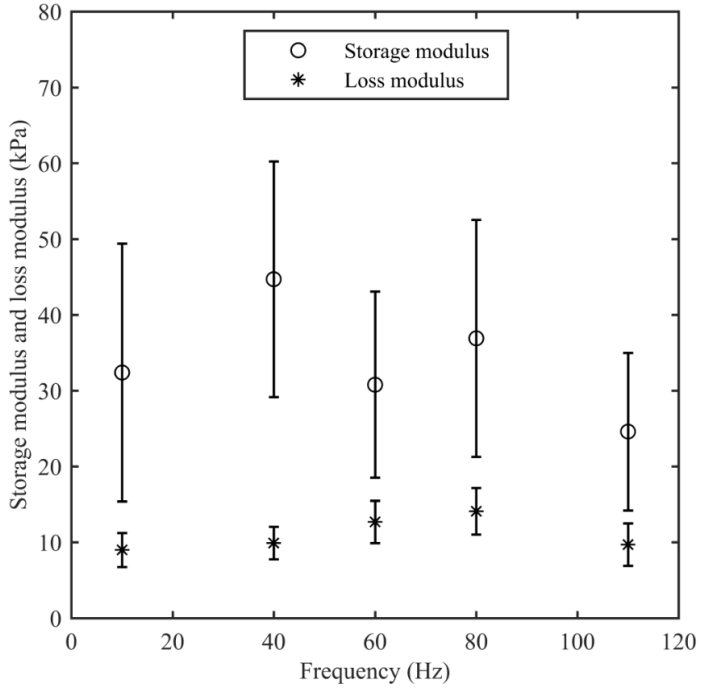


Figure 2.19. Storage modulus and loss modulus as a function of frequency from nanoindentation tests on porcine kidneys.

2.7. DISCUSSION AND CONCLUSION

This chapter reported uniaxial, shear and nanoindentation stress-strain measurements of porcine kidney tissue. The uniaxial tests gave a non-linear stress-strain response with a rupture stress of 250 kPa at 43% strain. A second-order Mooney-Rivlin model fitted the stress-strain data with a correlation coefficient better than 0.99. Oscillatory Shear tests showed that the storage modulus and loss modulus remained steady during strain sweep tests from 0.01% to 0.3% shear strain suggesting that porcine kidneys exhibit linear viscoelastic behaviour in this region.

Frequency sweep tests were performed from 0.1 Hz up to 9.5 Hz for a range of strain amplitudes and for a range of pre-compression. A monotonic increase in both the storage modulus and loss modulus as a function of frequency and the axial strain was observed.

In our study, an S-FKV model was fitted to the frequency sweep data at different axial strains for all the porcine organs with a correlation coefficient better than 0.99. The coefficient of consistence (K_α) increased monotonically with the axial strain. One possible explanation for this is that the pre-compression forces the interstitial fluid out of the tissue matrix and leading to a more solid-like behaviour. Also, the S-FKV model shows an increase in viscosity (η) by a factor of ~3 when the axial strain is increased to 10%. This implies a higher fluid movement with the increase in axial strain. The predictive power of the S-FKV model was tested by comparing the predicted response to a step shear strain with the measured response. The stress relaxation amplitudes of the predictions and measurements were within 26%.

Nicolle et. al. [53] performed rheological tests on fresh porcine kidneys (n=11). Frequency sweep tests were performed between 0.1 Hz and 4 Hz at 0.1% strain. A power-law behaviour was observed such that the storage modulus was ~1.8 kPa and loss modulus was ~0.2 kPa at 0.1 Hz. Our experimental value of storage modulus was 72% lower than [53] and our loss modulus was almost half of the value reported by [53]. This is potentially due to the variability in mechanical properties of animal tissues. The fitted S-FKV model was used to predict the shear modulus of porcine kidneys at frequencies reported in the literature. Table 2.1 compares values reported in the literature with the values predicted by the S-FKV model. The predicted values are in agreement with the literature values considering that the S-FKV data was extrapolated from < 10 Hz measurements and compared to 100's Hz in other data.

Technique	Study	Frequency (Hz)	Average Shear Modulus (kPa)	Semi-Fractional Kelvin-Voight Model (kPa)
Rheometry	Nicolle et. al. [53]	0.1 to 4	2.00	0.66 to 1.02
Rheometry	Nasseri et. al. [20]	0.01 to 20	5.10	0.50 to 1.24
Magnetic Resonance Elastography	Kruse et. al. [54]	75 to 300	1.67	1.45 to 1.71
Shear Wave Dispersion Ultrasound Vibrometry	Amador et. al. [55]	50 to 500	2.30	1.38 to 1.82

Table 2.1. Shear Modulus reported in the literature compared to the S-FKV model prediction.

Nanoindentation tests resulted in a shear storage modulus of 25 kPa at a frequency of 10 Hz. The storage modulus and loss modulus has a higher standard deviation since different indents or locations on the tissue samples were selected at different frequencies and soft tissues have an inhomogeneous structure [56]. Mattice et al. [57] performed indentation tests using 5.55 mm spherical indenter on kidney samples of twelve differently aged pigs. The instantaneous shear modulus varied from ~6 kPa to ~10 kPa. Considering the variability in reported properties for biological tissues our experimental data is consistent. The storage modulus at the micro-level was 50 to 90 times higher than the storage modulus at the macro-level. This is potentially due to the connective tissue structure as actin, elastin and collagen dominating at the micro-level compared to the macro-level where interstitial fluid dominates. Nanoindentation tests probe mechanical properties at a relatively smaller volume, and hence the frequency-dependent effects associated with large-scale deformation were not present in the nanoindentation data.

CHAPTER 3: MECHANICAL TESTING OF PORCINE TISSUES

3.1. INTRODUCTION

The shear modulus of abnormal tissues is stiffer than the normal tissue, and techniques such as Shear Wave Elastography and Magnetic Resonance Elastography have clinical applications in diagnosis of liver fibrosis [58], characterisation of brain lesions [59] and cardiac diseases such as myocardial infarction [60], and change in aortic stiffness [61]. In Magnetic Resonance Elastography, an external acoustic driver is used to create shear waves and the tissue stiffness is measured by correlating the shear strain waves with the shear storage modulus. In Shear Wave Elastography, shear waves are induced through an acoustic radiation force and the shear wave speed is captured using an ultrasound imaging. The storage modulus in the tissue is computed from the shear wave speed [62].

Fractional viscoelastic models have previously been applied to the brain [63], liver [64-67], and arteries [68,69]. These models can be helpful in predicting the viscoelastic properties of porcine organs such as the storage modulus and loss modulus during elastography techniques. In this chapter, the viscoelastic properties of porcine heart, liver, brain and aorta were measured, their dynamic properties were extracted until the inertial effects affected the measurements and fractional viscoelastic models were used to fit their power law behaviour. The viscoelastic model was later used to predict the relaxation behaviour of the porcine organs and a comparison with experimental data was performed. The fractional viscoelastic models were also extrapolated to other frequencies, and compared with the elastography techniques and data available in literature.

3.2. MATERIALS AND METHODS

Porcine heart, liver and brain were supplied by a local butcher in Oxford 48-72 hours after slaughter. All organs were tested within 2 hours after collection. A cork borer was used to extract 25 mm diameter samples of heart, liver and brain and surgical blades were used to dissect slices with varying thickness (shown in Table 3.1). One sample per organ was extracted for all the tests.

Porcine aorta was acquired from an abattoir and transported to the lab in a sealed package on dry ice. Disc shaped samples (8 mm in diameter and ~1.5 mm thick) were extracted from the thoracic region of the aorta from three pigs for frequency sweep and from arch, ascending, proximal descending, mid-descending and distal descending regions from one pig for strain sweep. Figure 3.1 shows representative images of the tissues that were measured in the study.

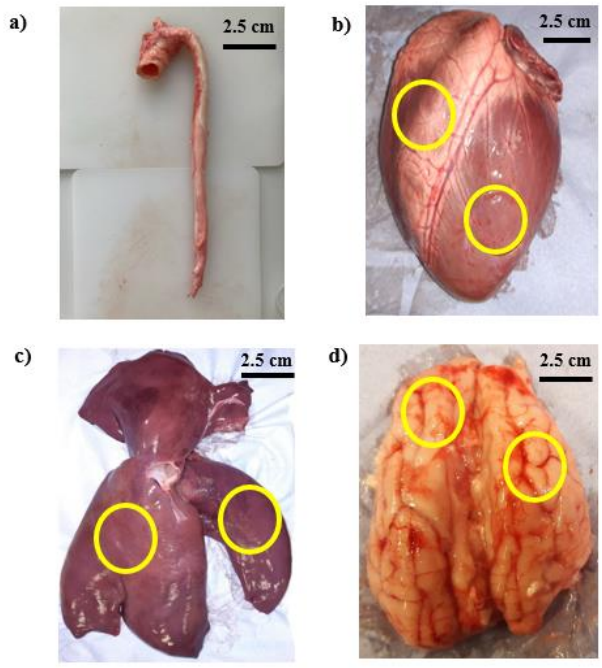


Figure 3.1. Images show porcine tissues and location from where samples were removed a)Aorta b) Left and right ventricle of Heart c) Left and Right lobe of Liver d) Frontal and parietal lobe of Brain.

Porcine Organ	Sample Thickness (Strain Sweep)	Sample Thickness (Frequency Sweep)	Sample Thickness (Relaxation Test)
Heart (n=4) [left and right ventricle]	5.9±0.3 (n=4)	5.9±0.4 (n=4)	6±0.4 (n=4)
Liver (n=4) [left and right lobe]	5.8±0.3 (n=4)	5.3±0.1 (n=4)	5.8±0.5 (n=4)
Brain (n=12) [frontal and parietal lobe of cerebrum along horizontal plane]	5.6±0.6 (n=4)	5.5±1.0 (n=4)	6.1±1.0 (n=4)
Aorta (n=4)	2.4±0.4 (n=5)	1.4±0.2 (n=9)	-

Table 3.1. Thickness of porcine tissue samples used for strain sweep, frequency sweep and relaxation tests. All dimensions are in mm.

The locations for samples chosen were partially in order to provide samples that were as homogenous as possible but also had clinical relevance. In heart, both left and right ventricle are sites of myocardial infarction. Hepatic fibrosis occurs in both left and right lobe of the liver. Stiffening can occur anywhere in the aorta and thus samples from aorta included arch, ascending, proximal descending, mid-descending and distal descending regions. Samples were extracted from the frontal lobe of the brain since it is the largest lobe in human brain and the most common region for traumatic brain injury [70]. The parietal lobe integrates information on proprioception, touch, space navigation, and language processing, and forms an important part of the somatosensory cortex [71]. Lesions in parietal lobe can lead to disorders in information processing [72].

3.3. RESULTS

3.3.1. Strain sweep

The strain amplitude was increased from 0.01% to 10% at a frequency of 1 Hz and the storage modulus and loss modulus were provided by the rheometer. Figure 3.2 shows the storage

modulus and loss modulus as a function of strain for the four different porcine tissues. The horizontal sections are consistent with the tissues acting as a linear viscoelastic material. Table 3.2 shows the storage modulus and loss modulus at 0.1 % strain amplitude which is within the linear viscoelastic region.

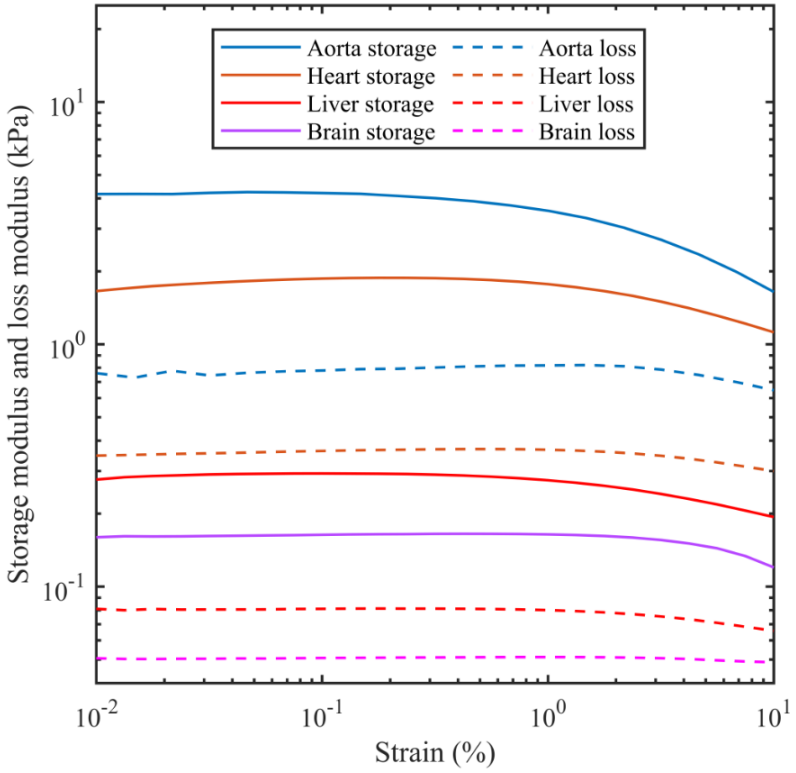


Figure 3.2. Storage modulus and loss modulus as a function of strain amplitude for porcine tissues. Measurements were carried out at 1 Hz.

Porcine organs	**Storage Modulus (kPa)**	**Loss Modulus (kPa)**
Heart	1.90±0.50	0.40±0.10
Liver	0.30±0.08	0.08±0.02
Brain	0.20±0.03	0.050±0.006
Aorta	4.20±1.40	0.80±0.10

Table 3.2. The storage modulus and loss modulus for different porcine tissues at 0.1% shear strain, and 1 Hz frequency. Measurements were carried out at a contact force of 0.1 N.

3.3.2. Frequency sweep

Figure 3.3 shows the measured storage modulus as a function of frequency from 0.1 Hz up to a frequency where inertial effects were present. The data was obtained for a strain amplitude of 0.1%, to be within the linear region and the samples were pre-compressed until the axial strain of 10%. The reduction in storage modulus shows the presence of inertial effects. The upper limit of frequency was 1.2 Hz for aorta, 9.5 Hz for heart, 4.2 Hz for liver and 2.8 Hz for brain.

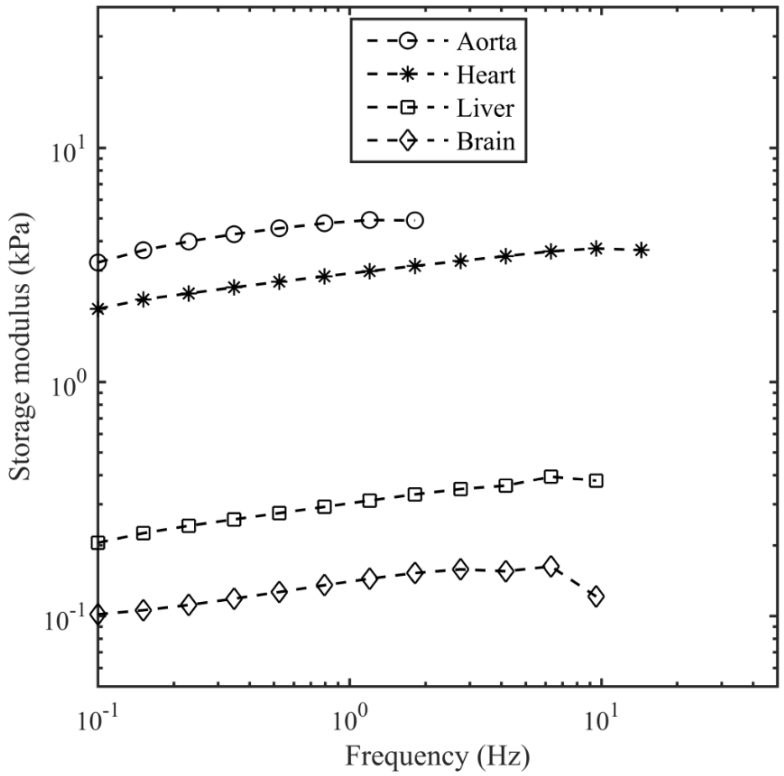


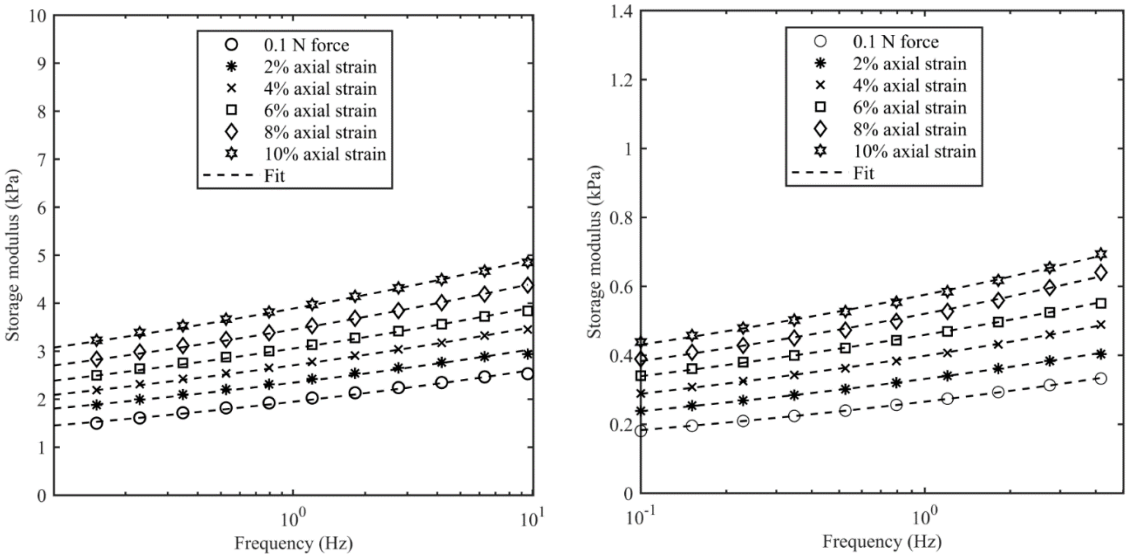
Figure 3.3. Storage modulus of porcine organs at a contact force of 0.1 N. Depending on the tissue, a dip in storage modulus can be seen near 10 Hz which is indicative of inertia.

The Semi-Fractional Kelvin Voight (S-FKV) model (Eq. 2.26 and 2.27) was fit to the heart, liver and brain data using the least square fit function in MATLAB, in order to determine K_α, α and η. At a contact force of 0.1 N, the axial stress is $\sigma \approx 200$ Pa which for a typical elastic modulus of 45 kPa (see Sec. 2.4) results in an axial strain of ~0.5%. Figures 3.4 and 3.5 shows the data and model fit of the storage modulus and loss modulus of porcine heart, liver and brain for a range of axial strains, and it can be seen that there is a good agreement over the range of frequencies and strains considered here with a correlation coefficient better than 0.99. The initial axial strain was based on a contact force of 0.1 N which corresponds ~0.5% strain for porcine organs. The raw data and fitted parameters for all organs are given in the appendix. Table 3.3 gives the fitted parameters of Eq. 2.26 and 2.27 in all porcine organs.

Porcine organs	K_α **[kPa.(s)$^\alpha$]**	**α**	**η [Pa.s]**
Heart	2.00±0.64	0.130±0.004	10.30±6.00
Liver	0.27±0.06	0.160±0.016	9.70±1.80
Brain	0.25±0.03	0.160±0.005	10.00±2.50

Table 3.3. S-FKV model parameters for different organs at a contact force of 0.1 N.

a) b)



c)

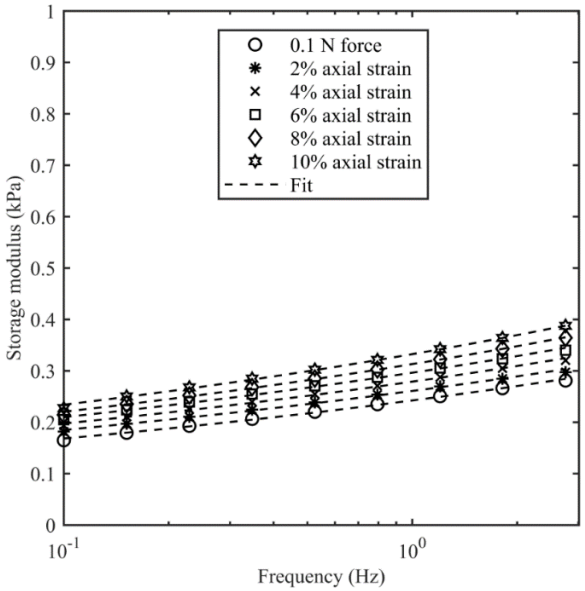
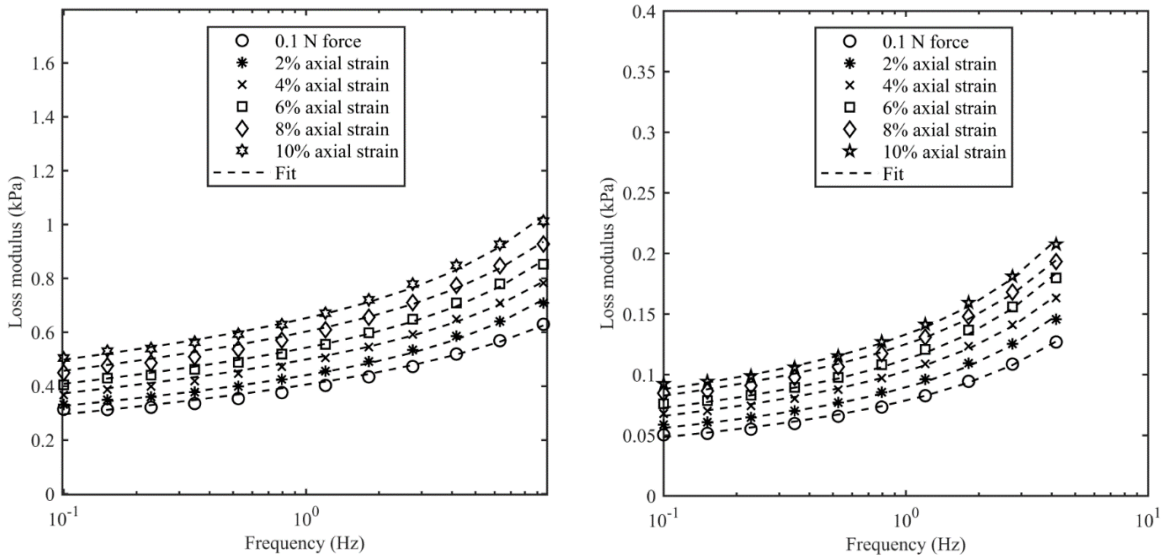


Figure 3.4. Storage modulus of Porcine a)Heart , b)Liver, and c)Brain as a function of frequency and axial strain. The dashed line shows S-FKV model fit and the contact force of 0.1 N corresponds to ~0.5% axial strain.

a) b)



c)

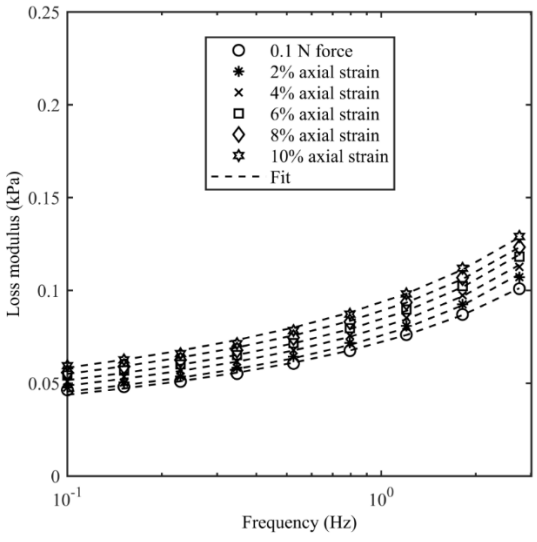


Figure 3.5. Loss modulus of Porcine a)Heart , b)Liver, and c)Brain as a function of frequency and axial strain. The dashed line shows S-FKV model fit and the contact force of 0.1 N corresponds to ~0.5% axial strain.

The storage modulus and the loss modulus increased monotonically with the axial strain and frequency for all three porcine organs. Figure 3.6 shows the dependence of K_α as a function of ε_A, and it can be observed that there appears to be a linear relationship with the axial strain. The data was fit to the expression:

$$K_\alpha = k_0(1 + b\varepsilon_A) \qquad (3.1)$$

where k_0 and b are the fitted values, and ε_A is the axial strain. Table 3.4 gives the parameters from the linear fit of Eq. 3.1 in all porcine organs. An offset of 0.5% is added to all the values of axial strains since the strain measurement is relative to 0.1 N contact force. Table 3.5 shows that α reduces by 23% in heart, 19% in liver and 6% in brain and η increases by 149% in heart, 80% in liver and 23% in brain as the axial strain is increased to 10%.

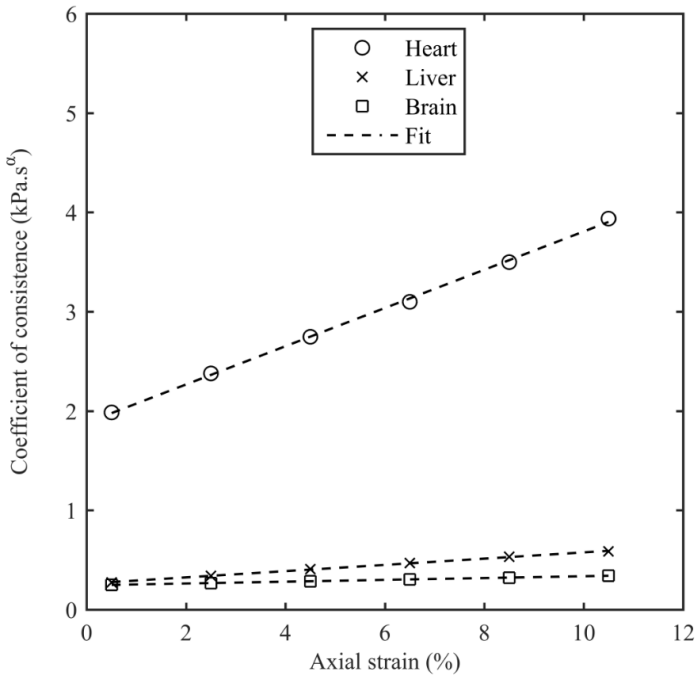


Figure 3.6. Coefficient of consistence (K_α) as a function of axial strain (ε_A) for different porcine organs.

Parameters	Heart	Liver	Brain
k_0 [kPa.(s)$^{\alpha}$]	1.900±0.600	0.260±0.050	0.250±0.030
b	0.100±0.032	0.120±0.020	0.040±0.003
α	0.130±0.004	0.160±0.016	0.160±0.005

Table 3.4. Parameters from linear fit in the plot of K_{α} as a function of ε_A.

Parameters	Heart	Liver	Brain
α at 0.5% axial strain	0.130±0.004	0.160±0.016	0.160±0.005
α at 10% axial strain	0.100±0.020	0.130±0.008	0.150±0.008
η at 0.5% axial strain [Pa.s]	10.300±6.000	9.700±1.800	10.000±2.500
η at 10% axial strain [Pa.s]	25.600±9.000	17.500±4.500	12.300±2.800

Table 3.5. S-FKV model parameters at 0.5% axial strain and 10% axial strain for three porcine organs.

Figure 3.7 shows both the storage modulus and loss modulus as a function of frequency for the aorta. It can be seen that there is a monotonic increase in the storage modulus of aorta from 6.9 kPa at 0.1 Hz to 9.8 kPa at 1.2 Hz while the change in loss modulus is marginal. Parameters obtained from springpot fit are: K_{α}= 9.64±3.34 and α=0.12±0.04 at a contact force of 0.1 N. Dashpot was removed from the S-FKV model since the loss modulus changed marginally with the frequency and springpot fitted the frequency response with a correlation coefficient higher than 0.99.

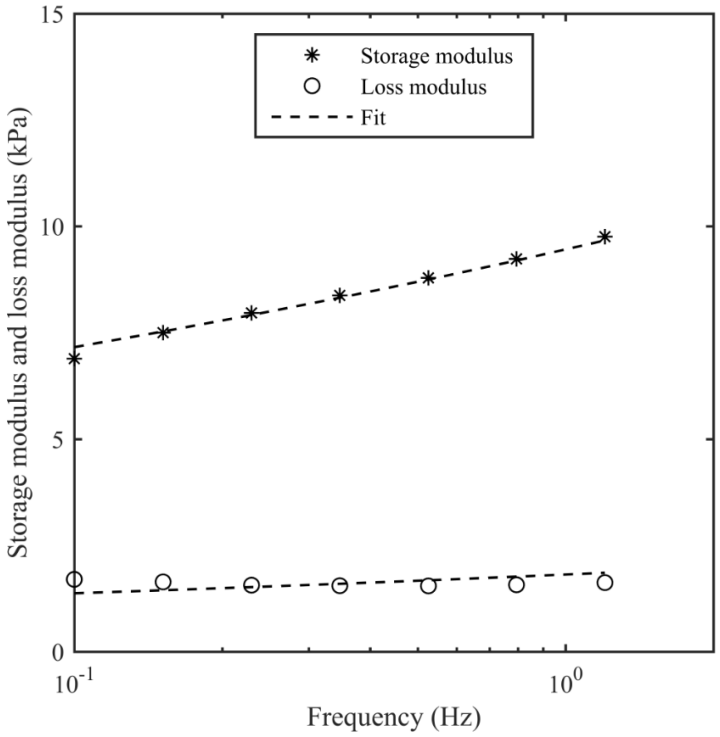
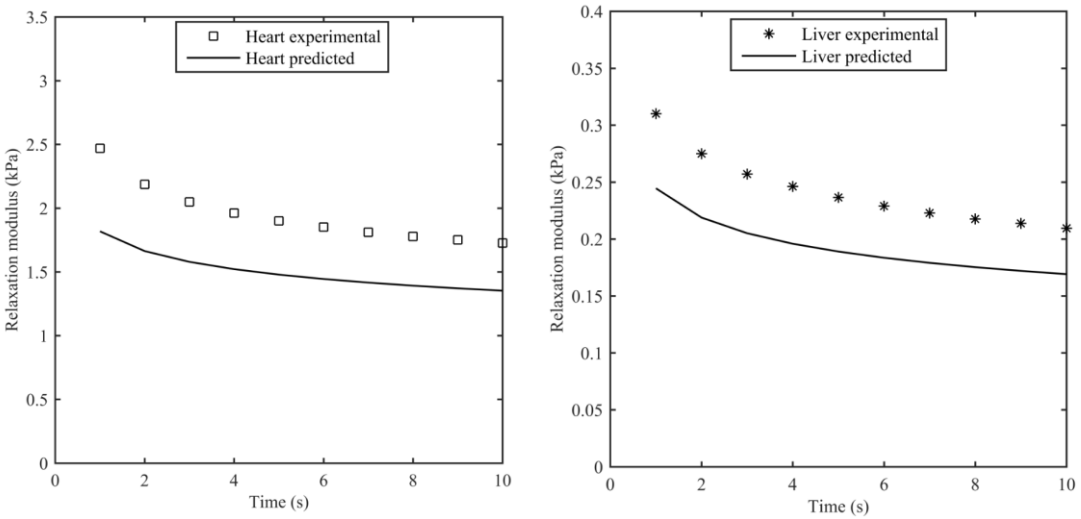


Figure 3.7**.** Storage modulus and loss modulus of porcine aorta as a function of frequency at a contact force of 0.1 N.

3.3.3. Stress relaxation

The performance of S-FKV model (obtained from fitting of frequency data) was tested by doing a time domain experiment where each tissue type was subject to a step change in strain of 0.1%. The samples had been preloaded axially to 0.5% and the shear stress was measured up to 10 seconds. The measured stress was compared to predictions based on the S-FKV model using parameters in Table 3.3. Figure 3.8 shows the experimental and predicted stress relaxation for the different porcine organs. The predictions captured the general behaviour of the time response well, despite the limited bandwidth over which the frequency data was acquired. On an average, the predicted values were 23% less for heart, 21% less for liver and 9% greater for brain.

a) b)



c)

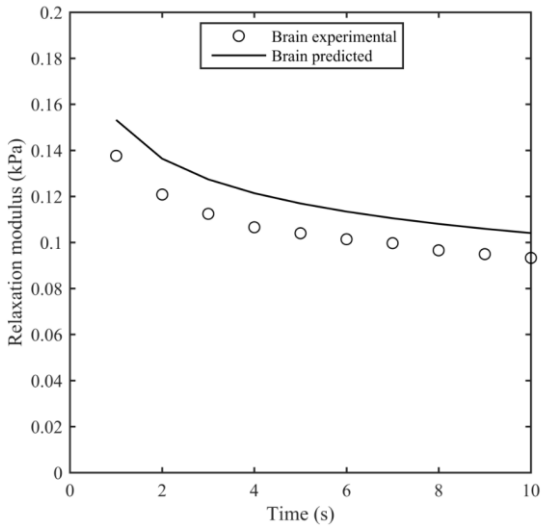


Figure 3.8. Measured stress relaxation modulus and predicted stress relaxation modulus using S-FKV model for a)Heart b)Liver c)Brain.

3.4. DISCUSSION AND CONCLUSION

This chapter reports detailed measurements of the mechanical properties of porcine heart, liver and brain as well as measurements on porcine aorta. Storage modulus and loss modulus remained steady during strain sweep tests from 0.01% to 0.1% shear strain suggesting that all tissues exhibit linear viscoelastic behaviour in this region. Frequency sweep tests were performed at 0.1% shear strain, and a S-FKV model fitted to the frequency sweep data at different axial strains for all the porcine organs while a springpot model fitted the porcine aorta data with a correlation coefficient better than 0.99. The coefficient of consistence (K_α) increased monotonically with the axial strain for porcine heart, liver and brain. This solid-like behaviour is potentially due to the close contact between connective tissue layers during the pre-compression forcing the interstitial fluid out of the tissue matrix. The predictive power of the S-FKV model was tested for porcine organs by comparing the predicted response to a step shear strain with the measured response. The stress relaxation amplitudes of the predictions and measurements were within 26%.

Table 3.6 compares the storage modulus values reported in literature with the values predicted by the S-FKV model or springpot described in this chapter. For each literature study, the S-FKV model or springpot was used to calculate values at the same frequency, in some cases this meant extrapolation from <10 Hz and comparing with measurements up to 1000 Hz. Table 3.6 shows that a discrepancy up to a factor of 5 is observed in animal tissues. This discrepancy increases to 27 in human organs, see Table 3.7. Also, there is a huge variability in the data reported in literature.

Technique	Tissue	Study	Frequency (Hz)	Average Shear Modulus (kPa)	Storage modulus from S-FKV model or springpot (kPa)
Magnetic Resonance Elastography	Porcine Aorta	Dong et. al. [73]	70	4.25	15.77
Vascular Dynamic Micro-Elastography		Schmitt et. al. [74]	240 to 480	11.25	18.28 to 19.86
Magnetic Resonance Elastography		Dong et. al. [61]	70	3.06	15.77
Magnetic Resonance Elastography	Porcine Heart	Kolipaka et. al. [75]	80	7.69	3.46
Magnetic Resonance Elastography		Nenadic et. al. [76]	40 to 500	12.70	3.16 to 4.39
Shear Wave Elastography	Porcine Liver	Chintada et. al. [62]	100 to 200	1.39	0.55 to 0.61
Magnetic Resonance Elastography		Kruse et. al. [54]	75 to 300	2.73	0.52 to 0.65
Rotational Rheometer		Nicolle et. al. [53]	0.1	0.80	0.18
Rheological Tests		Wex et. al. [77]	0.1 to 10	0.78	0.18 to 0.38
Rheometry (Time-temperature superposition)	Porcine Brain	Shen et. al. [78]	589	1.50	0.67
Oscillatory Shear Testing		Thibault et. al. [79]	20 to 200	1.01	0.39 to 0.57
Oscillatory Shear Testing (Time Temperature Superposition)		Wismans et. al. [80]	260 to 1000	1.63	0.59 to 0.73
Rotational Rheometry		Hrapko et. al. [81]	1 to 10	0.55	0.24 to 0.35
Rotational Shear Testing		Hrapko et. al. [82]	0.04 to 16	0.52	0.14 to 0.38
Shear Testing (custom-made)		Arbogast et. al. [83]	20 to 200	1.50	0.39 to 0.57

Table 3.6. Shear Modulus reported in literature for porcine tissues compared to the S-FKV model or springpot prediction.

Technique	Organ	Study	Frequency (Hz)	Average Shear Modulus (kPa)	Storage modulus from S-FKV model (kPa)
Dynamic Mechanical Testing	Human Liver	DeWall et. al. [84]	1 to 30	3.00	0.26 to 0.45
Magnetic Resonance Elastography	Human Brain	Sack et. al. [63]	25 to 62.5	1.56	0.41 to 0.47
Dynamic Shear Testing		Fallenstein et. al. [85]	9 to 10	0.85	0.34 to 0.35
Dynamic Torsion Testing		Shuck and Advani [86]	2 to 10	7.17	0.27 to 0.35

Table 3.7. Shear Modulus reported in literature for human organs compared to the S-FKV model prediction.

In conclusion, the rheological behaviour of porcine organs has been studied from 0.1 Hz up to 9.5 Hz for a range of strain amplitudes and axial compression. The behaviour of porcine organs was consistent with a S-FKV model, and aorta was consistent with springpot element. The stress relaxation behaviour of porcine organs was compared with the stress predicted by S-FKV model and the amplitudes were within 26%. The S-FKV model and springpot were extrapolated to predict the shear storage modulus at higher frequencies, and the predictions were consistent with values reported in the literature using other non-invasive methods.

CHAPTER 4: MECHANICAL TESTING OF AGAROSE AS A TISSUE MIMIC FOR PORCINE ORGANS

4.1. INTRODUCTION

Agarose is a linear polysaccharide extracted from marine red algae [87], composed of D-galactose and 3,6-anhydro-L-galactose [87,88] with a melting point of around 85℃ [88]. Agarose gel structure is a porous solid filled with liquid (i.e. biphasic structure) with both gel and fluid contributing to its viscoelastic property [87,89]. Phantoms provide desirable signal parameters during techniques such as Magnetic Resonance Elastography (MRE) [90] due to their standardised mechanical properties. Quantifying the dynamic mechanical properties of agarose gel enables the validation of measurements in elastography. The concentration of agarose phantoms can be varied to tailor their mechanical properties.

In this chapter, mechanical testing of agarose is performed at macro and micro-length scales. Elastic and viscoelastic properties were characterised using uniaxial and rheological tests for a range of agarose concentrations. Rheological tests performed across a range of agarose concentrations enabled the identification of agarose concentrations with viscoelastic properties similar to porcine heart and kidney. Oscillatory nanoindentation testing extracted the shear properties at the micro-length scale as a function of frequency. Viscoelastic properties at the micro-length scale enabled the identification of an agarose concentration with a shear modulus similar to the porcine kidney. This can potentially lead to its usage as in-vitro model during lithotripsy studies since cavitation occurring at the micro-length scale is a significant factor behind tissue damage during lithotripsy [12].

4.2. MATERIALS AND METHODS

4.2.1. Agarose preparation

Agarose (TopVision R0492, ThermoFischer Scientific), was used to prepare samples of different concentrations. Agarose samples of concentration 0.3% to 2% were prepared for uniaxial compression tests, 0.25% to 2% for rheological tests and 0.6% to 2% for oscillatory nanoindentation tests. Phantom preparation involved mixing 0.25 g to 2 g agarose powder in 100 ml of double distilled water. Since the melting point of agarose was 85℃, agarose-water mixture was heated in a microwave until it boiled. The mixture was stirred at 240 rpm using a magnetic stirrer, and degassing was performed for 10 minutes using a vacuum pump to reduce the trapped bubbles or air cavities in the mixture. The mixture was then poured into cylindrical moulds of diameter 50 mm, where it was stored at room temperature for 24 hours for gelation.

4.2.2. Uniaxial Compression

A cork borer was used to extract 25 mm diameter agarose samples of different concentrations and thicknesses, as shown in Table 4.1. A universal testing machine (Instron 5582) was used to perform the uniaxial tests using a 100 N load cell. Displacement was measured from the machine crosshead after establishing a contact force of 0.1 N with the sample. A square shaped perspex plate was attached to the machine crosshead, which compressed the sample at a cross-head velocity of 0.5 mm/min. All agarose samples were compressed until 2% strain.

Agarose concentration	Thickness [mm]
2% (n=5)	18.1±0.2
1.5% (n=5)	17.0±0.9
1.2% (n=10)	17.2 ±1.0
1% (n=5)	18.2±1.1
0.3% (n=8)	16.2±0.6

Table 4.1. Agarose concentration along with the sample thickness.

4.2.3. Oscillatory Shear

For shear strain tests, agarose samples of 2%, 1.5%, 1.2%, 0.6%, 0.4% , 0.3% and 0.25% with n=4 each were prepared and the thickness was restricted to 5 mm. A 25 mm cork border extracted samples and Table 4.2 gives the sample thicknesses for each of the three tests. The viscoelastic response in the form of storage modulus (G') and loss modulus (G'') was measured as described in section 2.3.2. To minimise the slippage at the sample-plate interface, sandpaper (200-grit size) was attached to the upper and lower plates. Phosphate Buffered Saline (PBS) solution was filled in a custom made metallic casing attached to the bottom plate of the rheometer maintained at 20°C.

Agarose concentration	Sample Thickness (Strain Sweep) [mm]	Sample Thickness (Frequency Sweep) [mm]	Sample Thickness (Relaxation Test) [mm]
0.4%	5.4±0.1 (n=4)	5.6±0.3 (n=4)	5.6±0.3 (n=4)
0.3%	5.2±0.1 (n=4)	5.7±0.1 (n=5)	5.7±0.1(n=4)
0.25%	5.4±0.1 (n=4)	5.5±0.2(n=4)	5.2±0.1(n=3)

Table 4.2. Thickness of agarose samples extracted for strain sweep, frequency sweep and relaxation tests.

Separate batches of 2%, 1.2% and 0.6% agarose with n=4 each were prepared and thickness was restricted to 5 mm for frequency sweep tests. The values of storage modulus and loss modulus obtained from these samples were compared with the values obtained from oscillatory nanoindentation tests.

4.2.4. Oscillatory Nanoindentation

Oscillatory nanoindentation tests were performed at the University of Liverpool using a Nanoindenter G200 setup, see Sec 2.3.3. The agarose samples were shipped from Oxford to Liverpool in PBS solution. These tests were performed at 10 Hz, 40 Hz, 80 Hz and 100 Hz, at an oscillation amplitude of 500 nm and pre-compression at 5 μm. Three indents were applied per sample. Figure 2.8 shows the procedure of nanoindentation tests conducted on agarose samples.

4.3. RESULTS

4.3.1. Uniaxial Compression

Figure 4.1 shows stress-strain curves for different agarose concentrations up to a strain of 2%. It can be observed that the slope of the stress-strain curve (i.e. elastic modulus) increases with the agarose concentration.

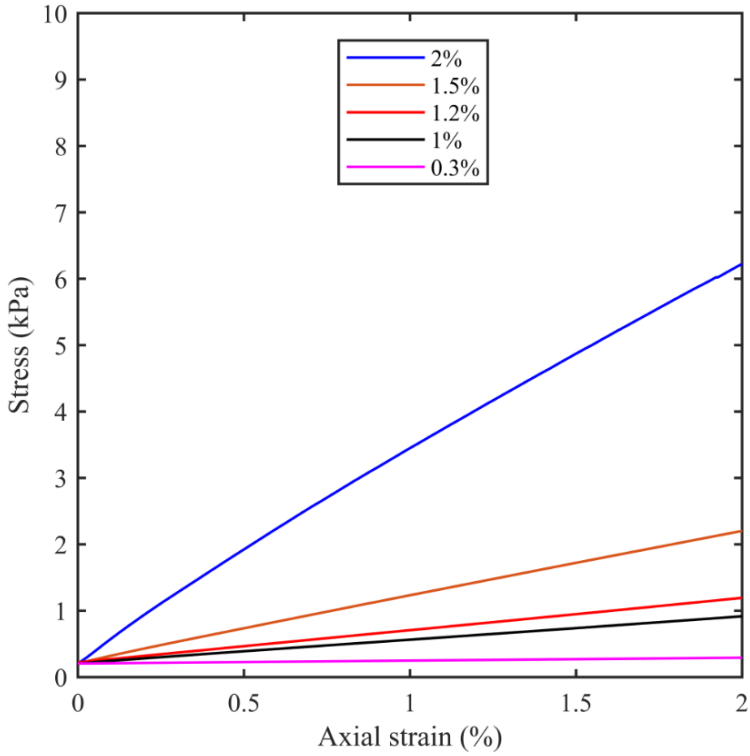


Figure 4.1. Stress-strain curve for different agarose concentrations

Figure 4.2 shows the variation of measured elastic modulus as a function of agarose concentration from our study along with the literature data from Table 4.3. Also shown is a power law fit to the measured data.

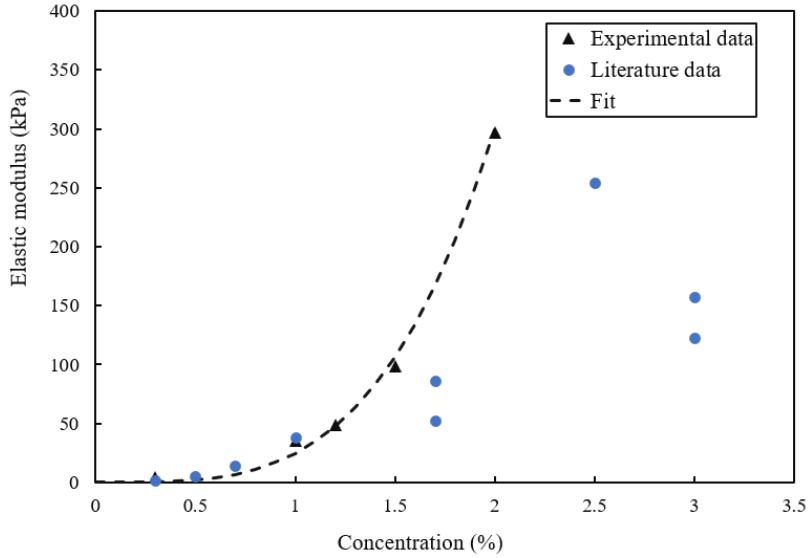


Figure 4.2. Elastic modulus as a function of agarose concentration with a power law fit ($G' = Ac^b$) such that A=24.7 kPa, b=3.6 and c is concentration in %. Literature data from Table 4.3 is also added.

A comparison of elastic modulus values from the experimental data and literature can be seen in Table 4.3. It can be observed that the elastic modulus of 1.7% agarose computed by [91,92] lies between our experimental elastic modulus values of 1.2% and 1.5% agarose and the elastic modulus of 3% agarose from [93] lies between the elastic modulus values of 1.5% and 2% agarose calculated from our experimental data. The elastic modulus of 1% agarose obtained by [88] closely resembles our experimental value of 35 kPa. The elastic modulus value of 2.5% agarose obtained by [88] is lower than our elastic modulus value of 2% agarose.

Study	**Agarose concentration**	**Elastic modulus (kPa)**
Manickam et. al. [91]	1.7%	52.0 ± 31.0
Kavitha et. al. [92]	1.7%	86.0
Brewin et. al. [93]	Fresh 3%	123.0±6.0
	Stored 3%	157.0±8.0
Normand et. al. [88]	2.5%	254.0±20.0
	1%	38.0±2.0
	0.7%	14.0±1.0
	0.5%	5.3±0.3
	0.3%	1.5±0.7
Experimental data	2%	297.0± 15.3
	1.5%	98.9± 2.3
	1.2%	48.4 ± 1.0
	1%	35.1±1.6
	0.3%	4.4±0.3

Table 4.3. Elastic modulus values for different agarose concentrations from literature and experimental data.

4.3.2. Strain sweep

The storage modulus and loss modulus were provided by the rheometer during strain sweep tests as the strain amplitude was increased from 0.01% to 10% at a frequency of 1 Hz. Figures 4.3 and 4.4 show the dependency of both moduli as a function of strain for different agarose

concentrations. The horizontal sections of both storage modulus (G') and loss modulus (G'') are consistent with the agarose samples acting as a linear viscoelastic material. Agarose of 0.25% shows linear behaviour at all the strains. The stiffness increased with the agarose concentration however the range of linear response decreased. The storage modulus of 2% agarose was only linear up to 0.1% strain, see Fig. 4.3 and the loss modulus was linear up to 0.05% strain, see Fig. 4.4.

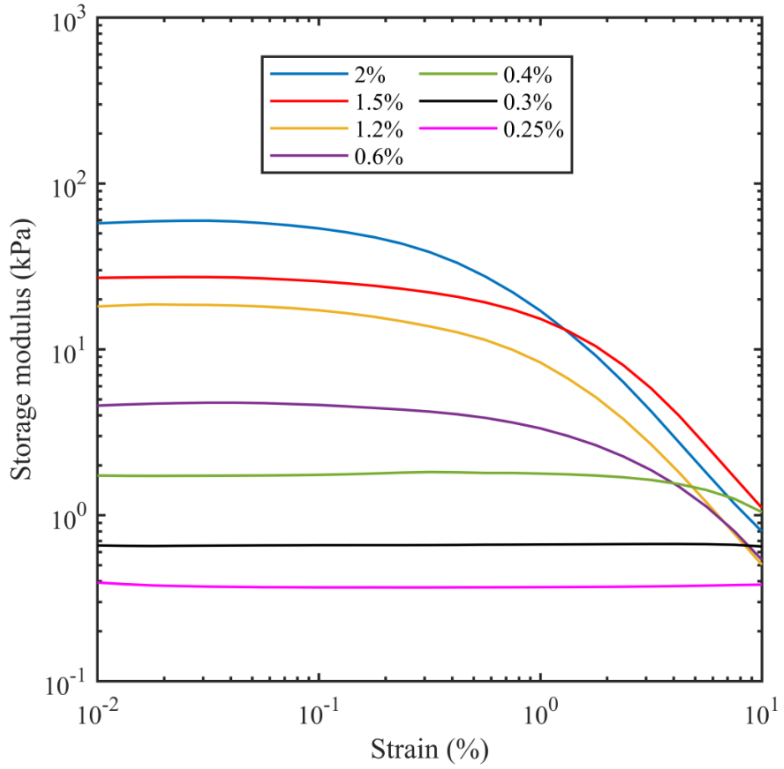


Figure 4.3. Storage modulus at 1 Hz as a function of strain for different agarose concentrations.

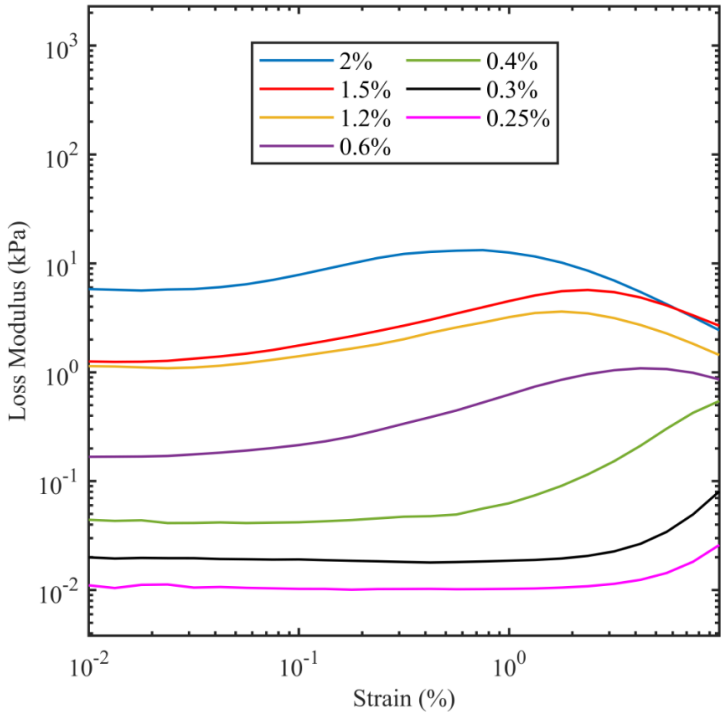


Figure 4.4. Loss modulus at 1 Hz as a function of strain for different agarose concentrations.

Figure 4.5 shows the shear storage modulus at 0.1% strain and 1 Hz as a function of agarose concentrations, along with a power law fit. The storage modulus varies from 0.4 kPa to 54 kPa as the concentration increases from 0.25% to 2%.

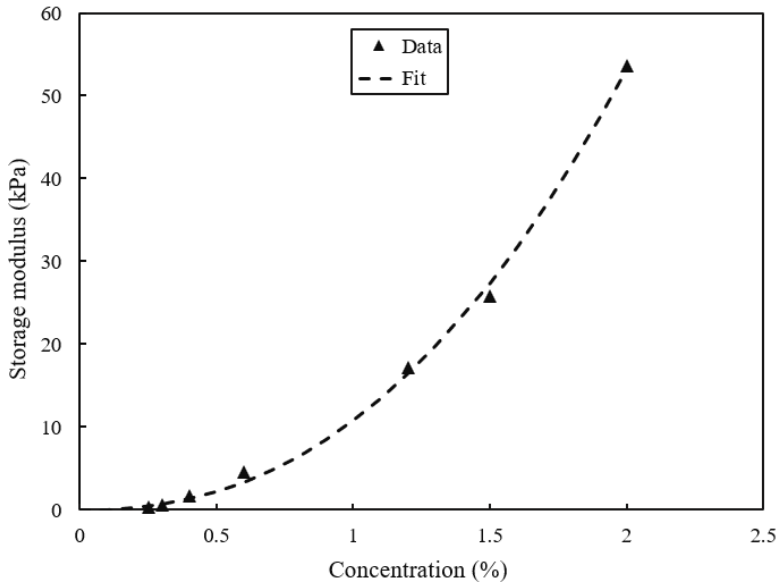


Figure 4.5. Storage modulus at 0.1% strain and 1 Hz as a function of agarose concentration with a power law fit ($G' = Ac^b$) such that A=10.8 kPa, b=2.3 and c is concentration in %.

Table 4.4 compares the storage modulus values of different agarose concentrations and porcine organs during strain sweep and frequency sweep tests. At 0.01% strain and 1 Hz, the storage modulus of the heart is 10% higher than agarose of 0.4%, the kidney is 29% lower than agarose of 0.3%, and the liver is 25% lower than agarose of 0.25%. At 0.1% strain and 0.1 Hz, the storage modulus of the heart is similar to agarose of 0.4%, the kidney is 14% lower than agarose of 0.3%, and the liver is 50% lower than agarose of 0.25%.

Sample	**Storage Modulus (kPa) from strain sweep tests (0.01% strain and 1 Hz)**	**Storage Modulus (kPa) from frequency sweep tests (0.1% strain and 0.1 Hz)**
Heart	1.90±0.50	1.40±0.50
Kidney	0.50±0.03	0.60±0.20
Liver	0.30±0.08	0.20±0.03
0.4%	1.70±0.06	1.40±0.06
0.3%	0.70±0.02	0.70±0.02
0.25%	0.40±0.03	0.40±0.03

Table 4.4. Storage modulus for different porcine organs at two different strain amplitudes and frequency along with the agarose phantoms which match closely.

4.3.3. Frequency sweep

For the frequency sweep experiments, the strain amplitude was held at 0.1%, and the frequency varied from 0.1 Hz until inertial effects were observed. Figure 4.6 shows how the measured modulus varies with frequency. The presence of inertial effects was determined by eye and was found to correspond to a storage modulus drop of 1.5% in 0.4% agarose, 2% drop in 0.3% agarose and 0.3% drop in 0.25% agarose. In porcine organs, inertial effects corresponded to a storage modulus drop of 13% in the kidney, 1.5% in the heart and 4% in the liver. The upper frequency was 9.5 Hz for porcine heart and kidney, 4.2 Hz for liver, 1.2 Hz for 0.3% and 0.4% agarose, and 0.8 Hz for 0.25% agarose. Due to the variable drop in storage modulus in different

samples, the threshold for upper frequency or inertia varied from one sample to another. Circles are used in Fig. 4.6 to identify measurements where inertial effects were deemed to have played a role.

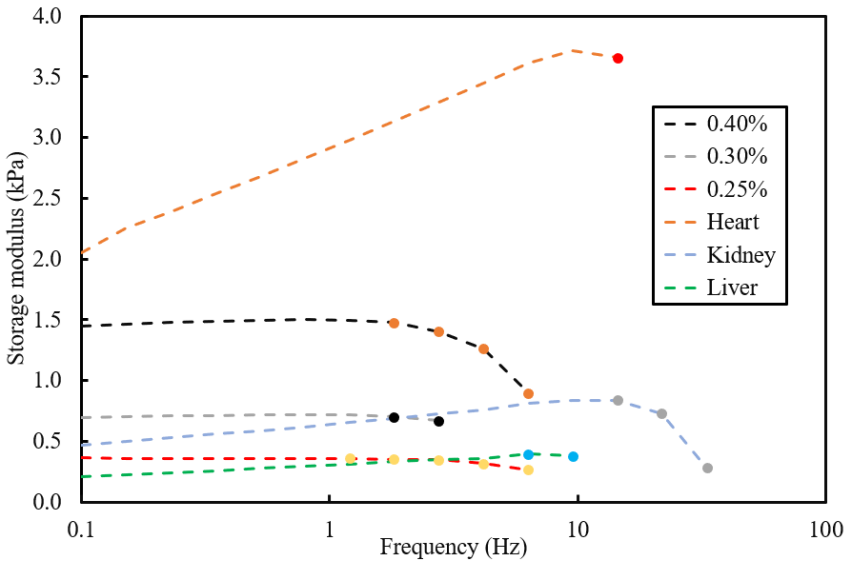


Figure 4.6. The storage modulus of porcine organs and agarose samples at a contact force of 0.1 N. A drop in storage modulus can be seen near 10 Hz in porcine organs and near 1 Hz in agarose samples which is indicative of inertia.

Figure 4.7 compares the storage modulus and loss modulus of agarose and porcine organs as a function of strain and frequency. The storage modulus and loss modulus of agarose and porcine organs remained steady from 0.01% to 0.1% shear strain, suggesting a linear viscoelastic behaviour in this region. The storage modulus increases by 6% for 0.4% agarose samples and 8% for 0.3% agarose samples from 0.1 Hz to 1.2 Hz. For 0.25% agarose samples, the storage modulus reduces by 1.5% from 0.1 Hz to 0.15 Hz followed by a 4% increase from 0.15 Hz to 0.8 Hz. There was a negligible effect of frequency on the loss modulus. Springpot was fit to the data using the least square fit function in MATLAB, in order to determine K_α and α as shown in Table 4.5. This was repeated for each axial strain. Since there was no change in the loss modulus with frequency in all three concentrations of agarose, the dashpot was removed from the S-FKV model and only a springpot was used.

Figures 4.8 a, b and c show the data and model fit of the storage modulus of 0.25%, 0.3% and 0.4% agarose samples for a range of frequencies and axial strains, and it can be seen that there is a good agreement over the range of frequencies and strains with a correlation coefficient better than 0.99. The storage modulus decreased monotonically with the axial strain (ε_A) for all agarose samples.

Sample	K_α **[kPa.(s)$^\alpha$]**	**α**
0.4%	1.500±0.060	0.019±0.002
0.3%	0.700±0.020	0.020±0.003
0.25%	0.400±0.020	0.019±0.005

Table 4.5. Springpot model parameters for different agarose concentrations at a contact force of 0.1 N.

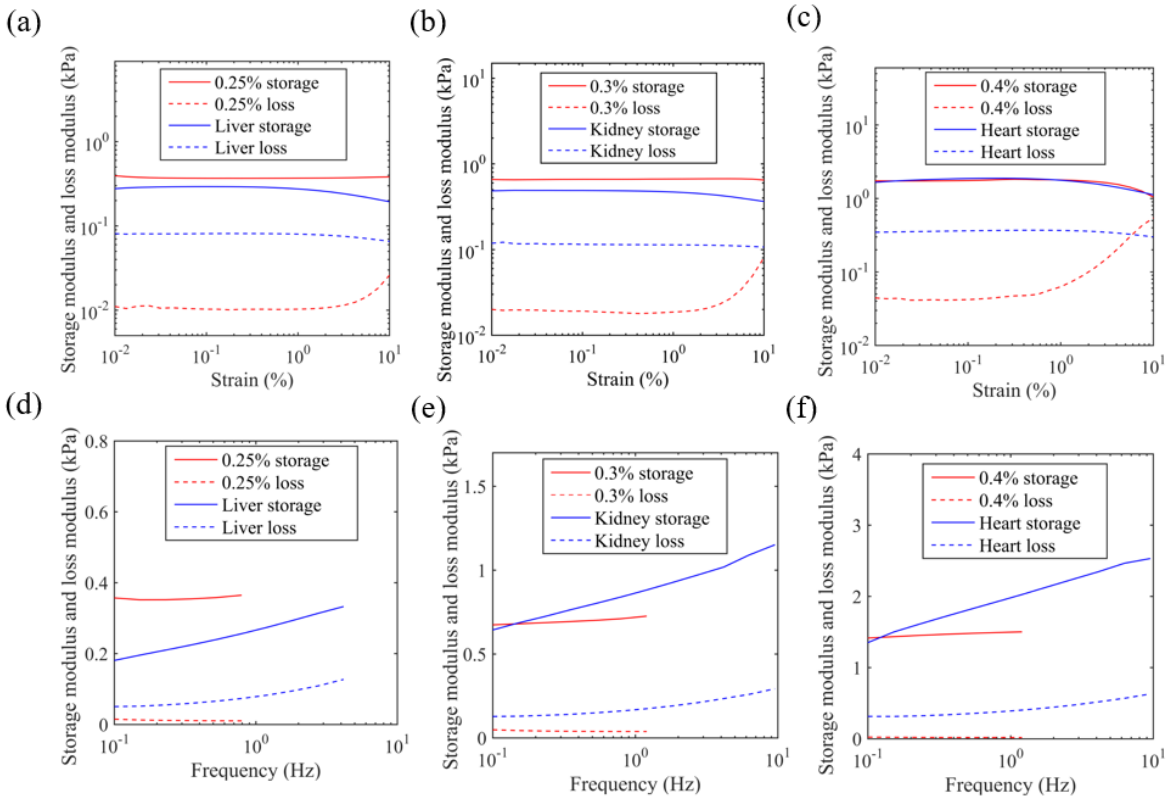
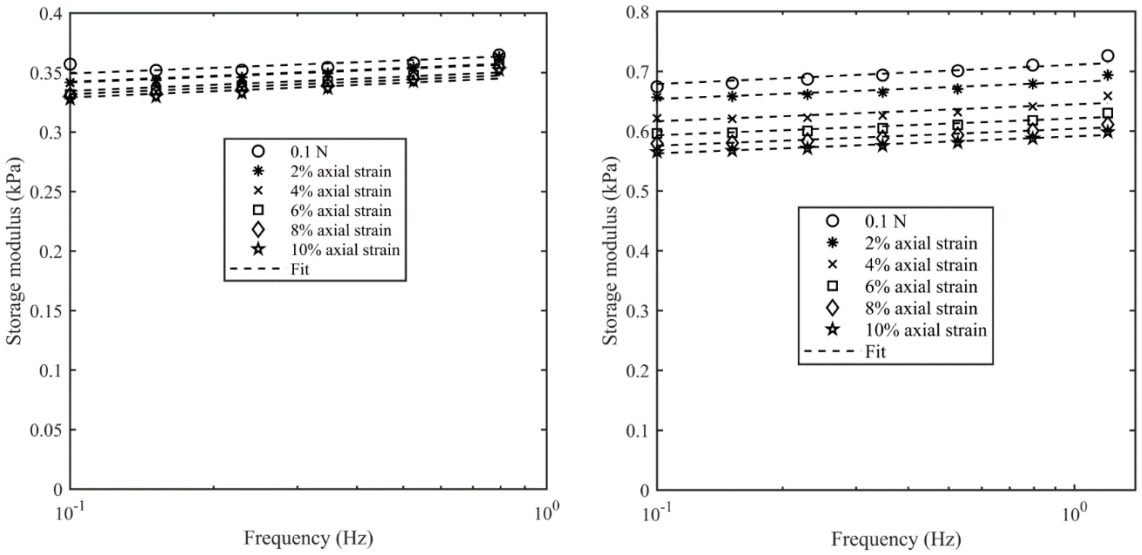


Figure 4.7. The storage modulus and loss modulus of agarose and porcine organs as a function of (a,b,c) strain and (d,e,f) frequency.

a) b)



c)

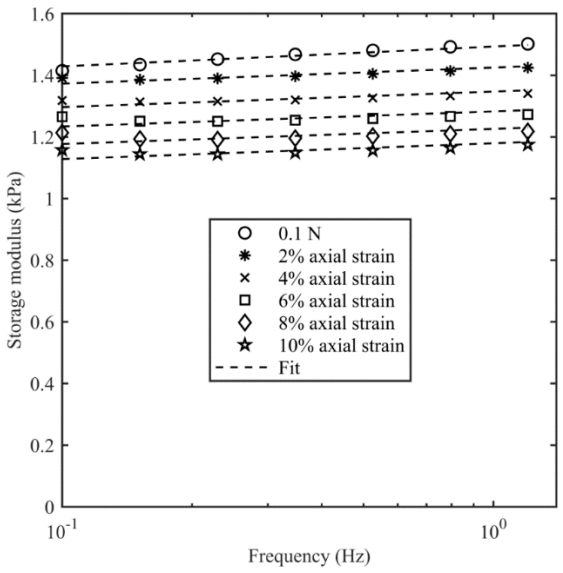


Figure 4.8. Storage modulus of a)0.25%, b)0.3% and c)0.4% agarose as a function of frequency for 6 different axial strains. The dashed line shows springpot model fit and the contact force of 0.1 N corresponds to ~0.4% axial strain.

At a contact force (F) of 0.1 N, the nominal stress is given by $\sigma = \frac{F}{A} = 204\ Pa$, where A is the cross-sectional area of the sample. Uniaxial compressive tests conducted on 1.2 % agarose yielded an elastic modulus E≈48 kPa from which the axial strain $\varepsilon_A = \frac{\sigma}{E}$ is ~0.4%. Since the axial strain measurements were relative to 0.1 N contact force, 0.4% is added to all the axial strain values.

The data for each agarose concentration and axial strain (ε_A) was fit to the springpot model, Eq. 2.21. Figure 4.9 shows the dependence of K_α as a function of ε_A for the agarose samples, and a linear relationship with the axial strain is observed.

$$K_\alpha = k_0(1 - b\varepsilon_A) \qquad (4.1)$$

where k_0 is the effective K_α as ε_A = 0. Parameters from the linear fit of Eq. 4.1 are given in Table 4.6 for all agarose samples.

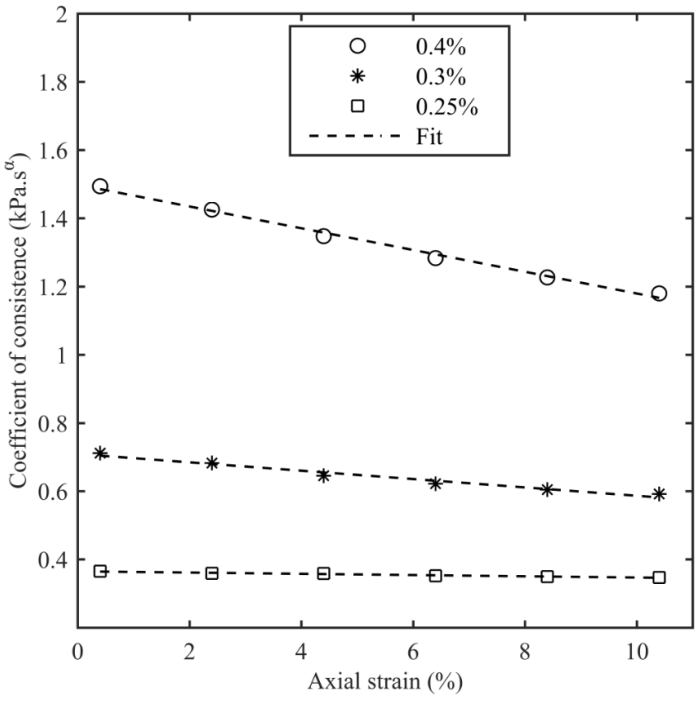


Figure 4.9. Coefficient of consistence as a function of axial strain for different agarose concentrations.

Parameters	**0.4%**	**0.3%**	**0.25%**
k_0 [kPa.(s)$^{\alpha}$]	1.500±0.060	0.700±0.020	0.400±0.010
b	0.020±0.003	0.020±0.003	0.006±0.004
α	0.019±0.002	0.020±0.003	0.019±0.005

Table 4.6. Fit parameters for K_α and the fit for α for the three agarose concentrations.

4.3.4. Stress relaxation

Samples were compressed at an axial strain of 0.4% and at time t=0, they were subjected to a step shear strain of 0.1%. For the springpot model, the response to a step strain $\in=\in_0 H(t)$, where H(t) is Heaviside function is given by :

$$G(t) = \frac{\sigma(t)}{\in_0} = k_\alpha \frac{t^{-\alpha}}{\Gamma(1-\alpha)} \qquad (4.2)$$

where Γ is the gamma function.

The measured stress was compared to predictions based on the springpot model using the parameters in Table 4.5. Figure 4.10 represents the experimental and predicted stress relaxation for different agarose samples. On average, the predicted values in agarose were 0.3% greater for 0.25% agarose, 1.4% greater for 0.3% agarose and 10% less for 0.4% agarose. In addition, the stress relaxation data for tissue samples is also given in Fig. 4.10. It can be seen that the average relaxation modulus of liver is 31% lower than 0.25% agarose samples, kidney is 48% lower than 0.3% agarose, and heart is 22% higher than 0.4% agarose.

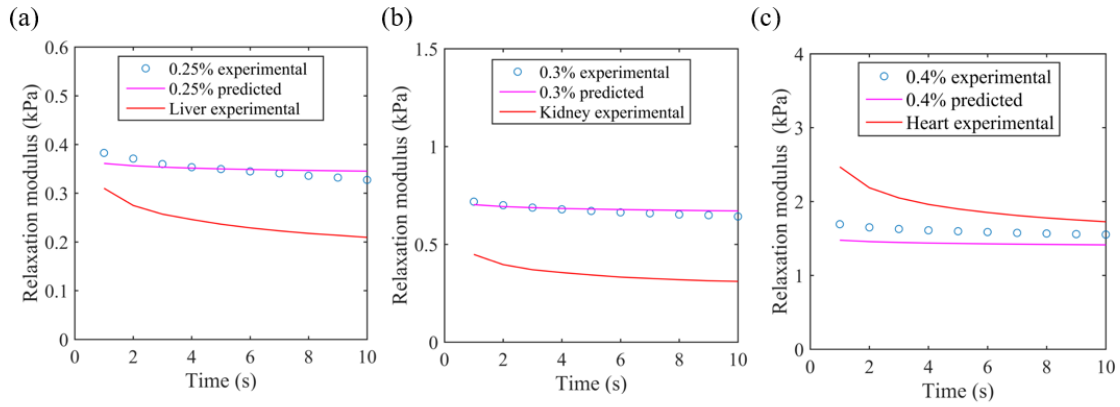


Figure 4.10. Experimental and predicted stress relaxation for different agarose concentrations and porcine organs.

Living tissue is at a temperature of 37℃, and the rheological experiments were performed at 20℃. In order to assess the effect of temperature on shear properties was assessed by increasing the Peltier plate temperature in the rheometer to 37℃. The shear modulus of 0.4%, 0.3% and 0.25% agarose samples varied less than 10% at 0.1 Hz as the temperature increased from 20℃ to 37℃, see Fig. 4.11.

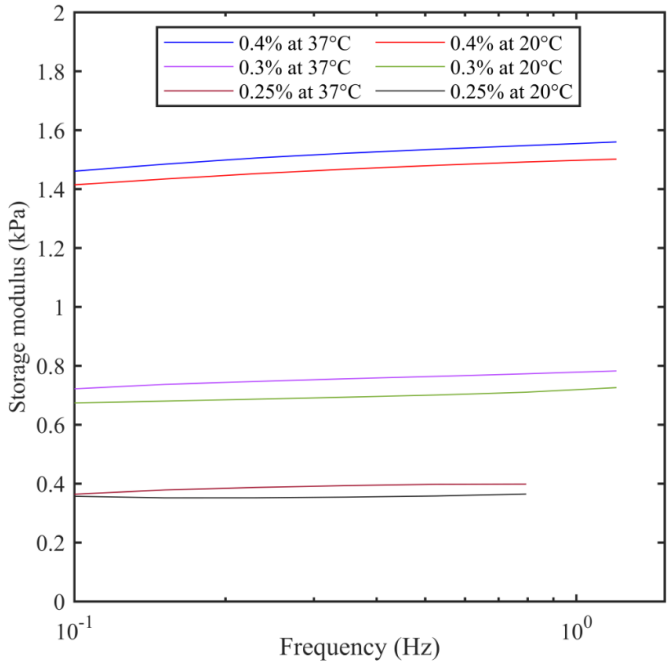


Figure 4.11. Storage modulus for different agarose concentrations at 20℃ and 37℃.

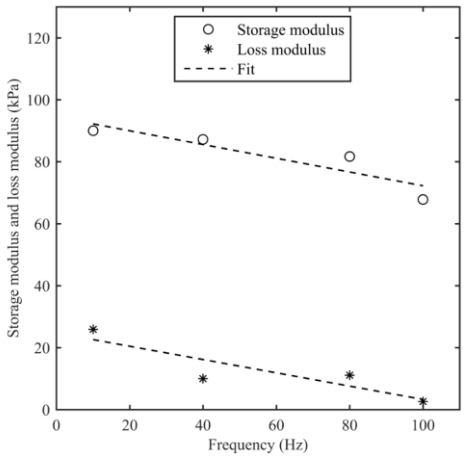
4.3.5. Nanoindentation Test

Figure 4.12 shows the storage modulus and loss modulus as a function of frequency measured by nanoindentation. In 2% agarose samples, the storage modulus monotonically decreases from 90 kPa to 68 kPa and the loss modulus monotonically decreases from 26 kPa to 3 kPa as the frequency increases from 10 Hz to 100 Hz. However, as the agarose concentration is reduced to 0.6%, the storage modulus monotonically increases from 4 kPa to 7 kPa and the loss modulus increases from 0.5 kPa to 0.8 kPa. Table 4.7 compares the storage modulus and loss modulus values of different agarose concentrations at the macro and micro-length scales. Storage modulus at micro and macro-length scale are in a similar range at 0.6% agarose and as the concentration is increased to 1.2% and 2%, there is a difference in micro and macro storage modulus by a factor of ~2. Table 4.8 shows the values of storage modulus and loss modulus for a range of agarose samples at different frequencies.

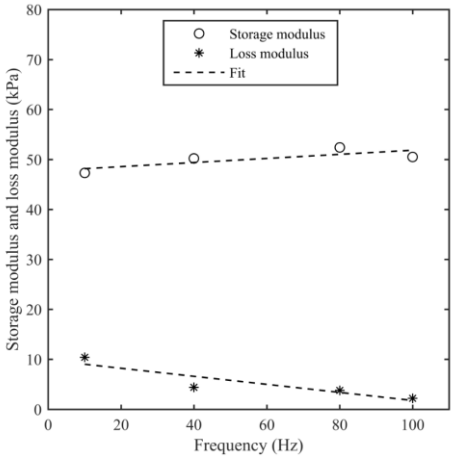
Agarose concentration (%)	**Macro-length scale**		**Micro-length scale**	
	Storage Modulus [kPa]	**Loss Modulus [kPa]**	**Storage Modulus [kPa]**	**Loss Modulus [kPa]**
0.6	3.20 ±0.10	0.10 ±0.01	4.20±1.10	0.50±0.30
1.2	19.40±0.30	1.30 ±0.30	39.30±1.60	8.90±2.60
2	47.40 ±2.20	1.90 ±0.20	90.00±15.30	25.90±3.70

Table 4.7. Values of storage modulus and loss modulus at the micro and macro-length scales. Storage modulus and loss modulus at the macro-length scale are at frequencies of 2.2 Hz, 4.2 Hz and 10.6 Hz for 0.6%, 1.2% and 2% agarose respectively. Storage modulus and loss modulus at the micro-length scale were measured at 10 Hz.

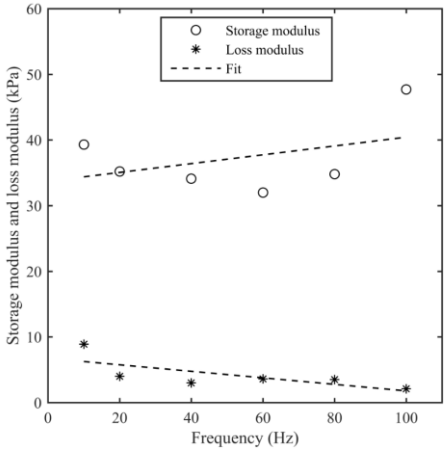
(a)



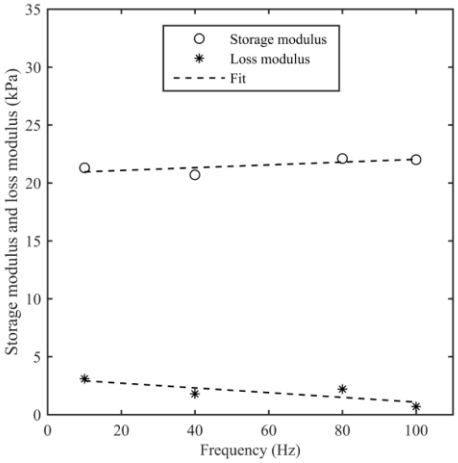
(b)



(c)



(d)



(e)

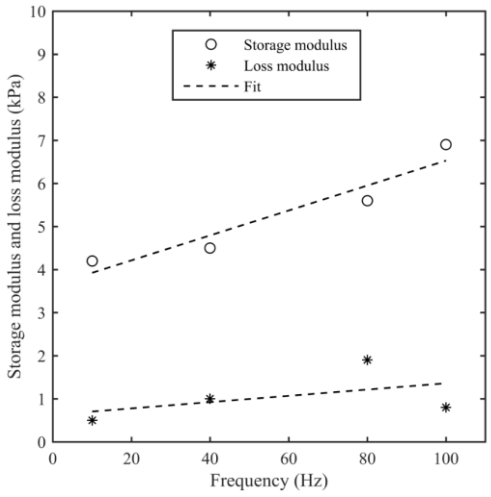


Figure 4.12. Storage modulus and loss modulus measured by nanoindentation for a)2% b)1.6% , c)1.2% , d)0.9% , and e)0.6% agarose as a function of frequency.

Frequency (Hz)	**0.6% agarose**	**0.9% agarose**	**1.2% agarose**	**1.6% agarose**	**2% agarose**
10	G' =4.2±1.1 $G^{"}$ =0.5±0.3	G' =21.3 ± 1.6 $G^{"}$ =3.1 ± 0.4	G' =39.3±1.6 $G^{"}$ =8.9±2.6	G' =47.3±10.8 $G^{"}$ =10.4±4.9	G' =90.0±15.3 $G^{"}$ =25.9±3.7
40	G' =4.5±1.4 $G^{"}$ =1.0±0.3	G' =20.7 ± 0.9 $G^{"}$ =1.8 ± 0.3	G' =34.1±3.4 $G^{"}$ =3.0±0.4	G' =50.2±12.6 $G^{"}$ =4.4±1	G' =87.2±13.3 $G^{"}$ =10.0±3.4
80	G' =5.6±1.4 $G^{"}$ =1.9±0.1	G' =22.1 ± 1.1 $G^{"}$ =2.2 ± 0.2	G' =34.8±4.1 $G^{"}$ =3.5±0.4	G' =52.4±9.7 $G^{"}$ =3.8±0.5	G' =81.7±13.6 $G^{"}$ =11.1±3.2
100	G' =6.9±0.8 $G^{"}$ =0.8±0.1	G' =22.0 ± 2.7 $G^{"}$ =0.7 ± 0.2	G' =47.7±0.9 $G^{"}$ =2.1±0.3	G' =50.5±8.5 $G^{"}$ =2.2±0.4	G' =67.8±1.7 $G^{"}$ =2.6±0.2

Table 4.8. Values of storage modulus and loss modulus in kPa for different agarose concentrations

A linear relationship of the storage and loss modulus is observed as a function of the frequency. Therefore, the storage modulus and loss modulus data, were fit to the following equations:

$$G' = G'_0(1 + b'f) \quad (4.3)$$

$$G'' = G''_0(1 + b''f) \quad (4.4)$$

where G'_0 and b' are the fitted parameters for storage modulus , G''_0 and b'' are the fitted parameters for loss modulus and f is the frequency. The fitting parameters for the different agarose phantoms are given in Table 4.9.

Parameters	**0.6% agarose**	**0.9% agarose**	**1.2% agarose**	**1.6% agarose**	**2% agarose**
G_0' (kPa)	3.6	20.8	33.7	47.7	94.4
b' (Hz^{-1})	8.0 x 10^{-3}	0.6 x 10^{-3}	2.0 x 10^{-3}	0.9 x 10^{-3}	-2.3 x 10^{-3}
G_0'' (kPa)	0.6	3.1	6.7	9.8	24.7
b'' (Hz^{-1})	11.5 x 10^{-3}	-6.5 x 10^{-3}	-7.4 x 10^{-3}	-8.2 x 10^{-3}	-8.7 x 10^{-3}

Table 4.9. Linear fit parameters in the plot of storage and loss modulus as a function of frequency.

Figures 4.13 and 4.14 represent the storage modulus and loss modulus as a function of agarose concentrations at four different frequencies. A linear relationship is observed in the plot of storage modulus and loss modulus as a function of concentration. The data was fit into linear functions of agarose concentrations:

$$G' = a_c' c - G_{0C}' \quad (4.5)$$

$$G'' = a_c'' c - G_{0C}'' \quad (4.6)$$

where c is the agarose concentration; a_c', G_{0C}' are the fit parameters for storage modulus G'; and a_c'', G_{0C}'' are the fit parameters for loss modulus G''. The parameters of the fit are given in Table 4.10.

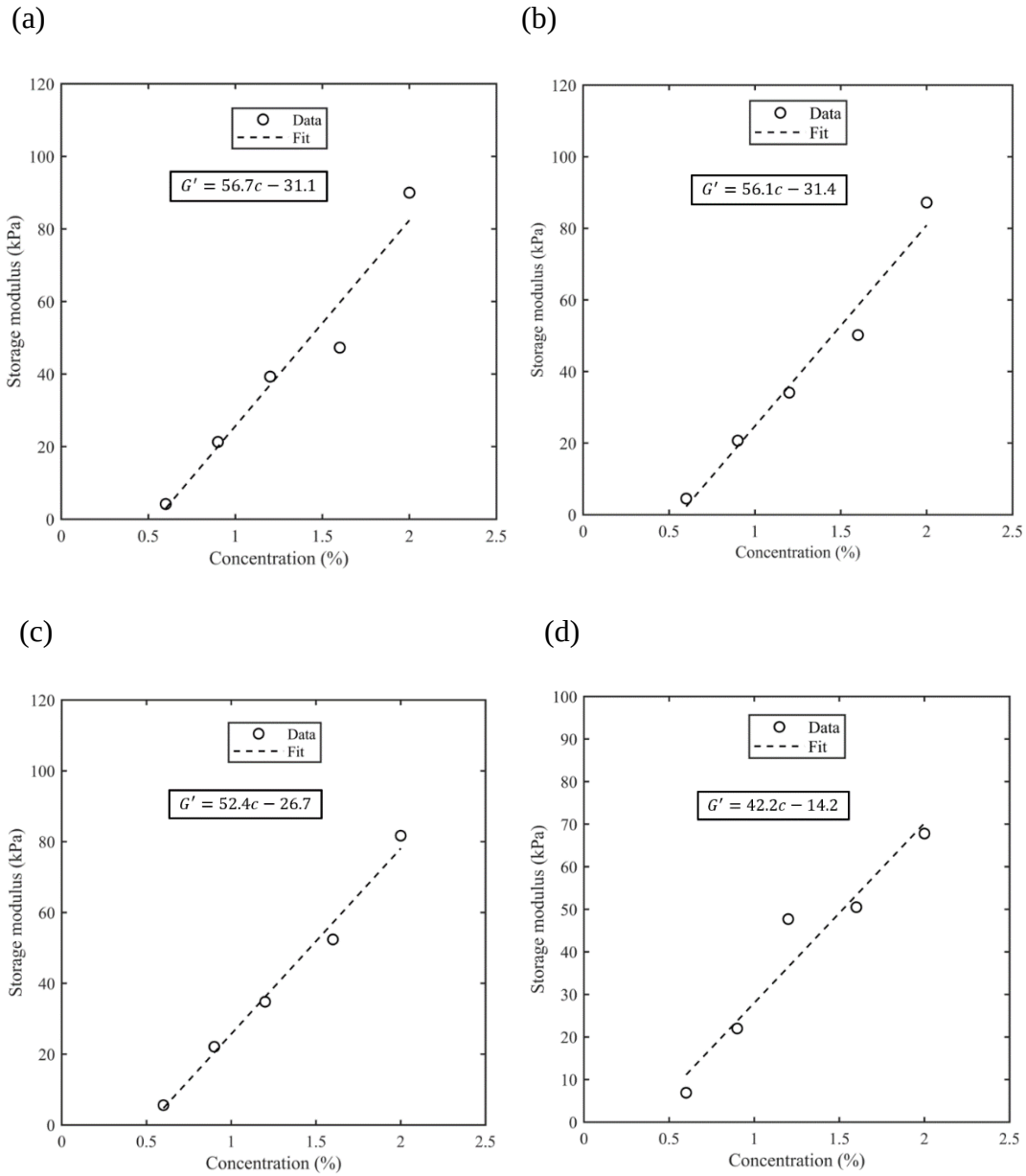


Figure 4.13. Storage modulus for a)10Hz, b)40 Hz, c)80 Hz, and d)100 Hz as a function of agarose concentrations along with the linear fit equations.

Parameters	**10 Hz**	**40 Hz**	**80 Hz**	**100 Hz**
a_c' (kPa)	56.7	56.1	52.4	42.2
G_{0C}' (kPa)	31.1	31.4	26.7	14.2
a_c'' (kPa)	16.8	6.0	5.9	1.4
G_{0C}'' (kPa)	11.4	3.5	2.9	0.1

Table 4.10. Linear fit parameters in the plot of storage modulus and loss modulus as a function of concentration.

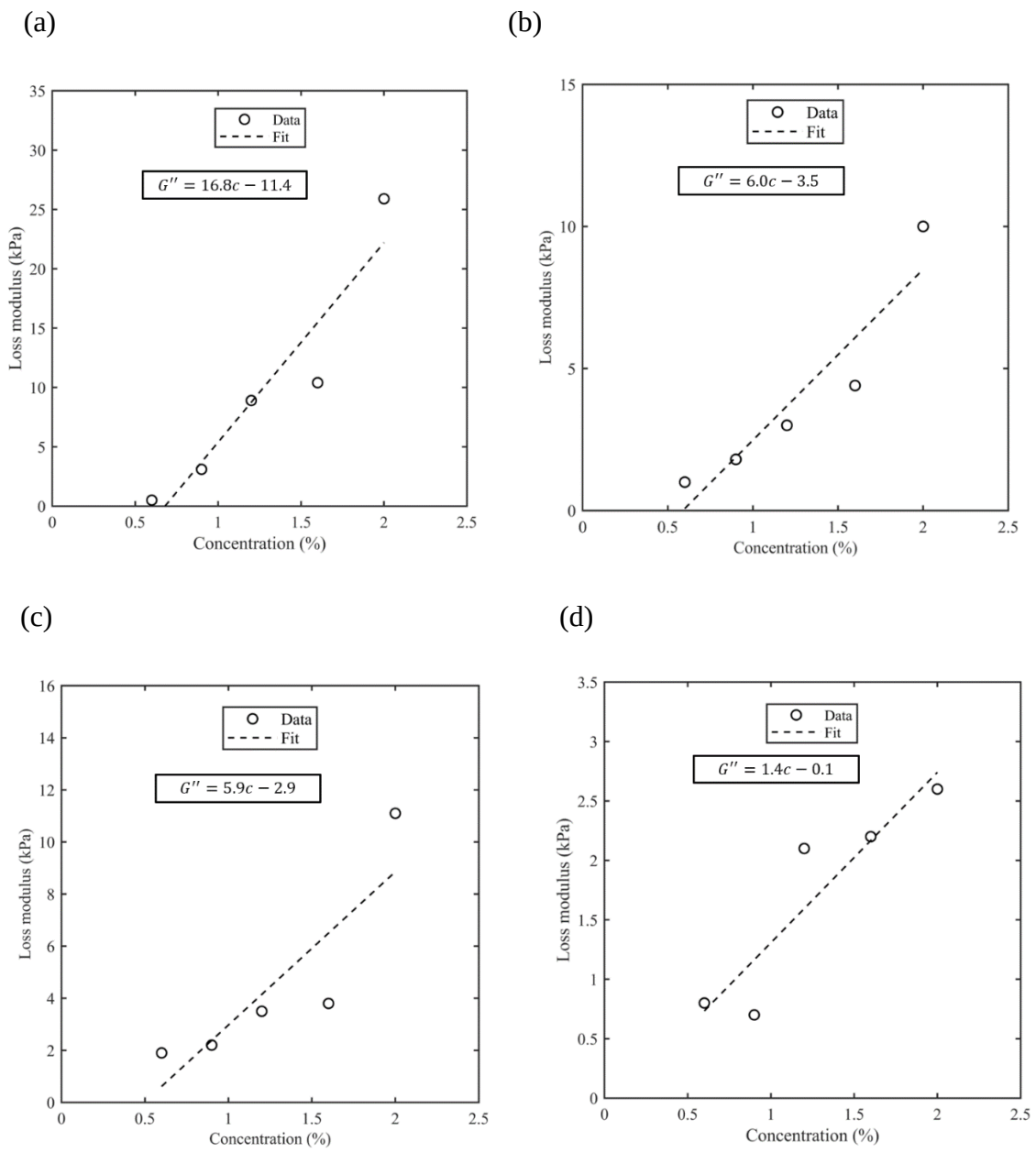


Figure 4.14. Loss modulus for a)10Hz, b)40 Hz, c)80 Hz, and d)100 Hz as a function of agarose concentrations along with the linear fit equations.

4.4. DISCUSSION

In this chapter, uniaxial compression, oscillatory shear and oscillatory nanoindentation measurements were performed on a range of agarose concentrations. The elastic modulus obtained from uniaxial tests showed a power law behaviour as agarose concentration increased from 0.3% to 2%. The elastic modulus of 1.2% agarose is ~48 kPa which is similar to that of the porcine kidney (~45 kPa, see Sec. 2.4). Agarose of 0.4% and 0.3% exhibited a shear storage modulus similar to porcine heart and kidney respectively at the macro-length scale. Tissues are robust to isotropic compression and sensitive to shear damage [12]. During the propagation of burst waves through the kidney, the shear storage modulus quantifies the stress accumulated in the kidney and is helpful in understanding the accumulation of stress after the BWL treatment, which damages the kidney. Loss modulus helps in quantifying the stress dissipated within the kidney. Hence, overall the priority in producing the agarose phantom for the kidney is shear storage modulus followed by loss modulus and compressive elastic modulus.

An agarose mimic of liver tissue was not identified as the shear storage modulus of liver at the macro-length scale was 50% lower than 0.25% agarose, the lowest possible concentration. It was not possible to further reduce agarose concentration because agarose does not gel at lower concentrations. Frequency sweep tests were performed at 0.1% shear strain, and a springpot model was fitted to the frequency sweep data at different axial strains for all the agarose samples with a correlation coefficient better than 0.99. The coefficient of consistence (K_α) decreased monotonically with the axial strain for all the agarose samples. This damping effect is potentially due to the aggregation of helical chains forming clusters during solidification at lower concentrations unlike a network spanning the entire sample at higher concentrations [94,95]. Chen et. al. [96] performed dynamic mechanical analysis on 2%, 2.5% and 3% agarose gels by testing the samples in a shear sandwich mode. Strain sweep tests were performed on 2.5% agarose gel at frequencies of 0.1 Hz, 1 Hz and 10 Hz. As the strain increased from 0.25%

to 2.5%, the shear modulus varied ~39 kPa to ~25 kPa at 1 Hz. The shear modulus values at 0.25% given in this study resembles with our storage modulus value of 43 kPa for 2% agarose. In this chapter, when samples were subject to a step change in strain, it was observed that the reduction in the relaxation modulus of agarose samples was lower than the porcine organs. This is potentially due to the weak dependency of the storage modulus on frequency in agarose samples compared to a stronger dependency in porcine organs. Also, the elasticity of connective tissues in porcine organs potentially contributes to their higher relaxation rate. The different frequency-dependent behaviour of agarose and porcine organs also potentially contributes to the difference in their relaxation modulus. The predictive power of the springpot model was tested by comparing the predicted response to a step shear strain with the measured response. The curves were qualitatively similar, and the stress relaxation amplitudes of the predictions and measurements were within 10%.

Oscillatory nanoindentation tests on 1.2% agarose resulted in a shear modulus varying from 34 kPa to 48 kPa which overlapped with that of the porcine kidney from 25 kPa to 45 kPa (see Sec. 2.6). A higher standard deviation is obtained in kidney samples compared to agarose samples, see Fig. 2.19. This is potentially due to the inhomogeneity of animal tissues compared to relatively homogenous agarose samples. Smith et. al. [97] performed indentation tests in agarose using a 4 mm diameter stainless steel flat-ended cylindrical probe. The indentation modulus varied from ~8 kPa in 0.75% w/v agarose to ~50 kPa in 2% w/v agarose during 2.5% to 7.5% strain. Nayar et. al. [98] performed dynamic nanoindentation tests on 0.5% agar concentrations using a 80 μm cylindrical flat-punch probe and obtained a storage modulus of 10.9±3.1 kPa at 90 Hz. These values lie in our experimental data range where the storage modulus varies from 4 kPa to 90 kPa at 10 Hz and 7 kPa to 68 kPa at 100 Hz as the concentration is increased from 0.6% to 2%.

4.5. CONCLUSION

The elastic and viscoelastic properties of agarose were investigated across a range of concentrations at both macro and micro-length scales. The properties of the agarose gels were fit with models to describe their dependence on concentration, strain and frequency. Agarose concentrations were found to match rheological properties of heart and kidney tissue. Liver tissue appeared to be softer than the lowest concentration at which agarose would gel. From nanoindentation tests, it was observed that the agarose concentration which matched with kidney tissue was higher than the concentration matched at macro-length scale using rheological tests. This indicates that one agarose concentration cannot match all the range of tissue properties.

CHAPTER 5 : PASSIVE ACOUSTIC MAPPING IN MONITORING BURST WAVE LITHOTRIPSY

5.1. INTRODUCTION

Cavitation has been known to play a significant role in tissue damage during SWL and BWL, see Sec. 1.2.1 and 1.4. Cavitation leads to tissue damage as the bubble collapses near the vessel wall and ruptures capillaries [99-102]. Passive Acoustic Mapping (PAM) is an ultrasound-based technique used for real-time mapping of acoustic emissions induced by a source for example scattering by a cavitation bubble. This technique has previously been used in HIFU [40] for monitoring cavitation using an array of passive detectors (i.e. ultrasound probes) which passively listen to the acoustic emissions [43]. Applications of PAM also include ablation monitoring [41] and drug delivery [103,104]. PAM can be used to differentiate between useful cavitation around the stone and harmful cavitation on the tissue. PAM has the potential to be used clinically alongside lithotripters in monitoring cavitation and minimising tissue damage.

5.2. METHODOLOGY

Figure 5.1 shows the typical configuration for PAM where a transducer with N array elements records the acoustic signals generated from cavitation bubbles in an area of interest. Inside the region of interest a mapping location x is defined and the distance to the sensor element j is given by :

$$d_j(x) = \sqrt{(x - x_j)^2 + (y - y_j)^2 + (z - z_j)^2} \qquad (5.1)$$

where x_j is the location of the j^{th} element.

The source strength at x is estimated by delay and sum beamforming of all the measured signals $s_j(t)$, and accounting for the spherical spreading one gets :

$$q\,(x,t) = \frac{4\pi}{\alpha} \sum_{j=1}^{N} w_j d_j(x) s_j(t + \tau_j(x)) \qquad (5.2)$$

Where α is the piezoelectric coefficient with units of V/Pa. In this work, the arrays were not calibrated and α was assumed to be 1, $\tau_j = d_j(x)/c$ is the propagation time from x to j, and w_j is the weight applied to the signal.

The source energy at x generated over a time duration T is then given by :

$$\psi\,(x) = \frac{1}{4\pi\rho_0 c} \int_{t_0}^{t_0+T} q\,(x,t)^2\, dt \qquad (5.3)$$

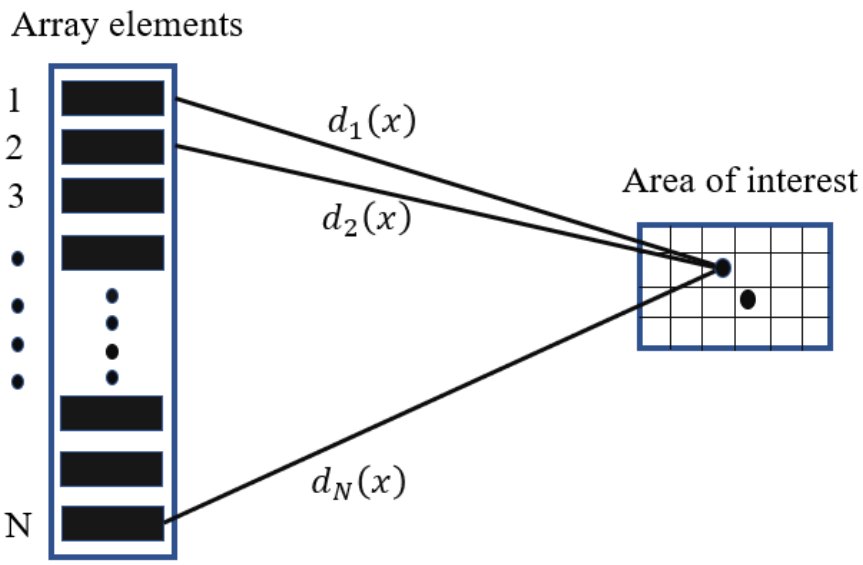


Fig. 5.1. Array geometry and area of interest

Time Exposure Acoustics (TEA) is a non-adaptive beamforming technique in which the weight vectors are assumed to be uniform across the array and fixed for all the voxels $w_j = 1/N$ However, there are inaccuracies in the locations of the receivers, variation in sensitivities of the array elements and interference between multiple sound sources which can lead to artefacts in PAM results if TEA is used [43,105]. Hence a data adaptive beamforming technique known as Robust Capon Beamformer (RCB) has been developed [106]. In this technique, weight vectors are optimised and chosen for each voxel in a data adaptive way.

For RCB it is more convenient to express ψ in terms of a correlation matrix R_s and diagonal matrix $D(x)$ consisting of the distances from grid position x to the sensor j.

$$R_s = \int_{t_0}^{t_0+T} s\,(x,t)\; s\,(x,t)^T\; dt \qquad (5.4)$$

$$D(x) = diag\,[d_1(x), \ldots., d_n(x)] \qquad (5.5)$$

$$\psi\,(x) = \frac{4\pi}{\alpha^2 \rho_0 c}\; w^T\; D(x)\; R_s(\mathrm{x})\; \mathrm{D(x)\; w} \qquad (5.6)$$

Weight vector calculation for RCB is performed by optimising the steering vector [107] , see Eq. 5.7.

$$\min_a a^T\; D(x)\; R_s(\mathrm{x})\; \mathrm{D(x)\; a} \quad \text{subject to } \|a - \bar{a}\|^2 \;\leq\; \varepsilon \qquad (5.7)$$

where a is the actual steering vector , $\bar{a}$ is the nominal steering vector and ε is the array calibration uncertainty. RCB approach was used in all the PAM analyses conducted on BWL results in this chapter.

The Spatial Integral Frame Power P_{SIF} is computed by summing the source energy ψ measured from one PAM over the region of interest and dividing by the time duration of the recording window τ_1.

$$P_{SIF} = \sum_{m=1}^{M} \frac{\psi\,(x_m)}{\tau_1} \qquad (5.8)$$

where x_m refers to a pixel in the region of interest, m is the pixel number, M is the total number of pixels.

Treatment Average Total Spatial Power P_{TATS} is computed by performing a summation of the spatial integral frame power over all the frames and dividing it by the number of frames L.

$$P_{TATS} = \frac{1}{L} \sum_{l=1}^{L} (P_{SIF})_l \qquad (5.9)$$

where $(P_{SIF})_l$ is the spatial integral frame power of the l^{th} frame.

Overall, the following steps are needed to generate a PAM frame:

i)Ultrasound probes are used to record the acoustic emissions from the area of interest.

ii)A two-dimensional grid of pixels is created in the area of interest, see Fig. 5.1.

iii)A Band-pass filter is applied to the recorded signals, 2 MHz to 5 MHz for P4-2 and 3 MHz to 9 MHz for L11-4.

iv)Beamforming is performed, and weight vectors are applied to the signals received on the array elements. This signal is back propagated, and parameters such as the Spatial Integral Frame Power and Treatment Average Total Spatial Power are computed using the equations 5.8 and 5.9.

5.2.1. Experimental setup

The BWL transducer consists of six 350 kHz elements in a ring confirmation with an aperture diameter of 85 mm, and a focal length of 100 mm [108]. The elements were driven by a programmable timing board which provided signals to six amplifiers. All channels outputted a sinusoidal profile from the matching network to the transducer element when the amplifier output was activated [109]. Figure 5.2 shows the BWL waveform measured at the focus using a hydrophone (Muller-Platte Needle Probe). Figure 5.3 shows the Pressure-Voltage data from the BWL transducer where the peak positive pressure was 0.6 MPa and peak negative pressure was 0.6 MPa at 10 V. The peak positive pressure increased to 15.7 MPa and peak negative pressure to 9.2 MPa as the voltage increased to 260 V. All the experiments in this chapter were conducted at 220 V which corresponded to a peak positive pressure of 12.4 MPa and negative pressure of 8 MPa. The number of cycles per burst was 20 during all the experiments. Figure 5.4 shows the radial and axial scans of the pressure field of the transducer. The volume treated by BWL is 60 mm * 6 mm * 6 mm.

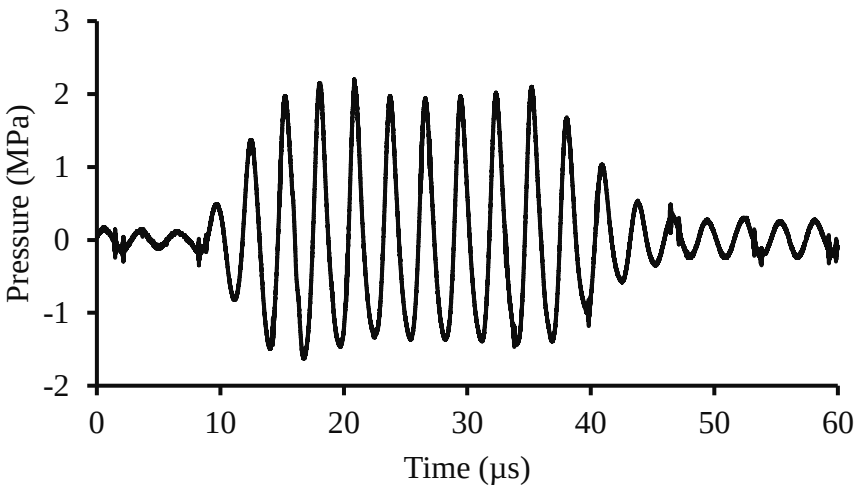


Figure 5.2. Focal waveform measured from the BWL transducer by a needle hydrophone for a 10 cycle pulse.

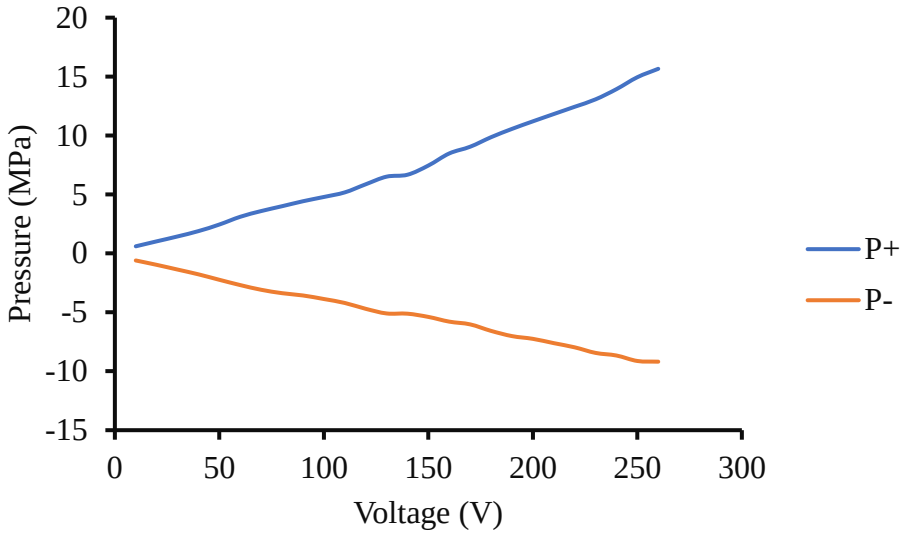


Figure 5.3. Pressure-Voltage data measured from the BWL transducer. P+ corresponds to the peak positive pressure and P- corresponds to the peak negative pressure.

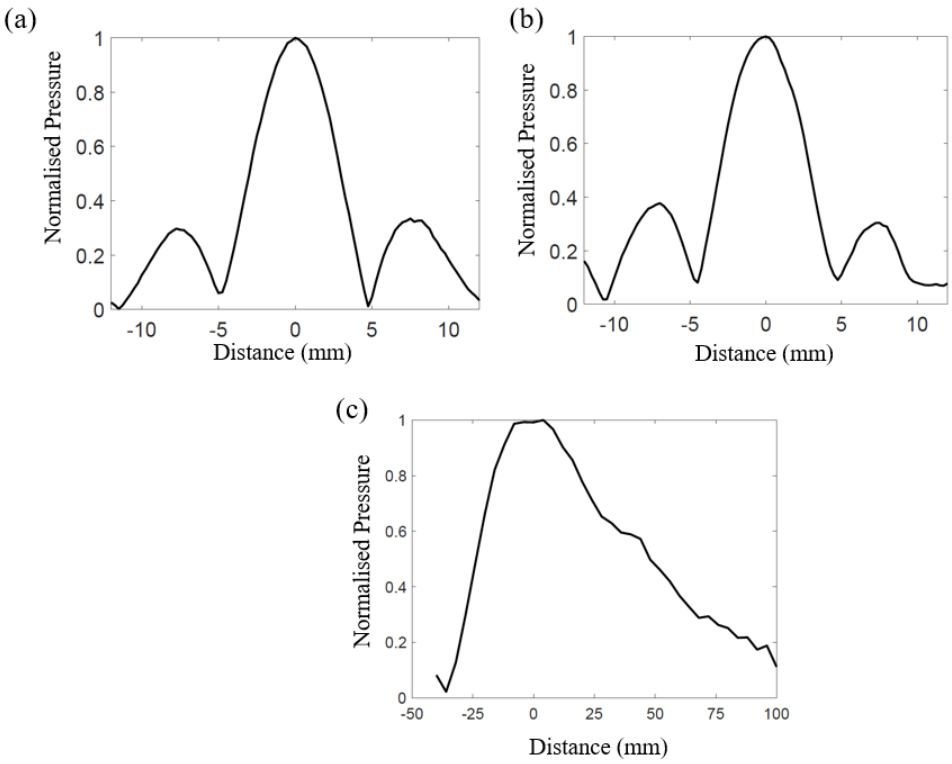


Figure 5.4. BWL waveform scans along a) X axis b) Y axis and, c) Z axis. X axis and Y axis are transverse to the acoustic axis while Z axis is along the acoustic axis. This data was provided by Adam Maxwell from University of Washington.

Figure 5.6 shows the set-up for PAM measurements with an in-line probe (P4-2) mounted into the BWL transducer and a second probe mounted on a manual positioning stage at 45 degrees to the acoustic beam. The two transducers were connected to a Verasonics ultrasound engine (Verasonics Inc, Kirkland, WA). Alignment was achieved by placing a steel ball under the B-mode imaging with the P4-2 until it was at the focus of the BWL. The L11-4 was then moved with a stage until the ball was in the centre of the image. The ball was removed, and an Ultracal-30 stones were placed at the focus. The L11-4 probe was at a distance of 55 mm to 64 mm from the focal region. The Verasonics was triggered by the BWL and acoustic emissions were recorded by both transducers for a duration of 102.4 μs for every burst at a sampling rate of 25 MHz. Agarose samples were placed on a rectangular plate, and Ultracal-30 stones were placed inside a well in the agarose with a cross section of 15 mm x 15 mm and a depth of 15 mm.

Figure 5.5a,b shows the sample waveform recorded by the L11-4 and P4-2 probes. Fast Fourier Transform spectra of the waveform is shown in Fig. 5.5c,d.

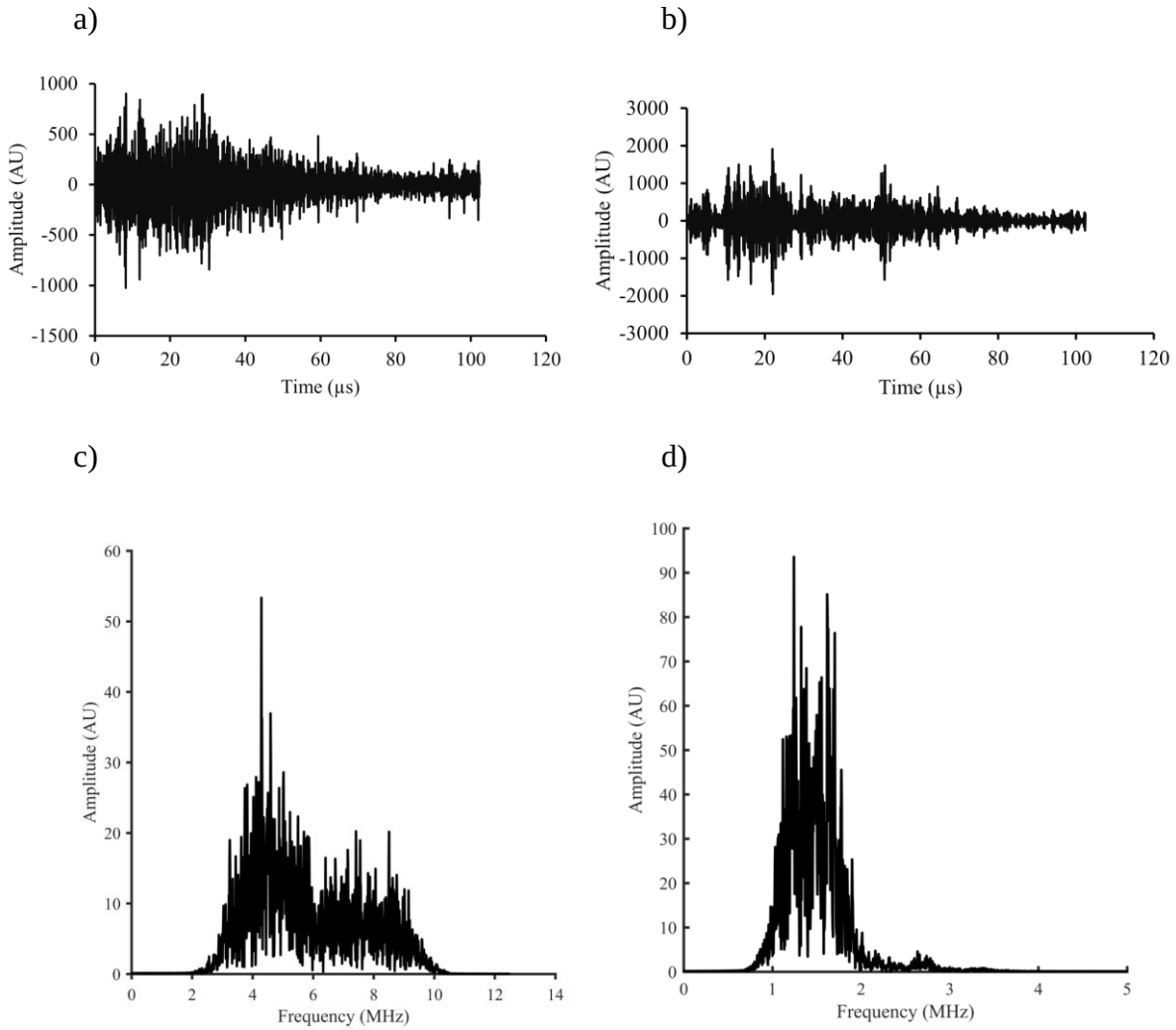


Fig 5.5. Sample waveform received a)on the 112th element of L11-4 probe b)on the 50th element of the P4-2 probe when large stone prepared in a rubber mould was subject to a 57 µs long BWL pulses. Fast Fourier Transform spectrum of (c) L11-4 and (d) P4-2 data which shows the broadband nature of the acoustic emissions from cavitation on and around the stone.

The axial and lateral resolution of the PAM transducers were estimated using the following formulae:

$$\text{Axial resolution} = 6.95 \left(\frac{z}{D}\right)^2 \lambda \qquad (5.10)$$

$$\text{Transverse resolution} = 0.89 \left(\frac{z}{D}\right) \lambda \qquad (5.11)$$

where z is the distance from the array to the mapping location, D is the aperture diameter and λ is wavelength. The aperture of L11-4 is 38.1 mm, and the centreline frequency is 6.25 MHz, corresponding to a wavelength of 0.24 mm. Hence, the transverse and axial resolution for L11-4 was 0.3 mm and 3.5 mm respectively at 55 mm from focus, and 0.4 mm and 4.7 mm respectively at 64 mm from focus. For the P4-2 probe, the nominal resolution was 2.8 mm by 117 mm at a distance of 100 mm. The diameter of Ultracal-30 stones ranged from 4 mm to 6 mm, and since the in-line P4-2 probe does not provide well-resolved spatial resolution axially, the L11-4 probe was used to capture the cavitation events occurring proximal or distal to the stone. Hence, both the transducers were not used to create a 'volumetric' PAM image. All the PAM data reported in this chapter used data from the L11-4 probe. Although the axial and transverse resolution values of the L11-4 probe changed slightly with distance between L11-4 and BWL focus, it was not considered likely to impact the results of the BWL experiments conducted in this chapter.

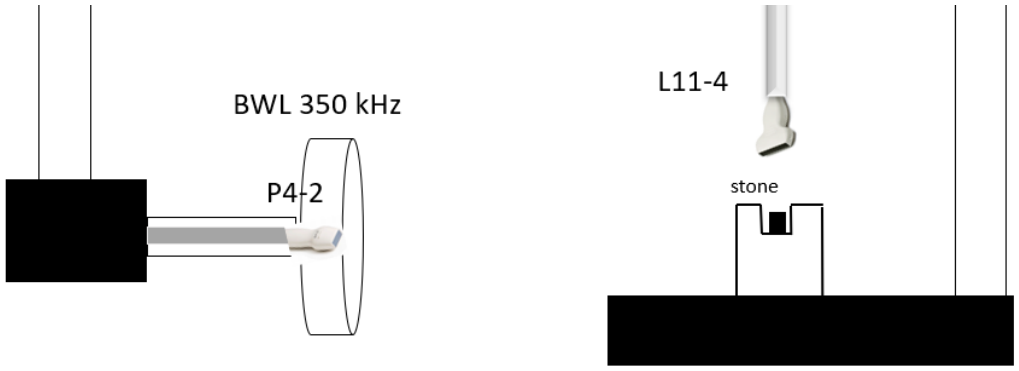


Figure 5.6. Setup for PAM measurements consisting of a BWL transducer along with in-line P4-2 ultrasound array and an out-of-line L11-4 ultrasound array. The stone was placed in agarose sample.

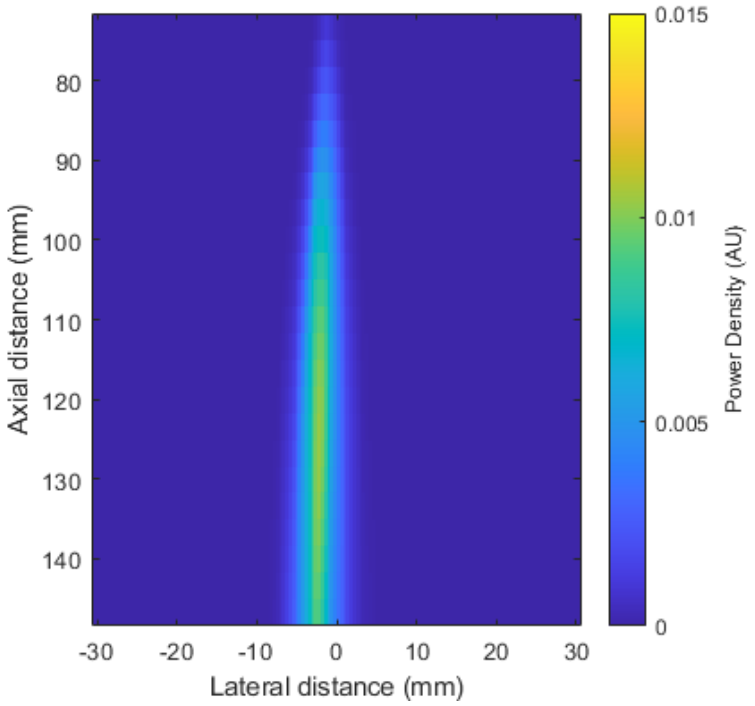


Figure 5.7. Power density map obtained after PAM processing from the P4-2 probe when a large stone prepared in rubber mould was treated with BWL.

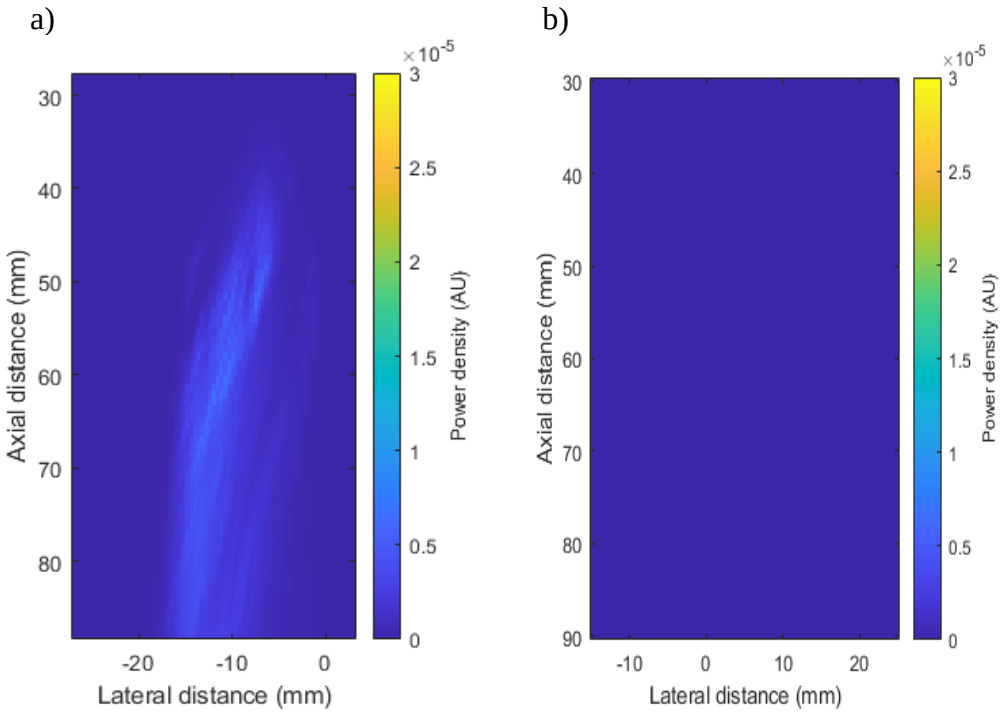


Figure 5.8. Power density map obtained after PAM processing from the L11-4 probe for a)large stone prepared in rubber mould, b)large stone prepared in Delrin mould were treated with the BWL.

Figure 5.7 shows that the cavitation power density using the P4-2 probe data from stone prepared in rubber mould is highest in the axial distance of 100 mm to 140 mm which is many times greater than the real stone dimensions around which cavitation is expected to be the highest. Figure 5.8a,b shows the power density maps using the L11-4 probe data from stones prepared with rubber and Delrin moulds treated with BWL. It can be observed that the power density varies up to 30×10^{-6} AU in stones prepared from rubber moulds and up to 8×10^{-6} AU in stones prepared from Delrin moulds. This is likely due to the higher surface roughness in stones prepared from rubber moulds, compared to a smooth surface in stones prepared from Delrin moulds, resulting in more cavitation nucleation sites. Highest power density is observed between the axial distance of 50 mm to 70 mm in Fig. 5.8 a which corresponds to the area around the stone dimensions where cavitation is expected. This confirms the superior resolution of the L11-4 probe over the P4-2 probe.

5.2.2. Preparation of agarose samples

0.3% agarose and 6% agarose samples were prepared, see Sec. 4.2.1. The agarose-water mixture was poured into rectangular moulds of dimensions 50 mm x 50 mm x 45 mm. The top plate of the mould had a protrusion of cross-section 15 mm x 15 mm and a height of 15 mm, which led to formation of a well in the agarose gel. Once poured, the moulds were stored at room temperature for 24 hours to gel. Sandpaper was placed on the agarose gel boundary during the BWL experiments so that the interface between the gel and water filled well could be identified using B mode imaging. This enabled the localisation of cavitation around the stone placed in the well from the cavitation inside the gel. Sandpaper was removed during the firing of BWL pulses. The 0.3% agarose gel was used to study the damage and cavitation effect on the stone size since its viscoelastic properties resembled with the porcine kidney (refer to

Chapter 4). A 6% agarose gel was used as a comparator as no damage was observed in this gel during the BWL experiments.

5.2.3. Preparation of Ultracal-30 stone

Ultracal 30 cement was mixed with water in a ratio of 1:1, and the mixture was stirred using a magnetic stirrer and degassed for 10 minutes using a vacuum pump. The mixture was cast in either in a mould made of rubber or a mould made of Delrin for a duration of 24 hours. The stones were soaked in water for at least 24 hours before the BWL experiments so that the presence of air pockets could be minimised. After BWL treatment, a sieve was used to retain the fragments larger than 2 mm, and these fragments were dried for 24 hours before being weighed. Fragmentation was quantified as the reduction in mass divided by the initial mass of the stone.

Rubber mould

Rubber moulds consisted of circular holes (diameter 6 mm and depth 8 mm), which were filled with Ultracal-30 mixture and extracted as stones after 24 hours. Stones prepared in rubber mould were placed inside 0.3% agarose (n=3) and 6% agarose (n=3).

Delrin mould

Delrin moulds consisted of two rectangular plates, circular holes of diameter 4,5 and 6 mm, and depths 5, 7 and 8 mm, respectively, were drilled into the upper plate. The lower plate was screwed to the upper plate, and the holes were filled with an Ultracal-30 mixture and cast as stones. After 24 hours, the lower plate was removed, and circular stones were extracted from the mould's upper plate. Five stones of small, medium and large sizes were placed in 15 different 0.3% agarose samples. Table 5.1 shows dimensions, mass and surface area for stones classified as 'Small', 'Medium' and 'Large'.

Classification	Dimensions (mm) Length*Diameter	Mass (mg)	Surface Area (mm^2)
Small stone (n=5)	5 * 4	76±2	88
Medium stone (n=5)	7 * 5	187±2	149
Large stone (n=5)	8 * 6	303±3	207

Table 5.1. Dimensions, mass and surface area of small, medium and large stones.

5.3. RESULTS

5.3.1. Stone fragmentation

Rubber mould stones placed in 0.3% agarose

Three stones made with the rubber mould were placed in 0.3% agarose holder and were subjected to PRFs of 20 Hz, 40 Hz and 80 Hz. The duration of the BWL treatment lasted ~2 hours. The Treatment Average Total Spatial Power and corresponding stone fragmentation percentage are shown in Fig 5.9. It was observed that all the stones had broken about the same but the detected cavitation ranged from 0.005 to 0.012.

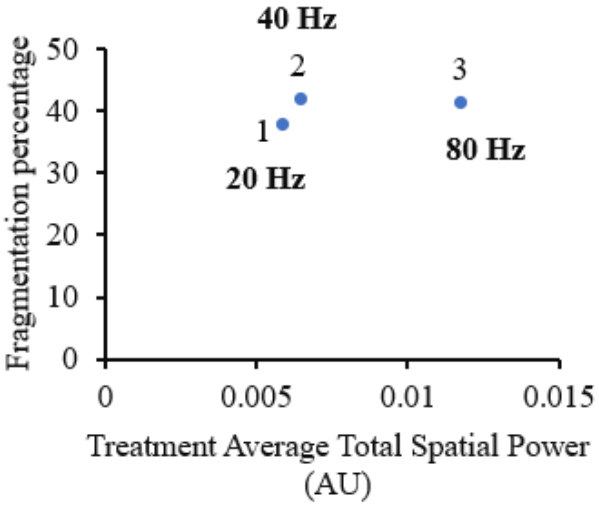


Figure 5.9. Treatment Average Total Spatial Power from the L11-4 probe and fragmentation percentage at three PRF's for large stones prepared in rubber mould and placed in 0.3% agarose.

Rubber mould stones placed in 6% agarose

Figure 5.10 shows fragmentation vs power for three stones made with the rubber mould, placed in 6% agarose and subjected to PRFs of 20 Hz, 40 Hz and 80 Hz. The total treatment duration varied from 1 to 2 hours. Despite stone 2 having a higher fragmentation percentage than stone 3, its Treatment Average Total Spatial Power is lower than stone 3 by a factor of ~2.

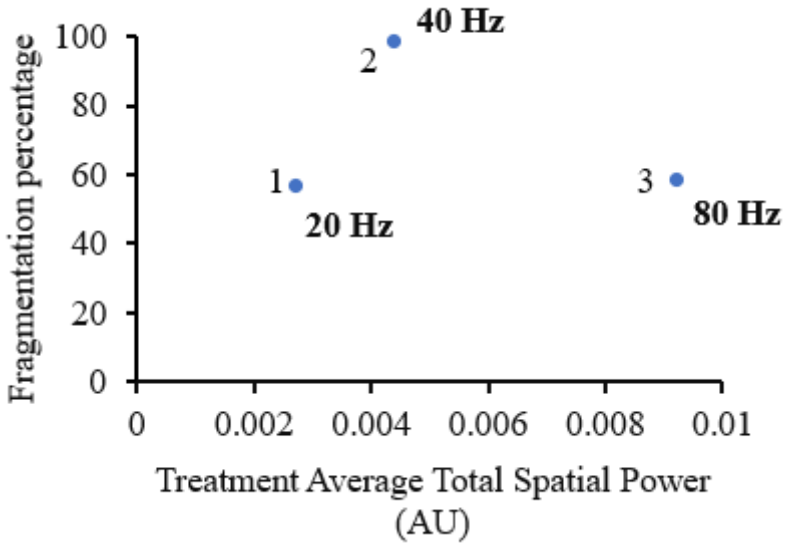


Figure 5.10. Treatment Average Total Spatial Power from the L11-4 probe and fragmentation percentage at three PRF's for large stones prepared in rubber mould and placed in 6% agarose.

Delrin mould stones placed in 0.3% agarose

BWL treatment duration was ~5 minutes to ~30 minutes in small stones, ~30 minutes in medium stones and ~30 minutes to ~50 minutes in large stones. All stones were treated at PRF of 20 Hz. Figure 5.11 shows the Treatment Average Total Spatial Power and fragmentation percentage in small, medium and large stones that were formed in the Delrin moulds. In the small stones group, an overall increase in the Treatment Average Total Spatial Power was observed with the fragmentation percentage. Fragmentation percentage was not correlated with the Treatment Average Total Spatial Power for the medium stone group. In the large stone

group, there was no trend observed in the Treatment Average Total Spatial Power with the fragmentation percentage.

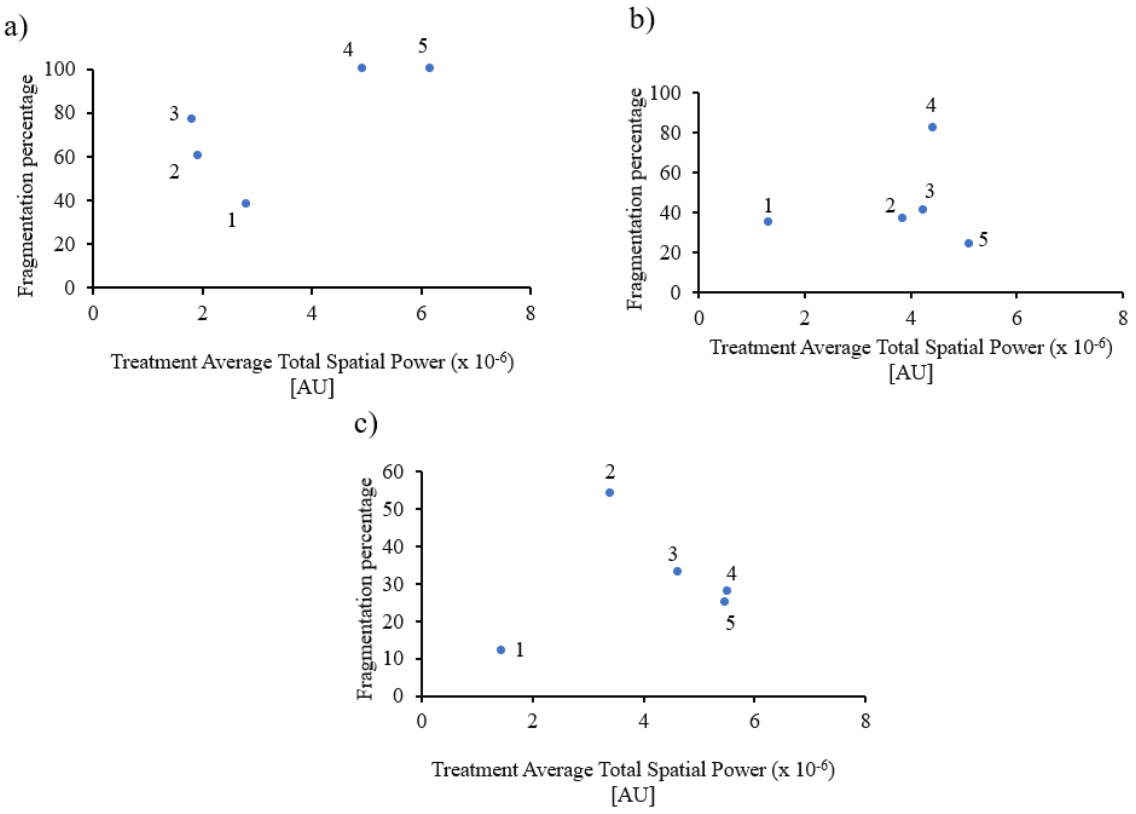


Figure 5.11. Treatment Average Total Spatial Power from the L11-4 probe and corresponding fragmentation percentage for a) Small stones, b) Medium stones, and c) Large stones prepared in the Delrin mould, placed in 0.3% agarose and subjected to PRF of 20 Hz.

Table 5.2 shows the Treatment Average Total Spatial Power computed from L11-4 for small, medium, and large stones (n=5 each). Figure 5.12 shows the mean Treatment Average Total Spatial Power over the five stones and it can be seen that there is a 21% increase in the power between the smallest and the largest stone.

Treatment Average Total Spatial Power (AU) [x 10^{-6}]					
Stone size	**Stone 1**	**Stone 2**	**Stone 3**	**Stone 4**	**Stone 5**
Small	1.82	1.92	6.18	2.82	4.93
Medium	4.42	4.25	1.32	3.86	5.12
Large	4.62	5.53	1.46	5.48	3.41

Table 5.2. Treatment Average Total Spatial Power from the L11-4 probe for small, medium and large stones prepared in the Delrin mould, placed in 0.3% agarose and subjected to PRF of 20 Hz.

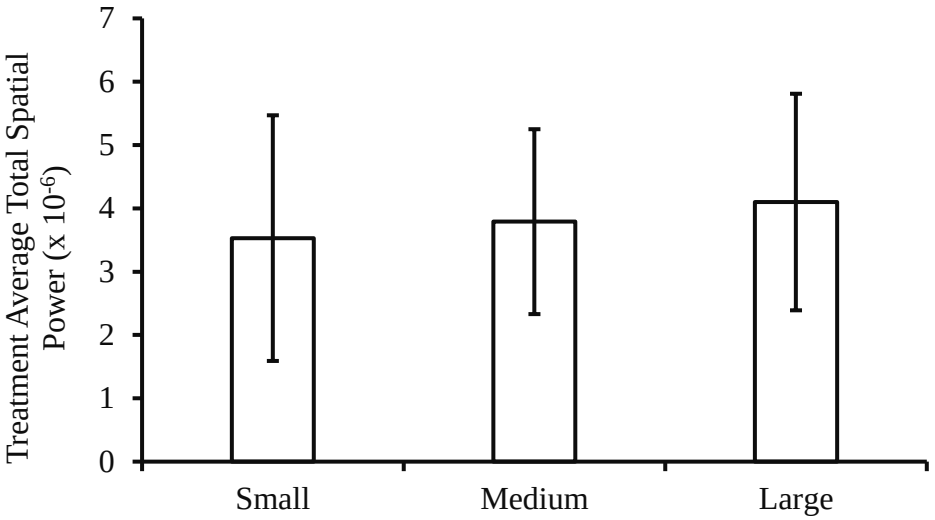


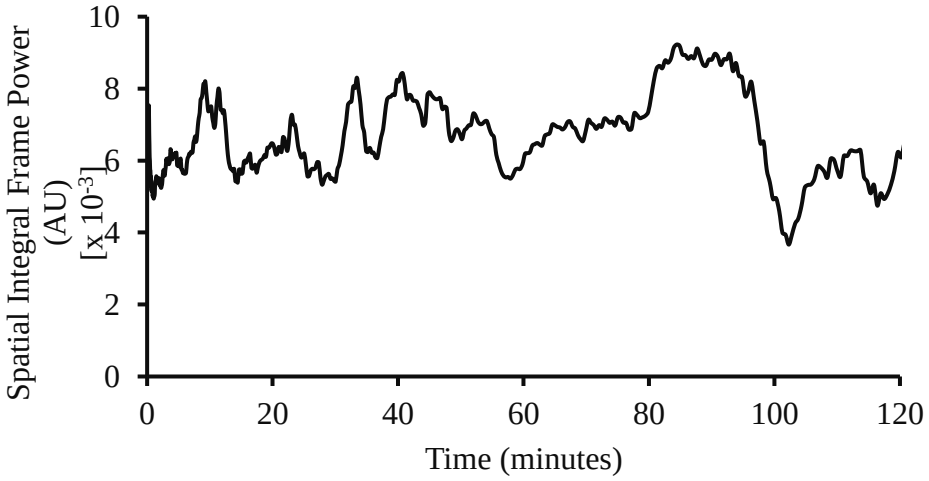
Figure 5.12. Mean and standard deviation of the Treatment Average Total Spatial Power at 20 Hz from the L11-4 probe for small, medium and large stones prepared in the Delrin mould and placed in 0.3% agarose samples.

Correlation between PAM power and stone fragmentation

The Spatial Integral Frame Power is plotted as a function of time for large stones prepared in rubber mould and placed in 0.3% agarose for 40 Hz (Fig. 5.13) and 80 Hz (Fig. 5.14). There was no detectable correlation between the PAM power and fragmentation. The roughness of the stone surface appears to be the main determinant of cavitation activity in BWL but the imaging methods used in this work were unable to quantify the difference in the surface roughness between stones made in the rubber and Delrin moulds.

Unfortunately in the analyses done here over many stones, it was not possible to find features of the cavitation power which predicted stone fragmentation.

a)



b)



c)



Figure 5.13 a) Spatial Integral Frame Power with time from the L11-4 probe for large stones prepared in a rubber mould and subjected to PRF=40 Hz, b,c) Stone fragmentation images at 18 minutes and 90 minutes.

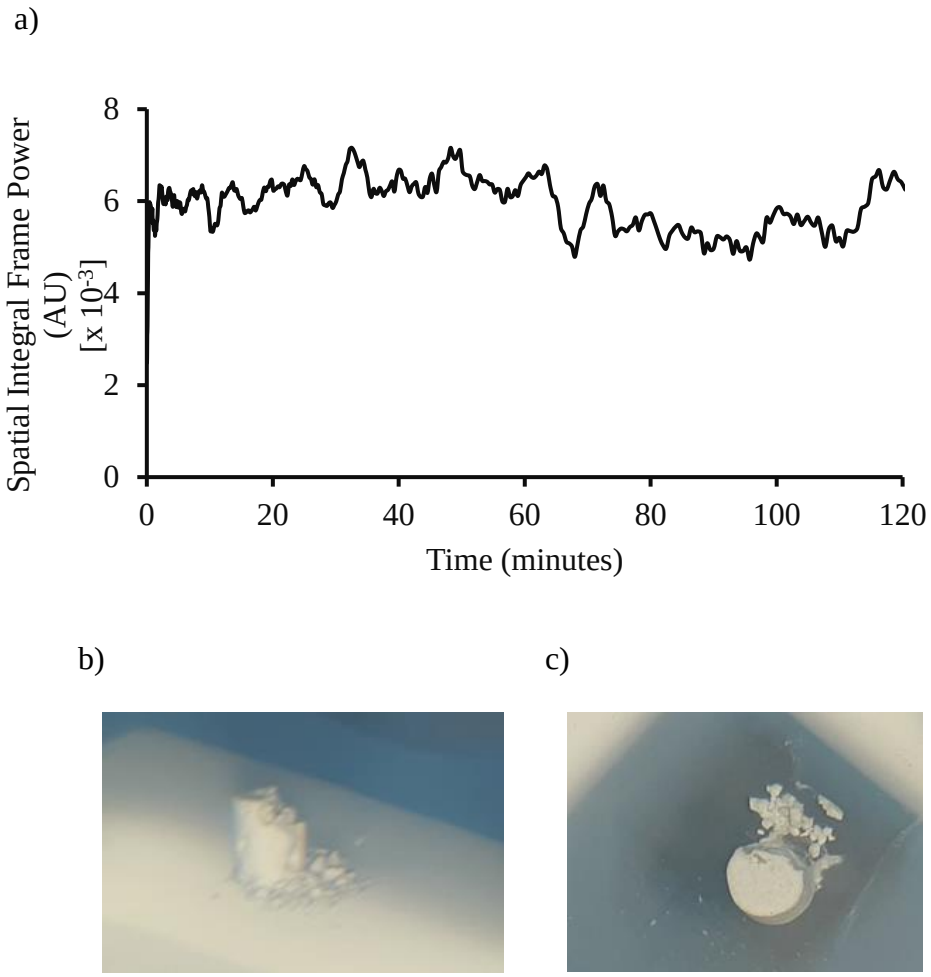


Figure 5.14 a) Spatial Integral Frame Power with time from the L11-4 probe for large stones prepared in a rubber mould and subjected to PRF=80 Hz, b,c) Stone fragmentation images at 55 minutes and 92 minutes.

5.3.2. Agarose damage

BWL has the potential to result in tissue damage and the agarose models were used to assess that. Figure 5.15 shows 0.3% agarose samples, which has mechanical properties close to kidney before and after the treatment. The volume of the damage was measured by filling the cavity with sand (50-70 mesh particle size) and then weighing the mass of the sand. Figure 5.16 shows

that the damage increased as the size for stones prepared in the Delrin mould increased from small to large. Presumably this is because the larger surface area results in more cavitation which results in more damage to the nearby agarose surface. For large stones prepared in the rubber mould, the damage was four fold greater than the large stones prepared in the Delrin mould. This is likely because the rubber mould results in greater surface roughness which results in more cavitation even though the surface area is same.

a) b)

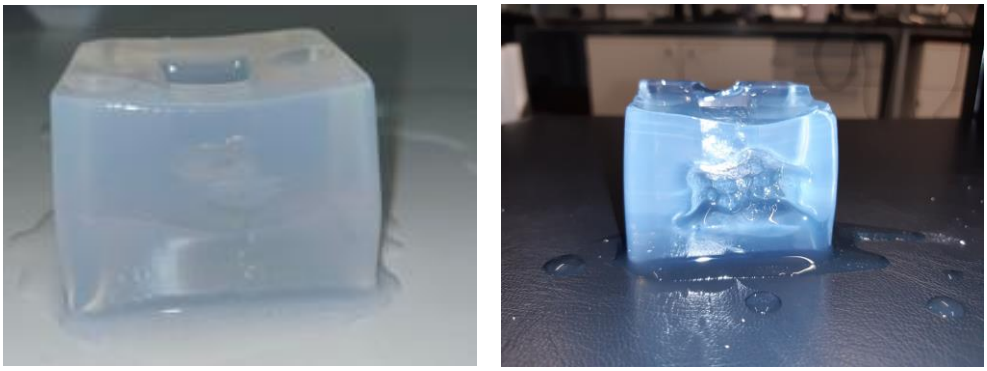


Figure 5.15. Agarose sample of 0.3% subjected to 20 Hz PRF with a large stone prepared in Delrin mould, a)Before the treatment, b)After the treatment.

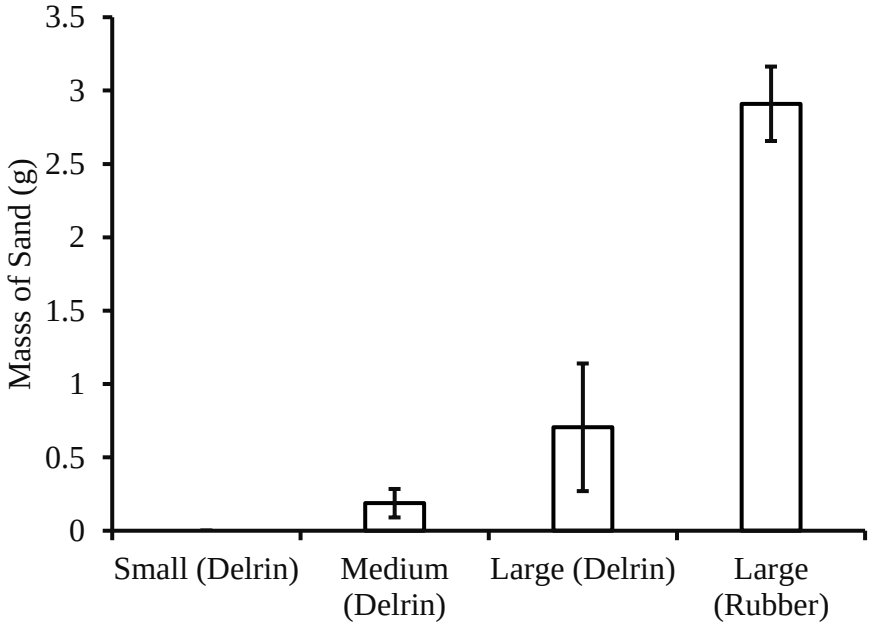


Figure 5.16. The mass of sand from damaged cavities for the different stones placed in 0.3% agarose. Small, medium and large stones prepared in the Delrin mould were subjected to 20 Hz and the large stones prepared in the rubber mould were subjected to three PRF's (20 Hz, 40 Hz and 80 Hz)

Figure 5.17 shows that the Treatment Average Total Spatial Power for stones prepared in a mould made of rubber and placed in 0.3% agarose compared to 6% agarose for three PRF's. In 0.3% agarose when the pulse repetition frequency is reduced from 80 Hz to 20 Hz, the Treatment Average Total Spatial Power increases by 99%. In 6% agarose, the pulse repetition frequency of 80 Hz has a spatial power 52% less than the power at a frequency of 20 Hz. In general, it was observed that the Treatment Average Total Spatial Power decreases with the higher PRF. Also, the agarose concentration likely has a little effect on the cavitation around the stone. Figure 5.18 shows the mass of sand with the Treatment Average Total Spatial Power and it is observed that higher power does not necessarily correspond to higher damage in 0.3% agarose. No damage was caused to the gel when the agarose concentration increased from 0.3% to 6%.

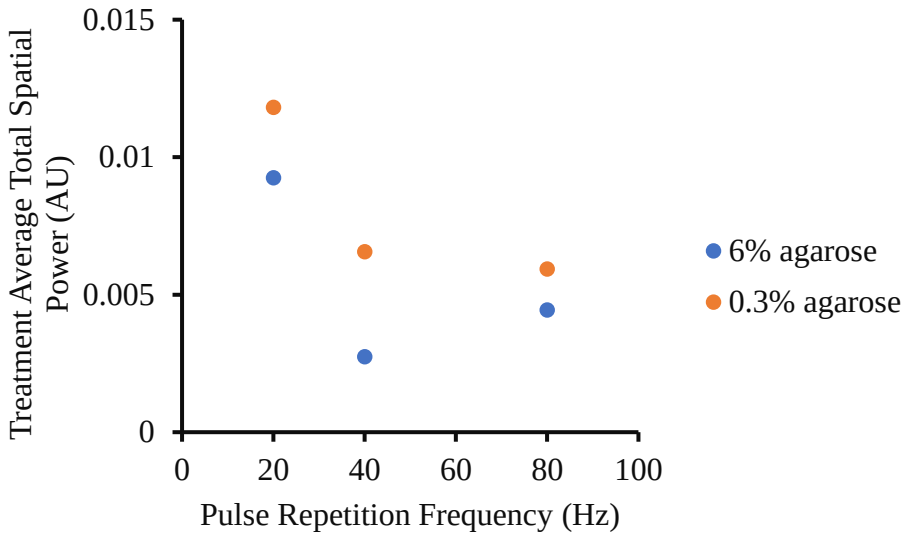


Figure 5.17. Pulse Repetition Frequency and Treatment Average Total Spatial Power from the L11-4 for large stones prepared in rubber mould and placed in 0.3% and 6% agarose (n=3 each).

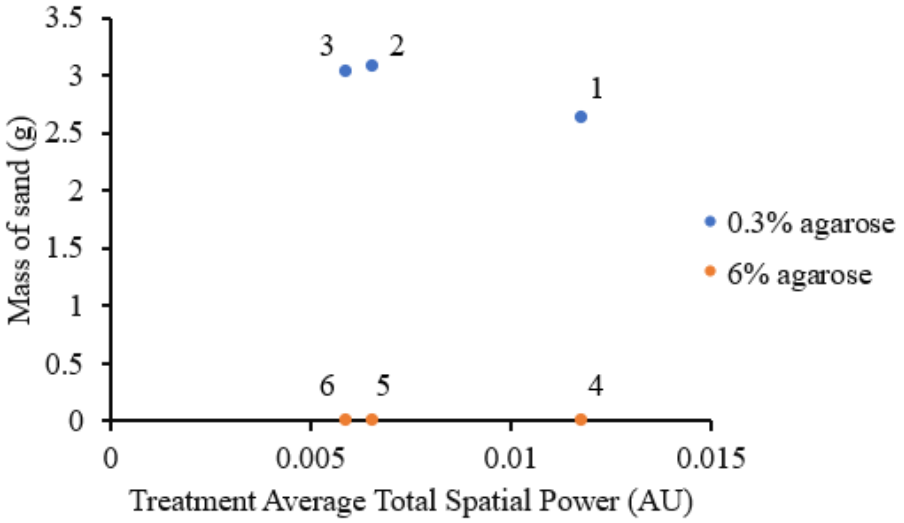


Figure 5.18. The mass of sand from damaged cavities and Treatment Average Total Spatial Power for large stones prepared in a rubber mould, and placed in 0.3% agarose and 6% agarose. Stones 1 and 4 were treated with a PRF of 20 Hz, Stones 2 and 5 were treated with a PRF of 40 Hz and Stones 3 and 6 were treated with a PRF of 80 Hz.

5.4. DISCUSSION AND CONCLUSION

In this chapter, cavitation was quantified by beamforming the acoustic emissions and applying weight vectors using the RCB approach. There was a correlation observed between the stone size and the mean Treatment Average Total Spatial Power which increased by 21% as the stone dimension was increased from ‘small’ to ‘large’. However, there was no correlation observed between the stone fragmentation and Treatment Average Total Spatial Power. The evolution of PAM was computed in form of the Spatial Integral Frame Power and it was not a robust indicator of fragmentation. The Treatment Average Total Spatial Power of stones placed in 0.3% and 6% agarose were in a similar range during the BWL treatment which showed that the agarose concentration did not have an effect on the stone fragmentation. The Treatment Average Total Spatial Power of the stones prepared in rubber moulds was four orders of magnitude higher than the stones prepared in the Delrin mould. This was likely due to the

greater roughness of the stones made in rubber moulds, resulting in more cavitation nuclei , although surface roughness was not quantitatively assessed.

Damage to agarose samples was observed as cavities for 0.3% agarose in the presence of stones. When the agarose concentration was increased to 6%, there was no damage observed to agarose samples. This is potentially due to the increase in strength of agarose at higher concentrations. BWL experiments performed on 0.3% agarose samples with stones prepared in Delrin moulds showed that the agarose damage increased with the stone surface area. Higher agarose damage was observed in the samples which consisted of stone prepared from rubber moulds with a rougher surface than those samples which consisted of stones made from Delrin moulds with a smoother surface. Although the agarose damage was observed to increase with the stone surface area and roughness, there was no relation observed between the Treatment Average Total Spatial Power and mass of sand measuring the agarose damage.

Although B-mode imaging can be used to detect persistent bubble clouds during the BWL treatment, it cannot extract information about cavitation power. In contrast, PAM has the ability to generate spatial maps of real-time source strength from cavitation activity. This study used PAM to monitor stone fragmentation with time and compute the values of cavitation in the form of spatial power during BWL treatment. Based on the results, in this study, it was not possible to use PAM to reliably correlate cavitation with the type of stone fragmentation. However, the overall cavitation values quantified in the form of Treatment Average Total Spatial Power have shown that cavitation changes strongly with surface roughness. At higher surface roughness, higher values of Treatment Average Total Spatial Power were obtained, and agarose damage was also observed. Hence, cavitation can be monitored using PAM to predict agarose or tissue damage.

To the best of our knowledge, no other PAM study has been performed on BWL to localise cavitation in real-time. The results in agarose suggest that PAM may be viable as a means of testing tissue damage during BWL. This motivates using PAM for monitoring cavitation in a kidney during BWL. A possible starting point might be using a perfused kidney model as has been done in HIFU assessment [110], as cavitation is highly dependent on the properties of the medium and a perfused kidney gives a more realistic environment than agarose, for cavitation without the expense and complications of live animal experiments.

PAM has previously been used to study lesion [41], cavitation from a microbubble [40] and during the addition of microbubbles to an in-vitro flow [42]. May et. al. [38] used B-mode imaging to detect cavitation within the kidney parenchyma or collecting space during BWL. However, parameters such as spatial power cannot be extracted using B-mode imaging and hence the quantification of cavitation is not possible. Our results from PAM during BWL experiments show that the stone surface area and its preparation most likely dominates the spatial power. Although PAM can be used to quantify the spatial power during BWL treatment, the data reported here was not able to obtain a way of extracting information on the stone fragmentation or agarose damage.

6. CONCLUSION

This chapter consists of a summary of key conclusions from different chapters outlined in the thesis. Suggestions are also added for future work.

Chapter 1 consists of the literature review and shows the state-of-the-art behind SWL and BWL. It shows that kidney injury occurs during the SWL and that cavitation is a crucial mechanism behind this damage. Studies have shown BWL to be successful in animal and human models and as an alternative to the SWL. BWL induce less tissue damage than SWL and can be used as an office-based treatment rather than in hospitals, as is the case with SWL. Cavitation also leads to tissue damage in BWL; motivating the need to monitor cavitation. Passive Acoustic Mapping was identified as a potential tool as it allows for temporal and spatial identification of cavitation using off-the-shelf transducer technology. Various studies were reviewed demonstrating how PAM has been used for ablation monitoring, drug delivery and detecting cavitation during the microbubble flow. Our literature review found that no PAM analysis was performed to monitor and quantify cavitation during the BWL.

Chapter 2 introduced the common viscoelastic models for soft tissue and the concept of fractional viscoelasticity. The equations behind the S-FKV model were derived, which shows a power law behaviour in the frequency domain. Different methods of mechanical testing were introduced : uniaxial compression, oscillatory shear testing and oscillatory nanoindentation. The theory by which viscoelastic properties could be recovered were described. This chapter reported on measurements made of the mechanical properties of porcine kidneys at macro and micro-length scales. A second-order Mooney-Rivlin model was used to fit the non-linear stress-strain data from uniaxial testing, and an elastic modulus of ~45 kPa was obtained until 2% strain. Oscillatory shear tests conducted at the macro-length scale observed a linear viscoelastic behaviour until at least 0.3% strain. Frequency sweep results showed a power law behaviour at different axial strains, and an S-FKV model fitted the frequency response with a correlation

better than 0.99. These results also showed that both the storage modulus and loss modulus increased monotonically with the axial strain, possibly due to the interstitial fluid being forced out of the tissue during the compression leading to a more solid-like behaviour. Stress relaxation tests were performed at a shear strain of 0.1%, and the results were compared to the predicted stress values by the S-FKV model. It was found that the S-FKV model predictions were within 26% of the measurements over a 10s relaxation time. The S-FKV model was also extrapolated from frequencies <10 Hz to values as high as 500 Hz to compare with values in the literature, with the extrapolation showing a discrepancy up to a factor of 4. Oscillatory nanoindentation tests were performed up to a frequency of 110 Hz. A storage modulus value of up to 45 kPa and a loss modulus of up to 14 kPa were obtained. The storage modulus and loss modulus were independent of the frequency, potentially due to the nanoindenter capturing local elastic effects and not the large-scale deformation from intercellular slide-slip interactions.

Chapter 3 investigated the mechanical properties of the porcine aorta, heart, liver and brain. These tests were performed at the macro-length scale using a stress-controlled rheometer. The strain sweep results showed a linear viscoelastic region until 0.3% strain in all the tissues. A frequency sweep test was performed on the porcine heart, liver and brain for a range of axial strains. A power-law behaviour with frequency was observed. The S-FKV model fitted the storage modulus and loss modulus data at all axial strains with a correlation higher than 0.99. Both the storage modulus and loss modulus increased monotonically with the axial strain. The viscosity parameter in the S-FKV model also increased with the axial strain in all the porcine organs suggesting a higher interstitial fluid flow as the samples were compressed. A frequency sweep test was performed on the porcine aorta at a contact force of 0.1 N, and a springpot model fitted the storage modulus and loss modulus. The S-FKV model was not used to fit the frequency response in the aorta since the loss modulus changed marginally with the frequency. The S-FKV model fitted in porcine organs was used to predict their stress responses, and a

comparison was made with the modulus values obtained from relaxation tests. The S-FKV model predictions and the amplitudes of stress relaxation obtained experimentally were within 26%. The shear storage modulus from the S-FKV and springpot model was extrapolated from less than 10 Hz to frequencies in the range of kHz in order to compare with values in the literature, and a discrepancy up to a factor of 5 in animal tissues and up to a factor of 27 in human tissues was observed.

Chapter 4 investigated the mechanical properties of different agarose concentrations using uniaxial compression, oscillatory shear and oscillatory nanoindentation testing. The uniaxial tests showed that the elastic modulus of 1.2% agarose is similar to that of the porcine kidneys and that the elastic modulus follows a power-law behaviour with agarose concentration. Oscillatory shear tests were conducted on a range of agarose concentrations in the form of strain sweep, frequency sweep and stress relaxation tests. It was found that the shear storage modulus of 0.4% agarose resembled the porcine heart, and 0.3% agarose resembled the porcine kidney. The storage modulus of liver tissue was 50% lower than the lowest possible agarose concentration that would gel. The strain sweep results showed that the linear viscoelastic region in both the storage modulus and loss modulus as a function of strain reduced with the increase in agarose concentration or stiffness. The frequency sweep results showed a weak dependency of the storage modulus of agarose with frequency compared to the power-law behaviour observed in porcine organs. This also corresponded to agarose relaxing more slowly than the porcine organs. This is likely due to the fundamental structural differences as agarose consists of a helices-water matrix structure compared to porcine organs, which consist of a connective tissue matrix with interstitium. A springpot was used to fit the frequency response of different agarose concentrations at various axial strains with a correlation better than 0.99. The springpot was used to predict the stress response of agarose samples to a step shear strain, and the predictions were within 10% of the stress response measured using the relaxation tests.

Oscillatory nanoindentation results showed that the shear storage modulus of 1.2% agarose varied from 34 kPa to 48 kPa and was in a similar range as that of the porcine kidney. However, a lower standard deviation was observed in the agarose samples compared to the porcine kidney samples since agarose samples are relatively homogenous.

Chapter 5 introduced PAM and defined the equations for computing the source energy using two signal processing approaches: RCB and TEA. PAM was used to quantify the cavitation when 350 kHz burst waves fragmented artificial Ultracal-30 stones. An in-line P4-2 probe and an out-of-line L11-4 probe collected the acoustic emissions. The Spatial Integral Frame Power and Treatment Average Total Spatial Power were computed using the RCB approach. PAM results showed that changing the agarose concentration did not alter the cavitation around the stone, and the Treatment Average Total Spatial Power was in a similar range when stones were placed inside 0.3% and 6% agarose. We found that the cavitation evolution with time using PAM does not help detect the type of cavitation around the stone. A Delrin mould was used to prepare stones of three different sizes: 'Small', 'Medium' and 'Large'. It was observed that Treatment Average Total Spatial Power increased by 21% as the stone size varied from small to large. The surface roughness of the stone was increased by preparing the stones in a rubber mould. It was observed that the Treatment Average Total Spatial Power increased by four orders of magnitude as the stone mould was changed from Delrin to rubber. This is consistent with the hypothesis that cavitation strongly depends on surface roughness. Agarose damage was also analysed using the stones made in the Delrin mould, and it was found that the volume of the damage increased by 709% as the stone size increased from small to large. When stones made in the rubber mould were used, the damage to the agarose increased by a factor of four. The Treatment Average Total Spatial Power and the mass of sand quantifying the agarose damage were the highest in the stones prepared in a rubber mould. This chapter concluded that PAM could be used to compute parameters such as spatial power during the BWL treatment of

kidney stones. However, the stone surface roughness and dimensions dominated the PAM results. The stone surface roughness and dimensions will vary from patient to patient, and our study was unable to use PAM for extracting useful information during the BWL. PAM showed promises in monitoring the tissue or agarose damage but not the stone fragmentation, perhaps because the cavitation in fluid dominated over that of the stone.

6.1. FUTURE WORK

The mechanical properties measured here were restricted to 10s of Hz, future work could employ techniques such as elastography to measure the viscoelastic properties at frequencies of kHz or MHz. This would be useful in understanding the mechanical response of kidneys during BWL when burst waves with a fundamental frequency of hundreds of kHz propagate through them. Magnetic Resonance Elastography could be used to measure the properties of different agarose concentrations at higher frequencies and identify the concentration which resembles the viscoelastic properties of porcine kidneys and other organs such as the heart, liver and brain.

In this thesis, oscillatory nanoindentation tests were performed on porcine kidneys and a range of agarose concentrations using a flat cylindrical punch of 100 μm diameter. It was found that the storage modulus and loss modulus were higher by a factor of 50 to 90 at the micro-length scale compared to the rheological properties obtained via oscillatory shear experiments using a rheometer plate of 25 mm diameter. Future studies should investigate the change in mechanical properties of agarose, and porcine tissues as the indenter dimensions are varied as 0.1 mm, 0.5 mm, 1 mm, 5 mm and 10 mm. This will enable us to identify the length scale at which local deformation and global deformation contribute to measuring viscoelastic properties.

PAM was used to monitor and quantify the cavitation around the stone during BWL, and it was found that the stone dimension and surface roughness likely dominated the PAM results. In-

vitro models of agarose were used to fragment the stones and analyse the cavitation damage. Going forward, it would be useful to investigate more sophisticated signal processing algorithms to assess whether PAM has some benefits in real-time monitoring and if it has the potential to be used in clinical settings alongside BWL. Hence, it would be interesting to perform BWL experiments by implanting Ultracal-30 stones inside the perfused kidneys and using PAM to quantify the cavitation and tissue damage. Perfused kidneys allow for: i)The use of the L11-4 probe to collect acoustic emissions as it will be closer to the kidneys rather than measuring signals from the P4-2 probe, which would be deployed in-vivo. ii)Reducing the dependency on live animal experiments due to ethical and monetary concerns. Lastly, in the experiments performed during this thesis, acoustic emissions were extracted from the L11-4 probe due to its superior resolution over the P4-2 probe. One possible area of future research would be to combine the acoustic emissions measured from the two probes simultaneously in order to localising the cavitation energy from a small volumetric region as has been done in other therapeutic ultrasound applications [111].

REFERENCES

[1] Atherton, J.C., 1972. Renal physiology. British journal of anaesthesia, 44(3), pp.236-245.

[2] Pitts, R.F. and Jacoby, J., 1963. Physiology of the kidney and body fluids. The Journal of the American Society of Anesthesiologists, 24(5), pp.748-748.

[3] Biga, L. (2019) 25.1 Internal and External Anatomy of the Kidney – Anatomy & Physiology. Available at: https://open.oregonstate.education/aandp/chapter/25-1-internal-and-external-anatomy-of-the-kidney/.

[4] Khan, S.R., Pearle, M.S., Robertson, W.G., Gambaro, G., Canales, B.K., Doizi, S., Traxer, O. and Tiselius, H.G., 2016. Kidney stones. Nature Reviews Disease Primers, 2(1), pp.1-23.

[5] Finlayson, B., 1978. Physicochemical aspects of urolithiasis. Kidney international, 13(5), pp.344-360.

[6] Evan, A.P., 2010. Physiopathology and etiology of stone formation in the kidney and the urinary tract. Pediatric nephrology, 25, pp.831-841.

[7] Wason SE, Monfared S, Ionson A, et al. Ureteroscopy. [Updated 2022 Nov 28]. In: StatPearls [Internet]. Treasure Island (FL): StatPearls Publishing; 2022 Jan-. Available from: https://www.ncbi.nlm.nih.gov/books/NBK560556/

[8] Netsch, C., Knipper, S., Bach, T., Herrmann, T.R. and Gross, A.J., 2012. Impact of preoperative ureteral stenting on stone-free rates of ureteroscopy for nephroureterolithiasis: a matched-paired analysis of 286 patients. Urology, 80(6), pp.1214-1220.

[9] Özdedeli, K. and Mete, Ç.E.K., 2012. Residual fragments after percutaneous nephrolithotomy. Balkan medical journal, 2012(3), pp.230-235.

[10] Holmes, S.A.V. and Whitfield, H.N., 1991. The current status of lithotripsy. British journal of urology, 68(4), pp.337-344.

[11] Chaussy, C.H., Brendel, W. and Schmiedt, E., 1980. Extracorporeally induced destruction of kidney stones by shock waves. The Lancet, 316(8207), pp.1265-1268.

[12] Cleveland, R.O., McAteer, J.A., 2012. The physics of shock wave lithotripsy. In: Smith's Textbook on Endourology, vol. 1. 3rd edition Wiley-Blackwell., pp. 527–558.

[13] Abdel-Khalek, M., Sheir, K.Z., Mokhtar, A.A., Eraky, I., Kenawy, M. and Bazeed, M., 2004. Prediction of success rate after extracorporeal shock-wave lithotripsy of renal stones A multivariate analysis model. Scandinavian journal of urology and nephrology, 38(2), pp.161-167.

[14] Reynolds, L.F., Kroczak, T. and Pace, K.T., 2018. Indications and contraindications for shock wave lithotripsy and how to improve outcomes. Asian journal of urology, 5(4), pp.256-263.

[15] Mishra, A. and Cleveland R. (2022). Pulsed waves for medical therapy. Power Ultrasonics: 2nd Edition. Book chapter awaiting publication.

[16] Rubin, J.I., Arger, P.H., Pollack, H.M., Banner, M.P., Coleman, B.G., Mintz, M.C. and VanArsdalen, K.N., 1987. Kidney changes after extracorporeal shock wave lithotripsy: CT evaluation. Radiology, 162(1), pp.21-24.

[17] Ng, C.F., Luke, S., Yee, C.H., Chu, W.C., Wong, K.T. and Yuen, J.W., 2017. A prospective randomized study comparing the effect of different kidney protection treatment protocols on acute renal injury after extracorporeal shockwave lithotripsy. Journal of Endourology, 31(1), pp.57-65.

[18] Krishnamurthi, V. and Streem, S.B., 1995. Long-term radiographic and functional outcome of extracorporeal shock wave lithotripsy induced perirenal hematomas. The Journal of urology, 154(5), pp.1673-1675.

[19] Snedeker, J.G., Niederer, P., Schmidlin, F.R., Farshad, M., Demetropoulos, C.K., Lee, J.B. and Yang, K.H., 2005. Strain-rate dependent material properties of the porcine and human kidney capsule. Journal of biomechanics, 38(5), pp.1011-1021.

[20] Nasseri, S., Bilston, L.E. and Phan-Thien, N., 2002. Viscoelastic properties of pig kidney in shear, experimental results and modelling. Rheologica acta, 41(1-2), pp.180-192.

[21] Shao, Y., Connors, B.A., Evan, A.P., Willis, L.R., Lifshitz, D.A. and Lingeman, J.E., 2003. Morphological changes induced in the pig kidney by extracorporeal shock wave lithotripsy: nephron injury. The Anatomical Record Part A: Discoveries in Molecular, Cellular, and Evolutionary Biology, 275(1), pp.979-989.

[22] Connors, B.A., Evan, A.P., Willis, L.R., Blomgren, P.M., Lingeman, J.E. and Fineberg, N.S., 2000. The effect of discharge voltage on renal injury and impairment caused by lithotripsy in the pig. Journal of the American Society of Nephrology, 11(2), pp.310-318.

[23] McAteer, J.A. and Evan, A.P., 2008, March. The acute and long-term adverse effects of shock wave lithotripsy. In Seminars in nephrology (Vol. 28, No. 2, pp. 200-213). WB Saunders.

[24] Coleman, A.J., Saunders, J.E., Crum, L.A. and Dyson, M., 1987. Acoustic cavitation generated by an extracorporeal shockwave lithotripter. Ultrasound in medicine & biology, 13(2), pp.69-76.

[25] Cleveland, R.O., Lifshitz, D.A., Connors, B.A., Evan, A.P., Willis, L.R. and Crum, L.A., 1998. In vivo pressure measurements of lithotripsy shock waves in pigs. Ultrasound in medicine & biology, 24(2), pp.293-306.

[26] Coleman, A.J., Choi, M.J. and Saunders, J.E., 1996. Detection of acoustic emission from cavitation in tissue during clinical extracorporeal lithotripsy. Ultrasound in medicine & biology, 22(8), pp.1079-1087.

[27] Williams Jr, J.C., Woodward, J.F., Stonehill, M.A., Evan, A.P. and McAteer, J.A., 1999. Cell damage by lithotripter shock waves at high pressure to preclude cavitation. Ultrasound in medicine & biology, 25(9), pp.1445-1449.

[28] Evan, A.P., Willis, L.R., McAteer, J.A., Bailey, M.R., Connors, B.A., Shao, Y., Lingeman, J.E., Williams, J.C., Fineberg, N.S. and Crum, L.A., 2002. Kidney damage and renal functional

changes are minimized by waveform control that suppresses cavitation in shock wave lithotripsy. The Journal of urology, 168(4 Part 1), pp.1556-1562.

[29] Lifshitz, D.A., Williams Jr, J.C., Sturtevant, B., Connors, B.A., Evan, A.P. and McAteer, J.A., 1997. Quantitation of shock wave cavitation damage in vitro. Ultrasound in medicine & biology, 23(3), pp.461-471.

[30] Howard, D. and Sturtevant, B., 1997. In vitro study of the mechanical effects of shock-wave lithotripsy. Ultrasound in medicine & biology, 23(7), pp.1107- 1122.

[31] Freund, J.B., Colonius, T. and Evan, A.P., 2007. A cumulative shear mechanism for tissue damage initiation in shock-wave lithotripsy. Ultrasound in medicine & biology, 33(9), pp.1495-1503.

[32] Maxwell, A.D., Wang, Y.N., Kreider, W., Cunitz, B.W., Starr, F., Lee, D., Nazari, Y., Williams Jr, J.C., Bailey, M.R. and Sorensen, M.D., 2019. Evaluation of renal stone comminution and injury by burst wave lithotripsy in a pig model. Journal of endourology, 33(10), pp.787-792.

[33] Maxwell, A.D., Cunitz, B.W., Kreider, W., Sapozhnikov, O.A., Hsi, R.S., Harper, J.D., Bailey, M.R. and Sorensen, M.D., 2015. Fragmentation of urinary calculi in vitro by burst wave lithotripsy. The Journal of urology, 193(1), pp.338- 344.

[34] Bailey, M.R., Maxwell, A.D., Cao, S., Ramesh, S., Liu, Z., Williams, J.C., Thiel, J., Dunmire, B., Colonius, T., Kuznetsova, E. and Kreider, W., 2022. Improving burst wave lithotripsy effectiveness for small stones and fragments by increasing frequency: theoretical modeling and ex vivo study. Journal of Endourology, 36(7), pp.996-1003.

[35] Zwaschka, T.A., Ahn, J.S., Cunitz, B.W., Bailey, M.R., Dunmire, B., Sorensen, M.D., Harper, J.D. and Maxwell, A.D., 2018. Combined burst wave lithotripsy and ultrasonic propulsion for improved urinary stone fragmentation. Journal of endourology, 32(4), pp.344-349.

[36] Harper, J.D., Lingeman, J.E., Sweet, R.M., Metzler, I.S., Sunaryo, P.L., Williams Jr, J.C., Maxwell, A.D., Thiel, J., Cunitz, B.W., Dunmire, B. and Bailey, M.R., 2022. Fragmentation of Stones by Burst Wave Lithotripsy in the First 19 Humans. The Journal of urology, 207(5), pp.1067-1076.

[37] Wang, Y.N., Kreider, W., Hunter, C., Cunitz, B.W., Thiel, J., Starr, F., Dai, J.C., Nazari, Y., Lee, D., Williams, J.C. and Bailey, M.R., 2018, November. An in vivo demonstration of efficacy and acute safety of burst wave lithotripsy using a porcine model. In Proceedings of Meetings on Acoustics 176ASA (Vol. 35, No.1, p. 020009). Acoustical Society of America.

[38] May, P.C., Kreider, W., Maxwell, A.D., Wang, Y.N., Cunitz, B.W., Blomgren, P.M., Johnson, C.D., Park, J.S., Bailey, M.R., Lee, D. and Harper, J.D., 2017. Detection and evaluation of renal injury in burst wave lithotripsy using ultrasound and magnetic resonance imaging. Journal of endourology, 31(8), pp.786-792.

[39] Paverd, C.M., 2019. Passive Acoustic Mapping for vascular permeability assessment (Doctoral dissertation, University of Oxford).

[40] Gyongy, M. and Coussios, C.C., 2009. Passive spatial mapping of inertial cavitation during HIFU exposure. IEEE Transactions on Biomedical Engineering, 57(1), pp.48-56.

[41] Jensen, C.R., Ritchie, R.W., Gyöngy, M., Collin, J.R., Leslie, T. and Coussios, C.C., 2012. Spatiotemporal monitoring of high-intensity focused ultrasound therapy with passive acoustic mapping. Radiology, 262(1), pp.252-261.

[42] Crake, C., de Saint Victor, M., Coviello, C., Owen, J., Coussios, C.C. and Stride, E., 2013, June. Passive acoustic mapping of magnetic microbubbles in an in vitro flow model. In Proceedings of Meetings on Acoustics ICA2013 (Vol. 19, No. 1, p. 075025). Acoustical Society of America.

[43] Coviello, C., Kozick, R., Choi, J., Gyöngy, M., Jensen, C., Smith, P.P. and Coussios, C.C., 2015. Passive acoustic mapping utilizing optimal beamforming in ultrasound therapy monitoring. The Journal of the Acoustical Society of America, 137(5), pp.2573-2585.

[44] Pace, K.T., Ghiculete, D., Harju, M., Honey, R.J.D.A. and University of Toronto Lithotripsy Associates, 2005. Shock wave lithotripsy at 60 or 120 shocks per minute: a randomized, double-blind trial. The Journal of urology, 174(2), pp.595-599.

[45] Craiem, D. and Magin, R.L., 2010. Fractional order models of viscoelasticity as an alternative in the analysis of red blood cell (RBC) membrane mechanics. Physical biology, 7(1), p.013001.

[46] Akhtar, R., Draper, E.R., Adams, D.J. and Hay, J., 2018. Oscillatory nanoindentation of highly compliant hydrogels: a critical comparative analysis with rheometry. Journal of Materials Research, 33(8), pp.873-883.

[47] Pharr, G.M., Oliver, W.C. and Brotzen, F.R., 1992. On the generality of the relationship among contact stiffness, contact area, and elastic modulus during indentation. Journal of materials research, 7(3), pp.613-617.

[48] Peters, A.E., Comerford, E.J., Macaulay, S., Bates, K.T. and Akhtar, R., 2017. Micromechanical properties of canine femoral articular cartilage following multiple freeze-thaw cycles. Journal of the mechanical behavior of biomedical materials, 71, pp.114-121.

[49] Öpik, R., Hunt, A., Ristolainen, A., Aubin, P.M. and Kruusmaa, M., 2012, June. Development of high fidelity liver and kidney phantom organs for use with robotic surgical systems. In 2012 4th IEEE RAS & EMBS international conference on biomedical robotics and biomechatronics (BioRob) (pp. 425-430). IEEE.

[50] Sommerer, C., Scharf, M., Seitz, C., Millonig, G., Seitz, H.K., Zeier, M. and Mueller, S., 2013. Assessment of renal allograft fibrosis by transient elastography. Transplant International, 26(5), pp.545-551.

[51] Umale, S., Deck, C., Bourdet, N., Dhumane, P., Soler, L., Marescaux, J. and Willinger, R., 2013. Experimental mechanical characterization of abdominal organs: liver, kidney & spleen. Journal of the mechanical behavior of biomedical materials, 17, pp.22-33.

[52] Farshad, M., Barbezat, M., Flüeler, P., Schmidlin, F., Graber, P. and Niederer, P., 1999. Material characterization of the pig kidney in relation with the biomechanical analysis of renal trauma. Journal of biomechanics, 32(4), pp.417- 425.

[53] Nicolle, S., Vezin, P. and Palierne, J.F., 2010. A strain-hardening bi-power law for the nonlinear behaviour of biological soft tissues. Journal of biomechanics, 43(5), pp.927-932.

[54] Kruse, S.A., Smith, J.A., Lawrence, A.J., Dresner, M.A., Manduca, A.J.F.G., Greenleaf, J.F. and Ehman, R.L., 2000. Tissue characterization using magnetic resonance elastography: preliminary results. Physics in Medicine & Biology, 45(6), p.1579.

[55] Amador, C., Urban, M.W., Warner, L.V. and Greenleaf, J.F., 2009, September. In vitro renal cortex elasticity and viscosity measurements with shearwave dispersion ultrasound vibrometry (SDUV) on swine kidney. In 2009 Annual International Conference of the IEEE Engineering in Medicine and Biology Society (pp. 4428-4431). IEEE.

[56] Chen, H., Zhao, X., Lu, X. and Kassab, G., 2013. Non-linear micromechanics of soft tissues. International journal of non-linear mechanics, 56, pp.79-85.

[57] Mattice, J.M., Lau, A.G., Oyen, M.L. and Kent, R.W., 2006. Spherical indentation load-relaxation of soft biological tissues. Journal of Materials Research, 21(8), pp.2003-2010.

[58] Yin, M., Woollard, J., Wang, X., Torres, V.E., Harris, P.C., Ward, C.J., Glaser, K.J., Manduca, A. and Ehman, R.L., 2007. Quantitative assessment of hepatic fibrosis in an animal model with magnetic resonance elastography. Magnetic Resonance in Medicine: An Official Journal of the International Society for Magnetic Resonance in Medicine, 58(2), pp.346-353.

[59] Kruse, S.A., Rose, G.H., Glaser, K.J., Manduca, A., Felmlee, J.P., Jack Jr, C.R. and Ehman, R.L., 2008. Magnetic resonance elastography of the brain. Neuroimage, 39(1), pp.231-237.

[60] Kolipaka, A., McGee, K.P., Araoz, P.A., Glaser, K.J., Manduca, A. and Ehman, R.L., 2009. Evaluation of a rapid, multiphase MRE sequence in a heart-simulating phantom. Magnetic Resonance in Medicine: An Official Journal of the International Society for Magnetic Resonance in Medicine, 62(3), pp.691-698.

[61] Dong, H., Mazumder, R., Illapani, V.S.P., Mo, X., White, R.D. and Kolipaka, A., 2017. In vivo quantification of aortic stiffness using MR elastography in hypertensive porcine model. Magnetic resonance in medicine, 78(6), pp.2315-2321.

[62] Chintada, B.R., Rau, R. and Goksel, O., 2021. Nonlinear characterization of tissue viscoelasticity with acoustoelastic attenuation of shear waves. IEEE Transactions on Ultrasonics, Ferroelectrics, and Frequency Control, 69(1), pp.38-53.

[63] Sack, I., Beierbach, B., Wuerfel, J., Klatt, D., Hamhaber, U., Papazoglou, S., Martus, P. and Braun, J., 2009. The impact of aging and gender on brain viscoelasticity. Neuroimage, 46(3), pp.652-657.

[64] Kobayashi, Y., Okamoto, J. and Fujie, M.G., 2005, April. Physical properties of the liver and the development of an intelligent manipulator for needle insertion. In Proceedings of the 2005 IEEE International Conference on Robotics and Automation (pp. 1632-1639). IEEE.

[65] Kobayashi, Y., Onishi, A., Hoshi, T., Kawamura, K., Hashizume, M. and Fujie, M.G., 2009. Development and validation of a viscoelastic and nonlinear liver model for needle insertion. International journal of computer assisted radiology and surgery, 4(1), pp.53-63.

[66] Kobayashi, Y., Kato, A., Watanabe, H., Hoshi, T., Kawamura, K. and Fujie, M.G., 2012. Modeling of viscoelastic and nonlinear material properties of liver tissue using fractional calculations. Journal of Biomechanical Science and Engineering, 7(2), pp.177-187.

[67] Kobayashi, Y., Watanabe, H., Hoshi, T., Kawamura, K. and Fujie, M.G., 2012. Viscoelastic and nonlinear liver modeling for needle insertion simulation. Soft Tissue Biomechanical Modeling for Computer Assisted Surgery, pp.41-67.

[68] Craiem, D., Rojo, F.J., Atienza, J.M., Armentano, R.L. and Guinea, G.V., 2008. Fractional-order viscoelasticity applied to describe uniaxial stress relaxation of human arteries. Physics in Medicine & Biology, 53(17), p.4543.

[69] Craiem, D. and Armentano, R.L., 2007. A fractional derivative model to describe arterial viscoelasticity. Biorheology, 44(4), pp.251-263.

[70] Bernier, R.A. and Hillary, F.G., 2019. Traumatic brain injury and frontal lobe plasticity. Handbook of clinical neurology, 163, pp.411-431.

[71] Smith, M., 2021. Mechanisms and genetics of neurodevelopmental cognitive disorders. Academic Press., pp. 49-76. https://doi.org/10.1016/B978-0-12-821913-3.00004-4

[72] Daroff, R.B. and Aminoff, M.J., 2014. Encyclopedia of the neurological sciences. Academic press, pp. 811-819. https://doi.org/10.1016/B978-0-12-385157-4.01171-4

[73] Dong, H., Russell, D.S., Litsky, A.S., Joseph, M.E., Mo, X., White, R.D. and Kolipaka, A., 2020. In vivo aortic magnetic resonance elastography in abdominal aortic aneurysm: a validation in an animal model. Investigative radiology, 55(7), p.463.

[74] Schmitt, C., Henni, A.H. and Cloutier, G., 2010. Ultrasound dynamic micro-elastography applied to the viscoelastic characterization of soft tissues and arterial walls. Ultrasound in medicine & biology, 36(9), pp.1492-1503.

[75] Kolipaka, A., Araoz, P.A., McGee, K.P., Manduca, A. and Ehman, R.L., 2010. Magnetic resonance elastography as a method for the assessment of effective myocardial stiffness throughout the cardiac cycle. Magnetic resonance in medicine, 64(3), pp.862-870.

[76] Nenadic, I., Urban, M.W. and Greenleaf, J.F., 2009, September. Ex vivo measurements of myocardial viscoelasticity using Shearwave Dispersion Ultrasound Vibrometry (SDUV). In 2009 Annual International Conference of the IEEE Engineering in Medicine and Biology Society (pp. 2895-2898). IEEE.

[77] Wex, C., Stoll, A., Fröhlich, M., Arndt, S. and Lippert, H., 2013. How preservation time changes the linear viscoelastic properties of porcine liver. Biorheology, 50(3-4), pp.115-131.

[78] Shen, F., Tay, T.E., Li, J.Z., Nigen, S., Lee, P.V.S. and Chan, H.K., 2006. Modified Bilston nonlinear viscoelastic model for finite element head injury studies.

[79] Thibault, K.L. and Margulies, S.S., 1998. Age-dependent material properties of the porcine cerebrum: effect on pediatric inertial head injury criteria. Journal of biomechanics, 31(12), pp.1119-1126.

[80] Wismans, J.S. and Paas, M.H., 1999. Comparison of the Dynamic Behaviour of Brain Tissue and Two Model Materials.

[81] Hrapko, M., Van Dommelen, J.A.W., Peters, G.W.M. and Wismans, J.S.H.M., 2008. The influence of test conditions on characterization of the mechanical properties of brain tissue. Journal of Biomechanical Engineering, 130(3).

[82] Hrapko, M., Van Dommelen, J.A.W., Peters, G.W.M. and Wismans, J.S.H.M., 2006. The mechanical behaviour of brain tissue: large strain response and constitutive modelling. Biorheology, 43(5), pp.623-636.

[83] Arbogast, K.B. and Margulies, S.S., 1997. Regional differences in mechanical properties of the porcine central nervous system. SAE transactions, pp.3807-3814.

[84] DeWall, R.J., Bharat, S., Varghese, T., Hanson, M.E., Agni, R.M. and Kliewer, M.A., 2012. Characterizing the compression-dependent viscoelastic properties of human hepatic pathologies using dynamic compression testing. Physics in Medicine & Biology, 57(8), p.2273.

[85] Fallenstein, G.T., Hulce, V.D. and Melvin, J.W., 1969. Dynamic mechanical properties of human brain tissue. Journal of biomechanics, 2(3), pp.217-226.

[86] Shuck, L.Z. and Advani, S.H., 1972. Rheological response of human brain tissue in shear.

[87] Chen, Q., Suki, B. and An, K.N., 2004. Dynamic mechanical properties of agarose gels modeled by a fractional derivative model. J. Biomech. Eng., 126(5), pp.666-671.

[88] Normand, V., Lootens, D.L., Amici, E., Plucknett, K.P. and Aymard, P., 2000. New insight into agarose gel mechanical properties. Biomacromolecules, 1(4), pp.730-738.

[89] Saris, D.B., Mukherjee, N., Berglund, L.J., Schultz, F.M., An, K.N. and O'Driscoll, S.W., 2000. Dynamic pressure transmission through agarose gels. Tissue engineering, 6(5), pp.531-537.

[90] McIlvain, G., Ganji, E., Cooper, C., Killian, M.L., Ogunnaike, B.A. and Johnson, C.L., 2019. Reliable preparation of agarose phantoms for use in quantitative magnetic resonance elastography. Journal of the mechanical behavior of biomedical materials, 97, pp.65-73.

[91] Manickam, K., Machireddy, R.R. and Seshadri, S., 2014. Characterization of biomechanical properties of agar based tissue mimicking phantoms for ultrasound stiffness imaging techniques. Journal of the mechanical behavior of Biomedical Materials, 35, pp.132-143.

[92] Kavitha, M. and Reddy, M.R., 2012, July. Characterization of tissue mimicking phantoms for acoustic radiation force impulse imaging. In 2012 IEEE International Conference on Imaging Systems and Techniques Proceedings (pp.553-557). IEEE.

[93] Brewin, M.P., Birch, M.J., Mehta, D.J., Reeves, J.W., Shaw, S., Kruse, C., Whiteman, J.R., Hu, S., Kenz, Z.R., Banks, H.T. and Greenwald, S.E., 2015. Characterisation of elastic and acoustic properties of an agar-based tissue mimicking material. Annals of biomedical engineering, 43(10), pp.2587-2596.

[94] Sugiyama, J., Rochas, C., Turquois, T., Taravel, F. and Chanzy, H., 1994. Direct imaging of polysaccharide aggregates in frozen aqueous dilute systems. Carbohydrate polymers, 23(4), pp.261-264.

[95] Le Goff, K.J., Gaillard, C., Helbert, W., Garnier, C. and Aubry, T., 2015. Rheological study of reinforcement of agarose hydrogels by cellulose nanowhiskers. Carbohydrate polymers, 116, pp.117-123.

[96] Chen, Q., Ringleb, S.I., Hulshizer, T. and An, K.N., 2005. Identification of the testing parameters in high frequency dynamic shear measurement on agarose gels. Journal of biomechanics, 38(4), pp.959-963.

[97] Delaine-Smith, R.M., Burney, S., Balkwill, F.R. and Knight, M.M., 2016. Experimental validation of a flat punch indentation methodology calibrated against unconfined compression tests for determination of soft tissue biomechanics. Journal of the mechanical behavior of biomedical materials, 60, pp.401-415.

[98] Nayar, V.T., Weiland, J.D. and Hodge, A.M., 2012. Macrocompression and nanoindentation of soft viscoelastic biological materials. Tissue Engineering Part C: Methods, 18(12), pp.968-975.

[99] Delius, M., Jordan, M., Eizenhoefer, H., Marlinghaus, E., Heine, G., Liebich, H.G. and Brendel, W., 1988. Biological effects of shock waves: kidney haemorrhage by shock waves in dogs—administration rate dependence. Ultrasound in medicine & biology, 14(8), pp.689-694.

[100] Chen, H., Kreider, W., Brayman, A.A., Bailey, M.R. and Matula, T.J., 2011. Blood vessel deformations on microsecond time scales by ultrasonic cavitation. Physical review letters, 106(3), p.034301.

[101] Zhong, P., Zhou, Y. and Zhu, S., 2001. Dynamics of bubble oscillation in constrained media and mechanisms of vessel rupture in SWL. Ultrasound in medicine & biology, 27(1), pp.119-134.

[102] Delius, M., Enders, G., Xuan, Z., Liebich, H.G. and Brendel, W., 1988. Biological effects of shock waves: kidney damage by shock waves in dogs—dose dependence. Ultrasound in medicine & biology, 14(2), pp.117-122.

[103] Choi, J.J., Carlisle, R.C., Coviello, C., Seymour, L. and Coussios, C.C., 2014. Non-invasive and real-time passive acoustic mapping of ultrasound-mediated drug delivery. Physics in Medicine & Biology, 59(17), p.4861.

[104] Kwan, J.J., Myers, R., Coviello, C.M., Graham, S.M., Shah, A.R., Stride, E., Carlisle, R.C. and Coussios, C.C., 2015. Ultrasound-propelled nanocups for drug delivery. small, 11(39), pp.5305-5314.

[105] Norton, S.J. and Won, I.J., 2000. Time exposure acoustics. IEEE Transactions on Geoscience and Remote Sensing, 38(3), pp.1337-1343.

[106] Li, J., Stoica, P. and Wang, Z., 2003. On robust Capon beamforming and diagonal loading. IEEE transactions on signal processing, 51(7), pp.1702-1715.

[107] Lyka, E., Coviello, C.M., Paverd, C., Gray, M.D. and Coussios, C.C., 2018. Passive acoustic mapping using data-adaptive beamforming based on higher order statistics. IEEE Transactions on Medical Imaging, 37(12), pp.2582-2592.

[108] Maxwell, A.D., Hunter, C., Cunitz, B.W., Kreider, W., Totten, S. and Wang, Y.N., 2021. Factors affecting tissue cavitation during burst wave lithotripsy. Ultrasound in medicine & biology, 47(8), pp.2286-2295.

[109] Maxwell, A.D., Kim, G.W., Furrow, E., Lulich, J.P., Torre, M., MacConaghy, B., Lynch, E., Leotta, D.F., Wang, Y.N., Borofsky, M.S. and Bailey, M.R., 2022. Development of a Burst Wave Lithotripsy System for Noninvasive Fragmentation of Ureteroliths in Pet Cats.

[110] Lorton, O., Guillemin, P.C., Holman, R., Desgranges, S., Gui, L., Crowe, L.A., Terraz, S., Nastasi, A., Lazeyras, F., Contino-Pépin, C. and Salomir, R., 2020. Enhancement of HIFU

thermal therapy in perfused tissue models using μ -sized FTAC-stabilized PFOB-core endovascular sonosensitizers. International Journal of Hyperthermia, 37(1), pp.1116-1130.

[111] Gray, M.D., Elbes, D., Paverd, C., Lyka, E., Coviello, C., Cleveland, R., & Coussios, C. (2021). Dual array passive acoustic mapping for cavitation imaging with enhanced 2-D resolution. IEEE Transactions on Ultrasonics, Ferroelectrics and Frequency Control 68(3), 647-663.